7-21-2022 1:30 PM

Investigating the Influence of Synthetic Environments on the Electronic Structure and Luminescence of Cr-doped Zinc Gallate

Xincheng Li, *The University of Western Ontario*

Supervisor: Liu, Lijia, *The University of Western Ontario*

A thesis submitted in partial fulfillment of the requirements for the Master of Science degree in Chemistry

Abstract

Cr doped $ZnGa_2O_4$ (Cr-ZGO) has shown potential in the field of bioimaging. To achieve the nano-size suiting for bioimaging, Cr-ZGO is normally synthesized using a hydrothermal method. There are few studies on how the hydrothermal conditions influence the structure and optical properties of the Cr-ZGO. The first two parts of this thesis study how different hydrothermal temperatures and pH environments will affect the optical properties of Cr-ZGO by photoluminescence spectroscopy. By combining the electronic structure information extracted from X-ray absorption near-edge structures (XANES) and extended X-ray absorption fine structure (EXAFS), a relationship among hydrothermal conditions, optical properties and electronic structure is built. The last part studies how the surface functionalization will affect the optical properties of Cr-ZGO synthesized under different hydrothermal conditions. It turns out oxygen vacancies around Zn will improve the emission intensity, Cr-ZGO synthesized at a low pH environment shows the strongest emission after functionalization.

Keywords:

Luminescence, Cr-doped zinc gallate, optical property, crystal structure, functionalization, X-ray absorption near-edge structures (XANES), extended X-ray absorption fine structure (EXAFS)

Summary for Lay Audience

Cr doped $ZnGa_2O_4$ (Cr-ZGO) is a new generation of persistent luminescent nanomaterials, which exhibit long-lasting luminescence for minutes or even hours after the excitation sources are removed. Cr-ZGO can emit light around 700 nm, which can be detected through tissue. Due to its desirable size and outstanding optical properties, persistent luminescent nanomaterials have shown potential in the field of visualizing biological activity. However, the optical properties can be affected by the crystal structure, and different parameters during the experiment can lead to different crystal structures. There will be some defects formed during the formation of the crystal. This means the crystal does not grow as the ideal structure. However, those defects are important for the persistent luminescent because they can store the electrons and release them slowly. During this process, the energy is released in the form of light. Therefore, this project studies how temperatures and pH environments, which are two important parameters during the synthesis of Cr-ZGO, will affect the crystal structures and the optical performance of different structures. To study the optical performance, the Cr-ZGO samples synthesized under different temperatures and pH environments are excited by different wavelengths. Then synchrotron-based techniques are used to determine the local chemical structure of different Cr-ZGO samples. It turns out that Cr-ZGO samples synthesized under 170 ℃ and pH=7 show fewer oxygens surrounding Zn in Cr-ZGO, which will increase the emission intensity. The last part talks about when the surface of Cr-ZGO samples synthesized under different conditions is functionalized by certain function groups, how the optical performance is affected. It turns out samples synthesized under low pH show the strongest light emission after functionalization.

Co-Authorship Statement

The X-ray absorption near-edge structures (XANES) data of Cr, Zn and Ga K-edge from Taiwan Photon Source (TPS) was collected with the help of the beamline scientist Dr. Lo-Yueh Chang at beamline 44A. The XANES data of Cr, Zn and Ga K-edge from Advanced Photon Source (APS) was carried out with the help of beamline scientists Dr. George Sterbinsky and Dr. Tianpin Wu. Dr. Zhiqiang Wang from Western University helped arrange the sample shipping. The X-ray powder diffraction (XRD) data was collected with the help of Dr. Paul D. Boyle from the X-ray Facility, Department of Chemistry, Western University. The Energy Dispersive X-ray Spectroscopy (EDX) is carried out with help from Mr. Clement Lee from the Department of Chemistry, Western University. Photoluminescence (PL) data was collected by the instrument Fluorolog spectrometer from Dr. Zhifeng Ding's group. The Fourier transform infrared spectroscopy (FTIR) was collected by the instrument from the Department of Chemistry, Western University and Dr. Paul Ragogna's group. The revision of the whole thesis is helped with the guidance and advice of Dr. Lijia Liu.

Acknowledgments

First and foremost, I would like to give my most sincere thanks to my supervisor, Dr. Lijia Liu. From my undergraduate project to my graduate project, you always show your best patience to give me unselfish assistance no matter whether it is a weekend or holiday. It's my greatest pleasure to be one of your students. You are the one who shows me how wonderful this scientific research world looks like. I wish I could express my gratitude to you with fancier words. No matter where or what I do in the future, I will always remember you for the help. I could not achieve such great work without you.

I also would like to thank the members of the Department of Chemistry faculty and support staff Mr. Clement Lee, Dr. Tsun-Kong Sham, Dr. Zhifeng Ding, Dr. Paul Ragogna, Mr. Jonathan Ralph Adsetts, Mr. Benjamin Bridge, Mr. Johnathan Lortie, and Dr. Mahdi Hesari. Thank you for your advice and help in the past two years.

Furthermore, I would like to appreciate my examiners reading and evaluating my thesis despite their busy schedules.

Finally, my family gives me all their support and patience. Thank you, my family. Mom and Dad, I hope I am the son you are proud of.

Table of Contents

List of Tables

List of Figures

List of Abbreviations

APS Advanced Photon Source

CB conduction band

CM collimating mirror

Cr-ZGO Cr doped $ZnGa_2O_4$

DCM Double-crystal monochromator

EDX Energy-dispersive X-ray spectroscopy

EXAFS extended X-ray absorption fine structure

FTIR Fourier-transform infrared spectroscopy

PL photoluminescence spectroscopy

PTFE polytetrafluoroethylene

Q-Mono quick-scanning monochromator

TFM toroidal focusing mirror

TPS Taiwan Photon Source

VB valence band

XANES X-ray absorption near edge structure

XAS X-ray absorption spectroscopy

XRD X-ray diffraction

ZGO $ZnGa_2O_4$

UWO University of Western Ontario

Chapter 1

1 Introduction

In this chapter, some foundational background information about the near infrared-emitting persistent luminescent materials, the dopant and the host of Cr-ZGO, the mechanism of Cr-ZGO luminescence, the foundation of the synchrotron radiation-based technique and the objective and arrangement of this thesis will be included.

1.1 Near Infrared-Emitting Persistent Luminescent Materials

Persistent-luminescent materials can be described as optical batteries because they can exhibit long-lasting luminescence for minutes even hours after the excitation sources are removed. The reason why these materials can store light is due to the structure defects as traps. The energy from excitation sources firstly migrates the charge carriers (electrons or the holes created by the migration of electrons) from the ground state. Then those charge carriers are captured by the traps. Finally, the captured charge carriers are released from traps back to the ground state.[1] With the energy releasing during this process, the light is produced. The origin of these structure defects can be caused by (a) heating the materials to a high temperature to form thermal dissociations and disorders, (b) exposing the material to excess pressure, (c) bombarding with high energy rays, electrons, nuclear particles or laser types, concentrations, and (d) doping with impurities and forming crystal defects to accept the dopant.[1] The concentration and depth of the defects will also affect the intensity and lifetime of the luminescence. Generally, the high concentration of defects can trap more charge carriers leading to a stronger emission. Deep traps, on the other hand, release trapped electrons at a considerably slower rate at ambient temperature, and they can even store some carriers, resulting in a phosphorescent emission with a long-lasting lifetime.[1]

In terms of applications, materials with persistent luminescence have widespread applications in the industrial field such as sensors, fluorescent lamps, light emitting diodes (LEDs), or emissive displays for screens.[2-4] However, when the size of persistent-luminescent materials is reduced to nanometer size, they show potential for applications in the biomedical field. Bioimaging, as one of the potential applications of persistent luminescence materials, has drawn scientists' attention.[5-8] Bioimaging is a technique for observing morphological characteristics in tissues at a high resolution. To achieve bioimaging, luminescent probes need to mark cells and emit luminous signals.[9] The ideal materials for this application should have a particle size down to the nanometer scale (normally less than 30 nm), and the luminescent emission should match the transparent window of living tissues (between 600 nm and 1100 nm).[10, 11] In addition, for the biological application, the stability in aqueous solution, the potential to be functionalized for specific binding capability and the luminescent lifetime (normally over hours) need to be considered for the selection of materials. [10, 11] Based on these requirements, organic dyes, chemodosimeters, quantum dots, metal complexes, and persistent luminescent nanomaterials have shown the potential in the field of bioimaging.[9, 10, 12-14] Due to desirable size and outstanding optical properties, persistent luminescent nanomaterials have been developed recently. Normally, this kind of material is inorganic spinel doped with transition metal ions. So far, this kind of material has been developed for two generations. The first generation utilizes silicates and phosphates-based materials. These materials are required to be excited before injection into living bodies by UV light or X-rays so that they could remain luminescent up to one hour after injection.[11, 15-16] For example, Eu^{2+}, Dy^{3+}, Mn^{2+} doped $Ca_{0.2}Zn_{0.9}Mg_{0.9}Si_2O_6$, as one of the first generation persistent luminescent nanomaterials, can be only excited at around 350 nm.[16] On the other hand, because of the intricacy of their chemical composition, it is a challenge to achieve precise stoichiometry control during the materials synthesis.[10, 11] However, the chemical compositions of second-generation materials are simpler, and they can be excited by multiple wavelengths including visible light. For example, Cr doped $ZnGa_2O_4$ (Cr-ZGO), as one of the second generation of persistent luminescent nanomaterials probes, overcomes the disadvantage of the first-generation material. Firstly, there is no need to excite the probe before injection because it can be excited by visible light, which allows the probe to circulate in the living

body's blood vessels for some time and does not waste luminescence duration before reaching the target organ. Moreover, the persistent luminescent property can prevent autofluorescence from living tissues to improve signal/noise ratio. [10, 11]. In addition to these advantages comparing with the first-generation probe, persistent luminescent nanomaterials can also be optimized by functionalization with different types of surfaces. The functionalization can improve the selectivity, stability and biocompatibility of persistent luminescent nanomaterials.[17-20] For instance, miRNA-21 is a bladder cancer-related biomarker. Since DNAs can completely pair with RNA, there has been a study to use miRNA-21 paired DNAs functionalized Mn^{2+} doped Zn_2GeO_4 to label and detect bladder cancer.[17]

1.2 $ZnGa_2O_4$-Based Persistent Luminescent Materials

$ZnGa_2O_4$ (ZGO) is a double oxide with a cubic spinel crystal structure that belongs to the $Fd\overline{3}m$ space group (shown in Figure 1-1).[21] The tetrahedral and octahedral positions are occupied by the Zn and Ga ions, respectively. Pure ZGO has a band gap of 4.4 eV to 4.7 eV, and it is a blue-emitting phosphor.[22, 23] It has been utilized in the solar cell fields to improve light absorption and liquid crystal displays (LCD) due to its light emitting property.[24, 25] The optical property of ZGO can be modified by introducing metal cation dopants. Several dopants have been studied, such as Mn^{2+} and Cr^{3+}. Mn^{2+}-doped ZGO is found to exhibit green light with the persistent luminescent property.[26] Mn^{2+}-doped ZGO shows potential in optoelectronic applications such as field emission displays, electroluminescence displays and vacuum fluorescent display systems.[23, 27] ZGO doped with Cr^{3+} emits NIR emission with persistent luminescent property.[8, 24] Its emission precisely matches the transparent window of living tissues (near IR emission of about 700 nm). This material has been successfully used in the living body for bioimaging. For example, Maldiney, T. et al. have successfully achieved sustained luminescence pictures of a tumor-bearing mouse and recognized the signal in the liver and other organs by injecting Cr doped ZGO and in situ activation.[8] However, scientists still want to improve the emission intensity and lifetime of Cr doped ZGO.

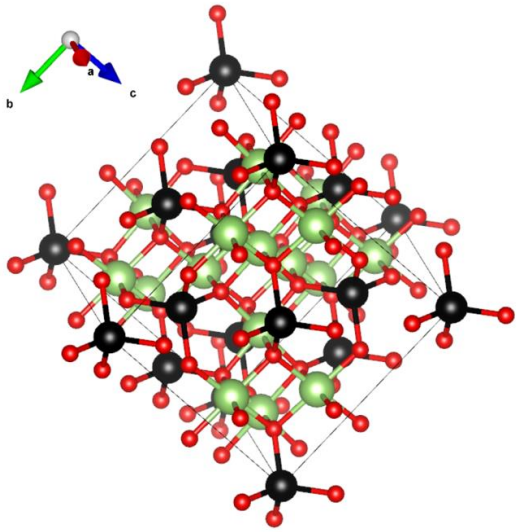

Figure 1- 1. Crystal structure of $ZnGa_2O_4$. The green spheres are Ga; the black spheres are Zn; the red spheres are O.

1.3 Electronic Energy Level of Cr^{3+} in an Octahedral Environment

Cr has various oxidation states from +2 to +6. Cr^{3+} is one of the most common oxidation states, which has an electron configuration of $[Ar]3d^3$ by losing one 4s electron and two 3d electrons. The other common oxidation states are +6 and +2. The elimination of the degeneracy of 3d orbitals separated d orbitals into two groups: t_{2g} (d_{xy}, d_{yz}, d_{zx}) and e_g (d_z^2 and d_x^2-$_y^2$).[29] The coordination of the transition metal and the intensity of the crystal field influence the respective energy positions of t_{2g} and e_g.[29]

The electrons of Cr^{3+} in e_g are directed toward the negative lattice points in octahedral symmetry, whereas the t_{2g} electrons of Cr^{3+} are directed between the point charges of the ligands; however, when the symmetry is tetrahedral, the outcome is the opposite. t_{2g} electrons of Cr^{3+} are directed toward the negative lattice points in tetrahedral symmetry, whereas e_g electrons are directed between the ligands' point charges. In octahedral

symmetry, e_g has a greater energetic position than t_{2g}; whereas, in tetrahedral symmetry, t_{2g} has a higher energetic position than e_g.[30]

In the octahedral symmetry, three unpaired electrons in t_{2g} orbitals generate $^4A_{2g}$, ^2E_g, $^2T_{1g}$, and $^2T_{2g}$ states, and $^4A_{2g}$ is the ground state. When one electron is excited to the e_g state, two quartet states ($^4T_{1g}$ and $^4T_{2g}$) are formed (shown in Figure 1-2). One quartet state $^4T_{1g}$ will be generated when two electrons are stimulated to the e_g state.[28,30]

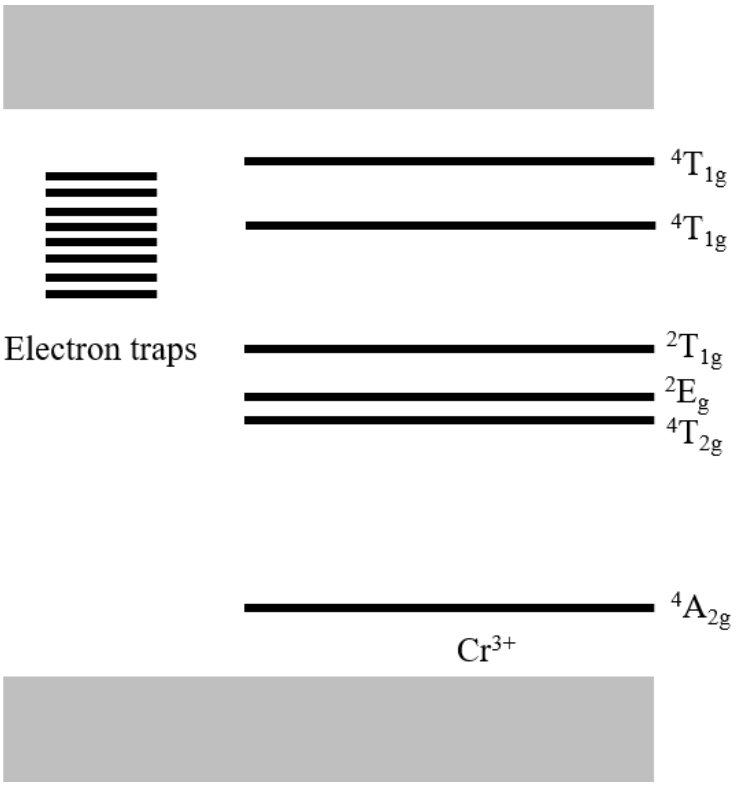

Figure 1- 2. The energy diagram of Cr^{3+} in the octahedral symmetry.[28]

1.4 Cr-ZGO Luminescence Mechanism

When Cr^{3+} is doped in $ZnGa_2O_4$ host, there have been studies pointing out that the Cr^{3+} ions will replace the position of Ga at octahedral sites because the ionic radius of Ga^{3+} (0.615 Å) and the size of Cr^{3+} ions (0.62 Å) are similar, which makes $ZnGa_2O_4$ become a

suitable host for Cr dopant.[31, 32] Although there is still much uncertainty about the mechanism of Cr-ZGO luminescence, a general mechanism has been proposed.[8, 33-35] As previously discussed, defects play an essential role in luminescence. Sometimes the Zn and Ga ions will exchange their positions, which means Ga cations occupy the tetrahedral positions, and Zn cations occupy the octahedral positions. This is called anti-site defect. A Ga ion in a Zn site will produce a positively charged defect (Ga_{Zn}°) and Zn in a Ga site is a negatively charged defect ($Zn_{Ga}^{'}$).[8] After being excited by an external energy source, electrons from Cr^{3+} ions are firstly promoted to $^4T_2$ excited states (step 1 in Figure 1-3), and then the excited Cr^{3+} will redistribute the charge in the $Zn_{Ga}^{'}$ – Cr^{3+}–Ga_{Zn}°, which will neutralize the anti-site defects, and the charge carrier (electron–hole pair) will be trapped nearby Cr^{3+} as neutral anti-site defects (step 2 (a) and (b) in Figure 1-3). The thermal activation process will let the excited electrons return to the ground state from ^2E state through a reversed way of step 1 and 2 (step 3 (a) and (b) and step 4 in Figure 1-3). [8]

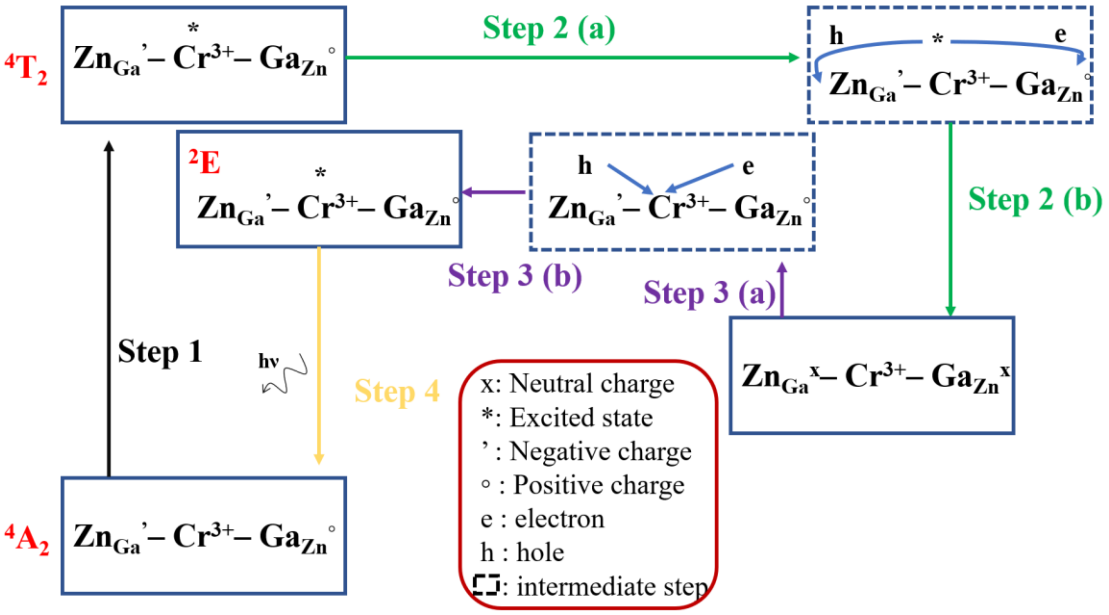

Figure 1- 3. Mechanism of Cr-ZGO luminescence.[6]

1.5 Synchrotron Radiation

The synchrotron can emit various wavelengths of light from infrared (IR) to hard X-Ray light. To achieve the hard X-Ray light (X-rays with the energy of several keV and higher), such high energy is obtained by accelerating the electrons to nearly the speed of light around a ring by the utilization of radio frequency waves and powerful electromagnets. It can be used to investigate the structural and chemical characteristics of materials at the molecular level.[36] When the trajectory of the electrons is bent, energy is released in the form of light. Figure 1-4 depicts the layout of a synchrotron radiation facility schematically.[37] Firstly, the electrons are created by the electron gun in the center of the ring. The linear accelerator will accelerate the electrons to nearly the speed of light with mega electron-volt energy. After that, the booster ring will further accelerate electrons up to giga-electron volt energy. Once the electrons reach to desired energy, they get into the storage ring in an ultra-high vacuum vessel. To balance the energy loss, a radio frequency electric field is applied to replenish the energy.[37]

Generally, the storage ring is more like a collection of long straight sections made by regions with magnets. An external magnetic field can potentially disturb an electron's path in the straight section. X-ray beams with specified spectral, temporal, and spatial features can be created by so-called linear insertion devices known as undulators and wigglers by carefully manipulating the orbital perturbations. With the help of specialized dipole and multipole magnets, high energy electrons are circulated and stored in a stable orbit in the storage ring.[37]

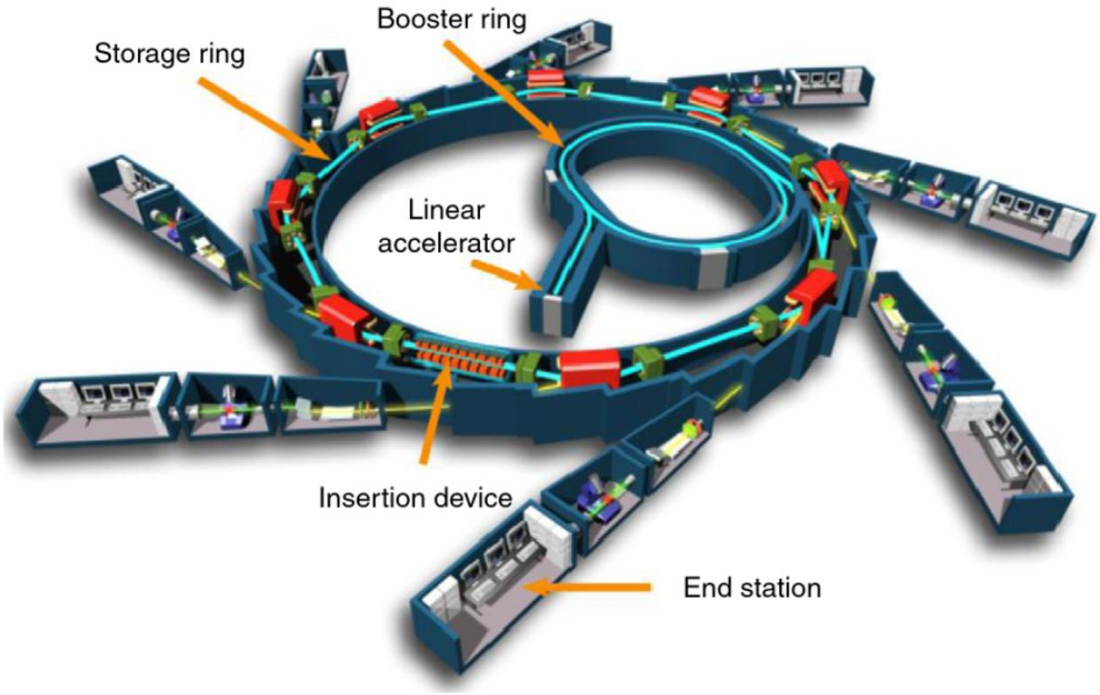

Figure 1- 4. The layout of a synchrotron facility.[37]

An accelerated charged particle with a curved trajectory will emit radiation, and when relativistic electrons are accelerated in a magnetic field, synchrotron radiation will be produced as a narrow cone tangent to the path of the particle, and the emission angle can be controlled by the magnetic field to further control the range of radiation spectrum. Normally, there are three kinds of magnetic structures, which are bending magnets, undulators and wigglers. The bending magnets radiation will produce a narrow radiation cone directing the radiation tangentially outward with an extraordinarily broad radiation spectrum. The undulators radiation will produce an extraordinarily narrow, which is narrower than the bending magnets radiation with a narrower radiation spectrum. Wigglers radiation also produces the broad radiation cone. The radiation spectrum is broad at higher energy than bending magnets radiation.[38]

During the experiment, a monochromator is essential for the selection of energy. Typically, grating monochromator and double-crystal monochromator are utilized for soft X-rays (above 5–10 keV) and hard X-rays (greater than around 10 keV) respectively. Figure 1-5 demonstrates how the energy selection is achieved using the grating monochromator.

When the polychromatic incident light hits the grating monochromator at a grazing angle, diffracted light with different angles will be produced according to equation 1-1, where α is the angle of incidence; β is the angle of diffraction; n is the order of the diffraction; λ stands for the wavelength of the diffraction light; d is the distance between the grating lines. Therefore, the grating monochromator can be rotated to select the desired wavelength.

$$n\lambda = d(\sin\ \alpha \pm \sin\ \beta) \qquad \textbf{(Equation 1-1)}$$

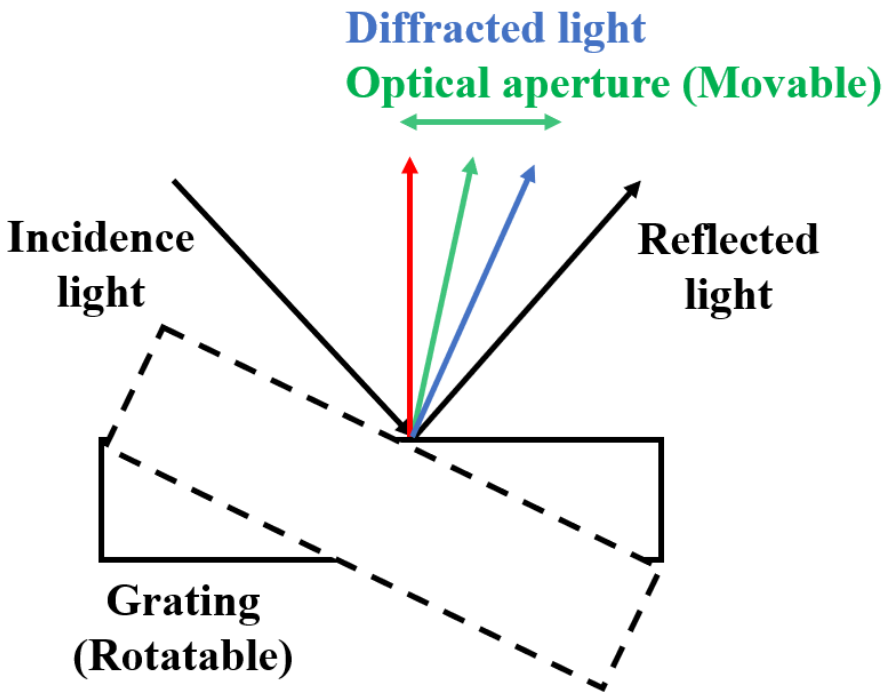

Figure 1- 5. Schematic diagram of how soft X-ray is selected by the grating monochromator.

In terms of hard X-rays, a double-crystal monochromator is utilized. A double-crystal monochromator is made by two parallel crystals with the same physical parameters. By adjusting the angle of the crystals, the incidence light with a fixed angle can be obtained. The first crystal can be adjusted to have varied incidence beam angles (θ) (Figure 1-6 (a)), and the second crystal can rotate and translate the Bragg diffracted beam to the fixed exit

point (Figure 1-6 (b)). Based on Bragg's law (Equation 1-2), mono-energy X-ray with constructive interference can be achieved.

$$n\lambda = 2d\sin\ \theta \qquad \text{(Equation 1-2)}$$

where n is the order of diffraction; λ represents the wavelength of the diffracted light; d stands for the lattice spacing of the crystal; θ is the Bragg angle.

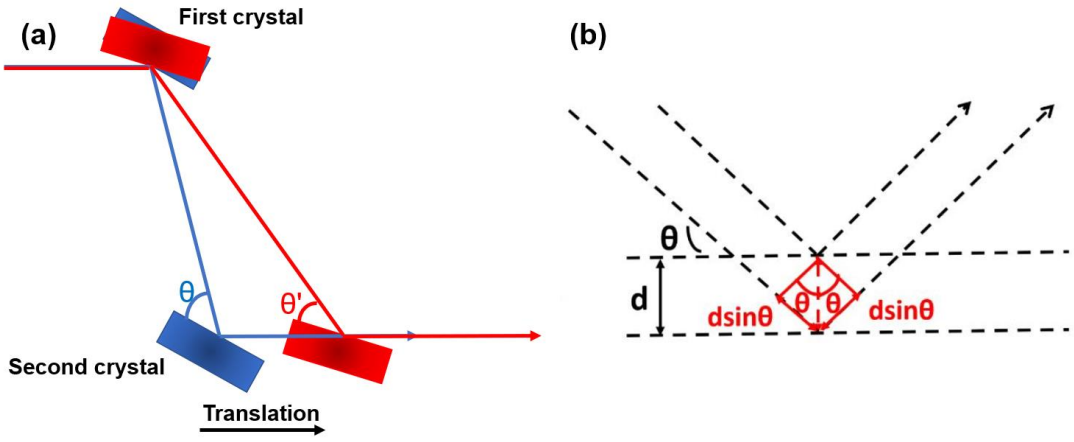

Figure 1- 6. Schematic diagram of (a) double-crystal monochromator and (b) illustration of Bragg diffraction.[25]

1.6 Objective and Arrangement of Thesis

In this project, the objective will be to investigate the relationship among synthetic environments, optical properties and structure for Cr^{3+} doped $ZnGa_2O_4$ (Cr-ZGO) samples. For the experimental part, the Cr-ZGO will be synthesized under different synthetic environments (different temperatures and pH values) and functionalized with different function groups by the hydrothermal method. In terms of structure, synchrotron radiation will be utilized to investigate the influence on the structure of Cr-ZGO.

There will be six chapters in this thesis. For the first chapter, a general introduction and background of (1) near infrared-emitting persistent luminescent materials, (2) $ZnGa_2O_4$-based persistent luminescent materials, especially (3) luminescence mechanism Cr doped $ZnGa_2O_4$, (4) outline of synchrotron radiation and objective of this thesis will be discussed. Chapter 2 will describe detailed information on synchrotron-based characterizations such as X-ray absorption near edge structure (XANES) and extended X-ray absorption fine structure (EXAFS). In addition, the laboratory techniques used in this thesis such as photoluminescence spectroscopy (PL), X-ray powder diffraction analysis (XRD), energy-dispersive X-ray spectroscopy (EDX) and Fourier-transform infrared spectroscopy (FTIR) will be introduced. After that, the investigation of the influence of synthesis temperature and pH on the electronic structure and luminescence of Cr-doped $ZnGa_2O_4$ will be presented in chapters 3 and 4. In chapters 3 and 4, the information of optical properties obtained by PL and electronic structure obtained by X-ray absorption spectroscopy (XAS) will be summarized and combined with synthetic environments. Chapter 5 will display how the functionalization will affect the Cr-ZGO under different synthetic environments. Finally, a conclusion of this thesis and proposed future work will be included in chapter 6.

1.7 References

[1] Li, Y., Gecevicius, M., Qiu, J., *Chem. Soc. Rev.* **2016**, 45, 2090–2136.

[2] Terraschke, H., Wickleder, C. *Chem. Rev*. **2015**, 115, 11352–11378.

[3] Zheng, Y., Chen, D. *J. Lumin*. **2011**, 26, 481–485.

[4] Salah, N., Habib, SS., Khan, ZH. *J. Fluoresc*. **2010**, 20, 1009–1015.

[5] Abdukayum, A., Chen, J-T., Zhao, Q., Yan, X-P. *J. Am. Chem. Soc*. **2013**, 135, 14125–14133.

[6] Maldiney, T., Lecointre, A., Viana, B., Bessière, A., Bessodes, M., Gourier, D., Richard, C., Scherman, D. *J. Am. Chem. Soc*. **2011**, 133, 11810–11815.

[7] Palner, M., Pu, K., Shao, S., Rao, J. *Angew. Chem. Int. Ed*. **2015**, 54, 11477–11480.

[8] Maldiney, T., Bessière, A., Seguin, J., Teston, E., Sharma, SK., Viana, B., Bos, AJJ., Dorenbos, P., Bessodes, M., Gourier, D., et al. *Nat. Mater*. **2014**,13, 418–426.

[9] Yang, Y., Zhao, Q., Feng, W., Li, F., *Chem. Rev*. **2013**, 113, 192–270.

[10] Dhoble, S. J., Raju, B. D. P., Singh, V., *Phosphors : synthesis and applications*. First edition.; Pan Stanford Publishing, Singapore, 2018.

[11] Wang, Y., Wu, A., Tan, K., Lu, X. *J. Comput. Chem.* **2019**, 40, 1038-1044.

[12] Lu, Y., Su, Y., Zhou, Y., Wang, J., Peng, F., Zhong, Y., Huang, Q., Fan, C., He, Y., *Biomaterials.* **2013**, 34, 4302–4308.

[13] Xue, Z., Li, X., Li, Y., Jiang, M., Ren, G., Liu, H., Zeng, S., Hao, J., *Nanoscale*. **2017**, 9, 7276–7283.

[14] Zhang, F., Tang, B., *Chem. Sci. (Cambridge)*. **2021**, 12, 3377–3378.

[15] Sun, S-K., Wang, H-F., Yan, X-P. *Acc. Chem. Res*. **2018**, 51, 1131–1143.

[16] le Masne de Chermont, Q., Chaneac, C., Seguin, J., Pelle, F., Maitrejean, S., Jolivet, J-P., Gourier, D., Bessodes, M., Scherman, D. *Proc. Natl. Acad. Sci. U.S.A.* **2007**, 104, 9266–9271.

[17] Wang, Y., Li, Z., Lin, Q., Wei, Y., Wang, J., Li, Y., Yang, R., Yuan, Q. *ACS Sens*. **2019**, 4, 2124–2130.

[18] Ramírez-García, G., d'Orlyé, F., Gutiérrez-Granados, S., Martínez-Alfaro, M., Mignet, N., Richard, C., Varenne, A. *Colloids Surf. B*. **2015**, 136, 272–281.

[19] Feng, F., Chen, X., Li, G., Liang, S., Hong, Z., Wang, H-F. *ACS Sens*. **2018**, 3, 1846–1854.

[20] Fu, X., Liu, C., Shi, J., Man, H., Xu, J., Zhang, H. *Opt. Mater*. **2014**, 36, 1792–1797.

[21] Bessière, A., Jacquart, S., Priolkar, K., Lecointre, A., Viana, B., Gourier, D. *Opt. Express.* **2011**, 19, 10131–10137.

[22] Shawuti, S., Can, MM., Gülgün, MA., Fırat, T. *Electrochim. Acta*. **2014**, 145, 132–138.

[23] Hasabeldaim, EH., Menon, SG., Swart, H., Kroon, R. *Vacuum*. **2021**, 192, 110447–.

[24] Tuerdi, A., Abdukayum, A., *RSC Adv.* **2019**, 9, 17653–17657.

[25] HIRANO, M., *J. Mater. Chem*. **2000**, 10, 469–472.

[26] Feng, Y., Deng, D., Zhang, L., Liu, R., Lv, Y. *Sens. Actuators B Chem*. **2019**, 279, 189–196.

[27] Somasundaram, K., Abhilash, K., Sudarsan, V., Christopher Selvin, P., Kadam, R. *Phys. B: Condens. Matter*. **2016**, 491, 79–83.

[28] Ogasawara, K., Alluqmani, F., Nagoshi, H. *ECS J. Solid State Sci*. **2015**, 5, R3191–R3196.

[29] Kalisky, Y., *Solid state lasers : tunable sources and passive q-switching elements*. SPIE Press., Bellingham, Washington, 2014.

[30] Lakshmi Reddy, S., *Electronic (Absorption) Spectra of 3d Transition Metal Complexes*. IntechOpen; 2012.

[31] Fernández-Osorio, A., Tapia, M., Vázquez-Olmos, A., Chávez, J. *J. Solid State Chem*. **2019**, 269, 328–335.

[32] Mian, F., Bottaro, G., Wang, Z., You, Y-M., Rancan, M., Sham, T-K., Armelao, L. *Appl. Surf. Sci.* **2022**, 577, 151896 –

[33] Li, L., Wang, Y., Li, H., Huang, H., Zhao, H. *RSC Adv*. **2015**, 5, 57193–572.

[34] Zhou, Z., Zheng, W., Kong, J., Liu, Y., Huang, P., Zhou, S., Chen, Z., Shi, J., Chen, X. *Nanoscale*. **2017**, 9, 6846–6853.

[35] da Silva, MN., de Carvalho, JM., de Abreu Fantini, MC., Chiavacci, LA., Bourgaux, C. *ACS Appl. Nano Mater*. **2019**, 2, 6918–6927.

[36] Parkinson, D., Uchida, M., Gros, M., Larabell, C., Knoechel, C., McDermott, G. *Visualizing Sub-cellular Organization Using Soft X-ray Tomography*. *Comprehensive Biophysics*. 2012; 2: 90–110.

[37] Le Gros, M., Knoechel, C., Uchida, M., Parkinson, D., McDermott, G, Larabell, C. *2.6 Visualizing Sub-cellular Organization Using Soft X-ray Tomography*. In: Comprehensive Biophysics. Elsevier B.V, 2012. p. 90–110.

[38] Attwood, DT., Sakdinawat, A., Geniesse, L. *X-rays and extreme ultraviolet radiation : principles and applications*. Second edition.; Cambridge: Cambridge University Press, 2016.

Chapter 2

2 Characterization Techniques

In this chapter, all the characterization techniques used in this thesis will be introduced including TPS and APS photon sources, hydrothermal method, X-ray absorption spectroscopy, energy dispersive X-ray, X-ray diffraction, photoluminescence spectroscopy and Fourier-transform infrared spectroscopy.

2.1 Synchrotron Radiation Facilities and Beamlines

2.1.1 The Advanced Photon Source (APS)

The Advanced Photon Source (APS) is located at Argonne National Laboratory in Lemont, Illinois, USA, which is a third-generation synchrotron x-ray radiation source. It is a 7 GeV ring, whose circumference is 1104 m. Figure 2-1 shows the layout of the APS facility. As of June 2022, there are 34 sectors distributed around the storage ring, and each sector has at least one beamline. [1, 2] In this thesis, the X-ray absorption fine structure (XAFS) data from APS was collected at beamline 20-BM. Its schematic layout is shown in Figure 2-2. X-rays at this beamline are originated from a bending magnet, with energies ranging from 2.7 keV to 35 keV.[3,4] The energy selection is achieved through Si (111) double crystal monochromator (DCM). It has detectors such as ionization chambers, multi-element Ge detector, Vortex Si drift detector, Si diodes and Area detector. In this project, the Cr K-edge XANES, Zn K-edge EXAFS, and Ga K-edge EXAFS were measured in this beamline.

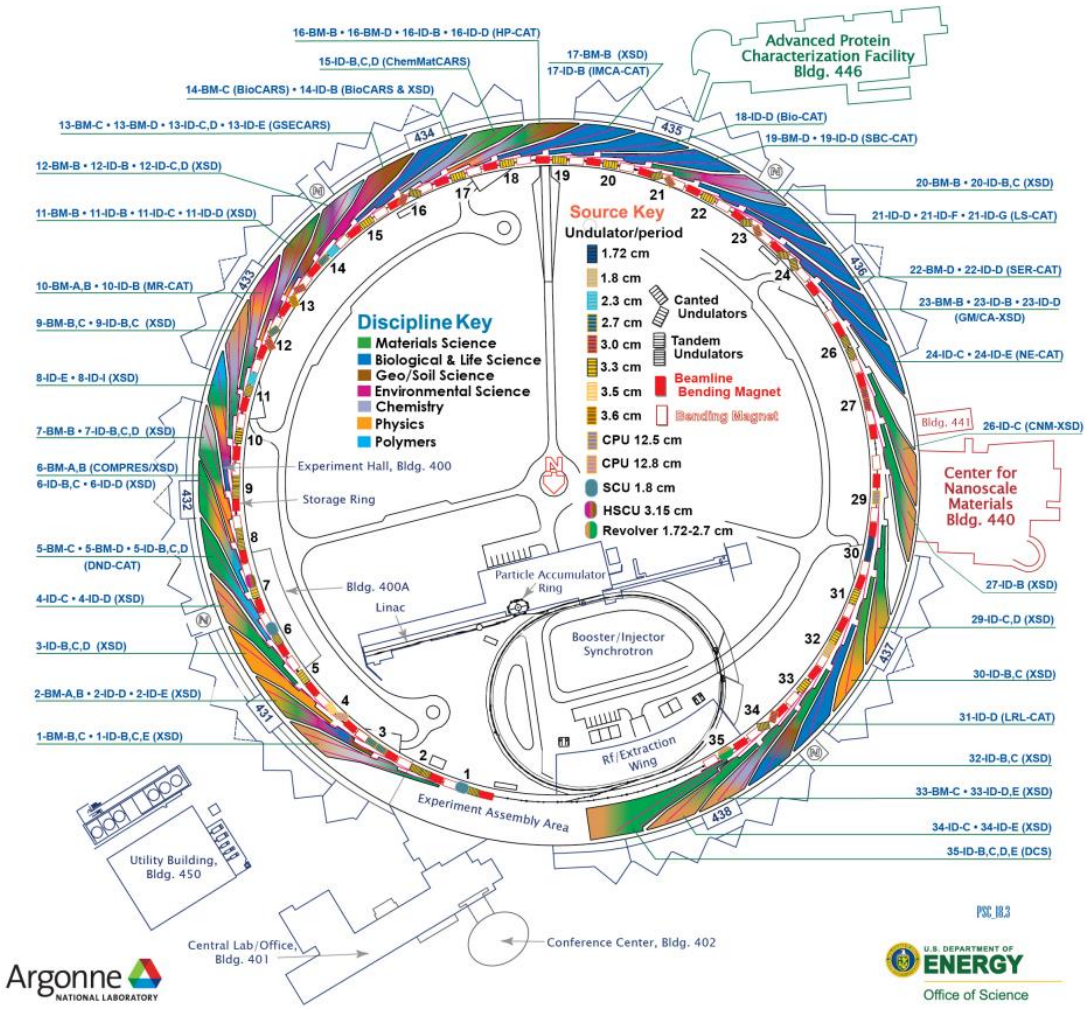

Figure 2- 1. The layout of the APS.[2]

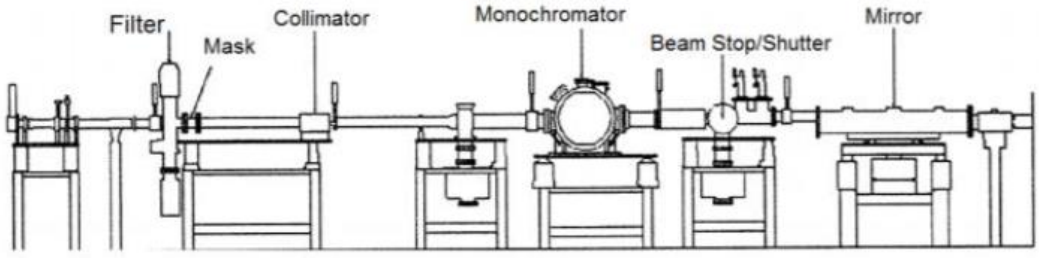

Figure 2- 2. The schematic diagram of the 20-BM at APS.[4]

2.1.2 Taiwan Photon Source (TPS)

Taiwan Photon Source (TPS) locates in Hsinchu, Taiwan, China. It is a 3.0 GeV storage ring with a circumference of 518.4 meters. Figure 2-3 shows the layout of TPS.[5] As of June 2022, there are 16 active beamlines in use, and 9 beamlines still under construction. In this thesis, the X-ray absorption fine structure (XAFS) data from APS was collected at the 44A beamline. This beamline uses a bending magnet for the study of physics, chemistry, biology, environment and arts. For in situ time-resolved measurements and conventional XAS investigations, this beamline offers the capacity for quick scanning and step-by-step scanning, respectively. It only takes less than 100 milliseconds over 1000 eV to take acquire a full quick-scanning EXAFS spectrum.[6] This beamline can produce energy from 4.5 – 34 keV. As shown in Figure 2-4, the 44A beamline is mainly made up of optical devices including a collimating mirror (CM), a quick-scanning monochromator (Q-Mono), a toroidal focusing mirror (TFM) and a set of K-B mirrors. The CM is used for the collimation of the vertical beam and increasing the resolving power of the monochromator. Q-mono is used to select the photon energy. TFM can focus the incoming light at the first sample position. At the second sample position, K-B mirrors are set for the micro-beam experiments.[7]

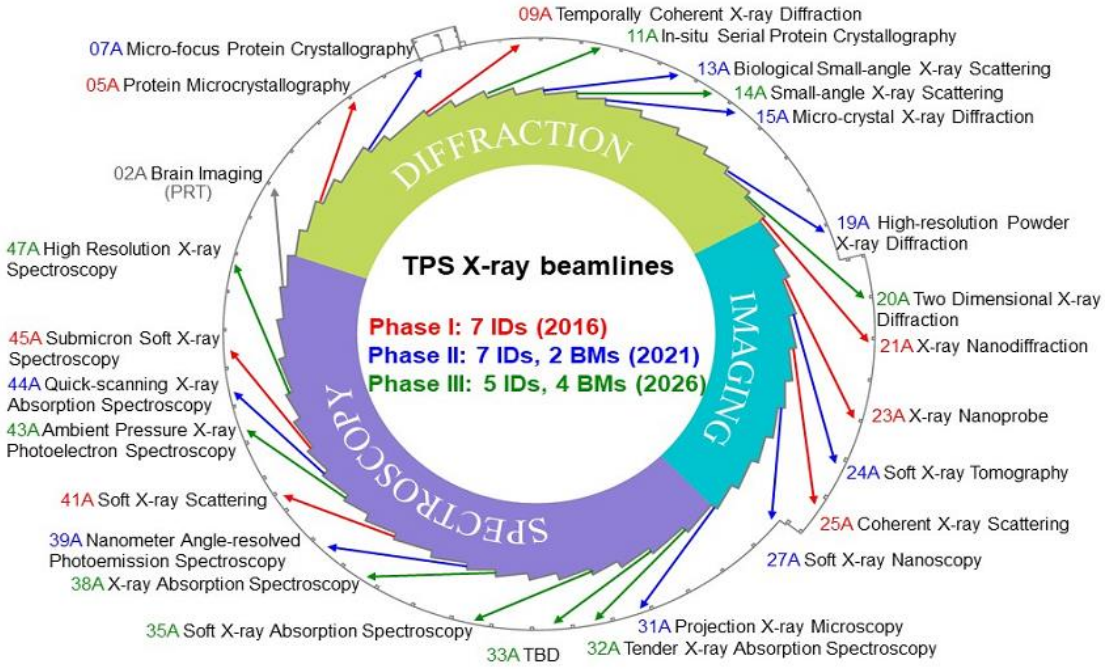

Figure 2- 3. The layout of TPS.[5]

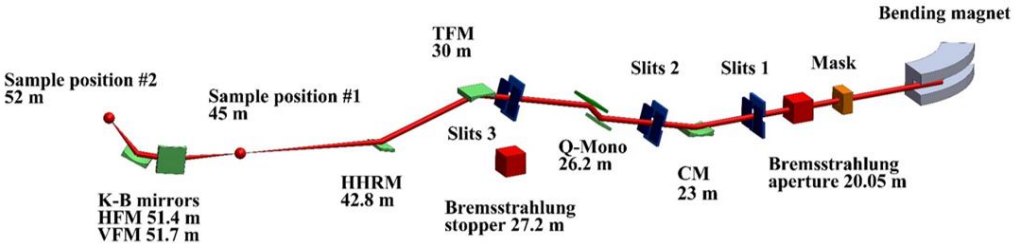

Figure 2- 4. The optical layout of beamline 44A in TPS.[7]

2.2 Hydrothermal Method

The hydrothermal method is one of the most commonly used aqueous-phase nanomaterials synthetic methods. It refers to the heterogeneous reaction of inorganic materials to form crystals by solubility changes of substances in the sealed aqueous solution above ambient room temperature and pressure.[8-10] There are some advantages of the hydrothermal method

such as low-temperature requirement comparing with the solid state reaction, cheap cost, and no requirement for metal catalysts.[11, 12] In addition, it is very suitable to synthesize nano-size particles, which is a fundamental requirement for the biological applications. The reaction happens in a hydrothermal synthesis autoclave reactor with a polytetrafluoroethylene (PTFE) lined vessel (shown in Figure 2-5) with temperatures between the boiling and critical points of water from 100 to 374 ℃ and at elevated pressures (up to ca. 15 MPa).[12] It is suitable for the synthesis of fine and uniform powders like nanoparticles with excellent homogeneity.

Figure 2- 5. Hydrothermal synthesis autoclave reactor with polytetrafluoroethylene (PTFE) lined vessel.

The hydrothermal method is a commonly used method to synthesize Cr doped $ZnGa_2O_4$ (Cr-ZGO) due to the formation of small size crystals.[13-17] In this project, the Cr-ZGO is synthesized by following these steps: $Ga(NO_3)_3$ (0.0025 mol) and $Zn(NO_3)_2$ (0.00125mol) were dissolved in 5ml DI water in two separated vials individually. When all the solid was dissolved adequately, $Zn(NO_3)_2$ solution was added into $Ga(NO_3)_3$ solution with vigorously stirring. 500 μL $Cr(NO_3)_3$ stock solution, made by $Cr(NO_3)_3$ (0.0001 mol) in 10 ml DI water, was mixed with $Ga(NO_3)_3$ and $Zn(NO_3)_2$ solution. The mixture was stirred for a half-hour. The pH adjustment was done by the addition of ammonium hydroxide (28 wt%). Once the target pH was reached, the mixture was stirred for 30 min and put into an autoclave and heated at a constant temperature for 10 hours to react. When the solution is

cooled to room temperature, the precipitate was collected by centrifuge at 4500 rpm for 5 min. The 5 ml 0.1 M HCl is added into centrifuge tube, and the centrifuge tube is shaken to wash the precipitate. The precipitate is separated by centrifuge at 3500 rpm for 5 min. Then 10 ml 2-propanol is used to wash the sample again. The washed samples were dried under 60 ℃ for 10 hours.

2.3 X-ray Absorption Spectroscopy

When a sample is bombarded with X-rays, by comparing the intensity of the incident and transmitted beams or by measuring the electrons or photons produced during the relaxation process, the absorption coefficient of the material can be determined according to Beer's Law (shown in Equation 2-1),

$$\frac{I_t}{I_0} = e^{-\mu t} \qquad \textbf{(Equation 2-1)}$$

where I_0 is the intensity of incident X-rays; I_t is the intensity of transmitted X-rays; t is the thickness of the sample; μ is the absorption coefficient, which can be described by equation 2-2:

$$\mu = \sigma \cdot \rho \qquad \textbf{(Equation 2-2)}$$

Where σ is the absorption cross section and ρ is the density of the sample. By monitoring the modulation of μ with the change of the excitation X-ray energy, an X-ray absorption spectrum (XAS) is obtained. When the energy of the incident X-ray is slightly over the core electron's binding energy, it will lead to a significant increase of cross section σ and therefore the absorption coefficient. This abrupt change will cause an absorption edge. In other words, the absorbed X-rays energy by the atom is sufficiently high to overcome the binding energy of core electrons of the atom. These electrons will be excited to an unoccupied bound state, quasi-bound state and further to the continuum with the increase of the energy of the incident X-ray. [17] Figure 2-6 indicates absorption edges in the plot of absorption coefficient as a function of wavelength.[18] The absorption edges are labeled based on the quantum number of the shell. The K-edge represents the excited electron is

from 1s orbital (N=1); the excitation of an electron from the 2s, $2p_{1/2}$, and $2p_{2/3}$ orbitals is represented by the $L_{1,2,3}$-edge, respectively (N=2); the excitation of an electron from a 3d orbital is labeled as M-edge (N=3). Therefore, X-ray absorption spectroscopy (XAS) or X-ray absorption fine structure (XAFS) can be seen above the absorption edge, which is defined as the energy-dependency of the absorption coefficient.[19]

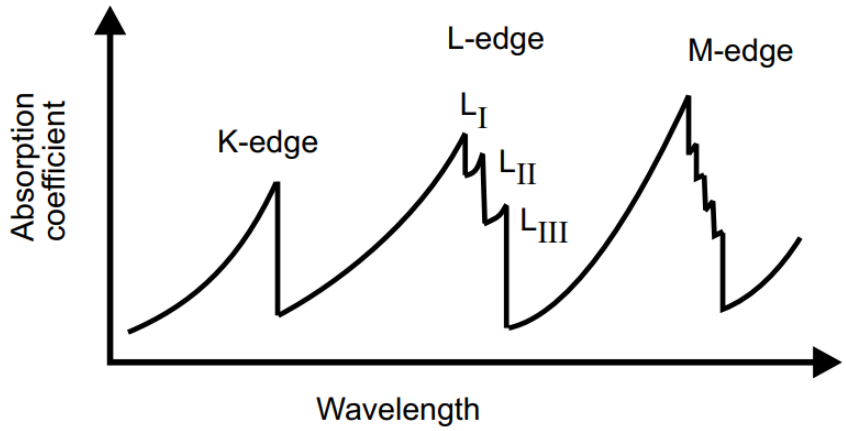

Figure 2- 6. The absorption edges in the plot of absorption coefficient as a function of wavelength.[18]

The XAS can be divided into two parts: X-ray absorption near edge structure (XANES) and extended X-ray absorption fine structure (EXAFS). The XANES relates to the absorption of the sample with excitation energy from a few eV below the absorption edge until ~50 eV above the edge (Figure 2-7). The XANES contains electronic transitions of a specific core-level electron to bound and quasi-bound states, as well as multiple scattering among adjacent atoms. XANES contains information such as the occupation of electronic state, symmetry, and geometry for the absorbing atom, which could be obtained by analyzing the energy position of the absorption edge and shape of the spectra.[20 to 22]

The EXAFS refers to the absorption spectrum at excitation energy 50 eV to 1000 eV above the edge. Before exiting the system, the high-energy photoelectron is usually scattered once by surrounding atoms shown in Figure 2-7 Therefore, EXAFS is sensitive to local structure within the adjacent atoms. The structure parameter such as interatomic distances and coordination numbers can be quantitatively obtained by analyzing the post-edge oscillation

patterns. By conversion of energy to the wave number of the photon electrons (k) according to Equation 2-3:

$$k = \frac{\sqrt{2m(E-E_0)}}{\hbar^2} \qquad \textbf{(Equation 2-3)}$$

where E_0 is the absorption edge energy; m is the electron mass and $\hbar$ is Planck's constant. The oscillation as a function of photonelectron wave number is called K-space described by Equation 2-4.

$$\chi(k) = \sum_j \left[\frac{N_j S_0^2 f(k,\theta) e^{-2R_j/\lambda_e(k)} e^{-2k^2\sigma_j^2}}{kR_j^2}\right] \sin\left[2kR_j + \phi(k)\right] \qquad \textbf{(Equation 2-4)}$$

where N_j is the coordination number of the atom; S_o^2 is the amplitude reduction term, which describes processes that affect the X-ray absorption coefficient but do not contribute to the EXAFS.[23] f (k, θ) is atomic scattering amplitude; $e^{-2R_j/\lambda_e(k)}$ and $e^{-2k^2\sigma_j^2}$ amplitude damping terms due to electron escape depth λ_e and mean displacement due to thermal motion σ_j, respectively; R_j is interatomic distance; $\Phi(k) = 2\delta_a(k) + \delta_b(k)$ is the phase function with contributions from the absorber $\delta_a(k)$ and the back-scatterer $\delta_b(k)$. K-space is always transformed to R-space to acquire information on the local structure by the Fourier transform. During the Fourier transform, the amplitude is as a function of neighboring distance, and information such as bond lengths and coordination numbers can be extracted.[24]

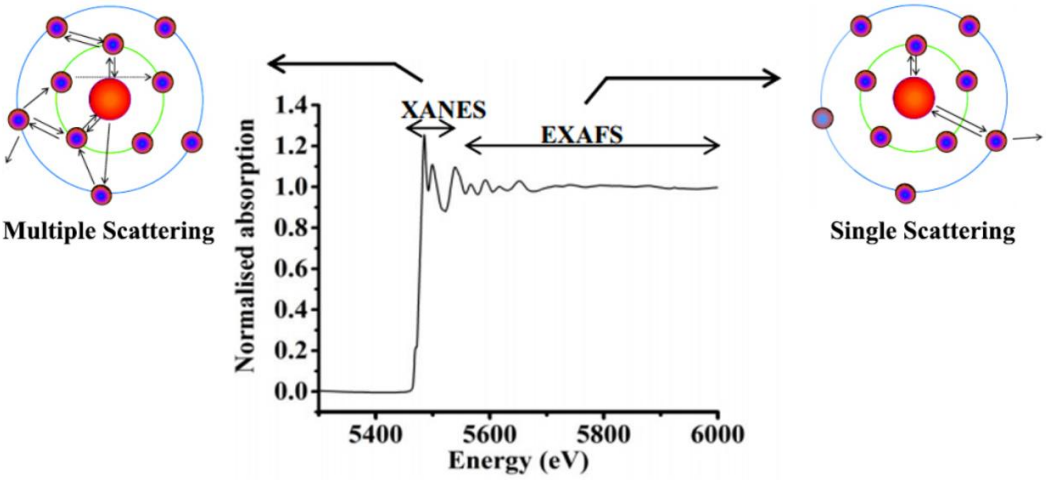

Figure 2- 7. schematic drawing for XANES and EXAFS with multiple and single scattering.[24]

2.4 Energy Dispersive X-ray Spectroscopy (EDX)

For elemental speciation and concentration quantification, energy dispersive X-ray (EDX) is utilized. It is an analytical method by tracking the fluorescence X-rays emitted from elements in the sample. When the electron beam hits the sample, the electron in the inner shell of the element in the sample will be excited and ejected, leaving a hole.[25] An electron from an outer shell will fill the hole, emitting X-ray photon with energy equal to the difference between the two energy levels. This energy is characteristic of the atomic structure of the emitting element, which allows to identify the elements. [26] The EDX in this project was taken at the Nanofabrication facility at Western using an attachment of a scanning electron microscope (LEO (Zeiss) 1540XB FIB/SEM).

2.5 X-ray Diffraction (XRD)

X-ray diffraction (XRD) is extensively utilized in crystal structure determination. The technique takes advantage of the fact that X-ray wavelengths are similar to the interatomic

spacing of crystalline solids.[27] As shown in Figure 2-8, the diffraction of an incoming X-ray beam through a crystal produces a distinct pattern, and the diffraction of X-rays by a crystal is described by the Bragg law shown in Equation 2-6 where λ is the wavelength of the incident X-ray (e.g., 0.179nm for Co Kα); d is the lattice spacing; θ is the angle of diffraction; n is the positive integer (the order of diffraction).

$$n\lambda = 2d\sin\ \theta \qquad \textbf{(Equation 2-6)}$$

The peak position in an XRD pattern is related to interplanar distance (d) between parallel planes of atoms. The relative phases of waves from nearby planes determine the intensity of X-rays diffracted from one crystal plane, indicating the geometrical structure in a unit cell.[28] The XRD in this project was taken at the X-ray Facility at the Chemistry Department of Western University. The apparatus is equipped with a Cu Kα sealed tube source, an Inel XRG3000 generator, and an Inel CPS 120 detector.

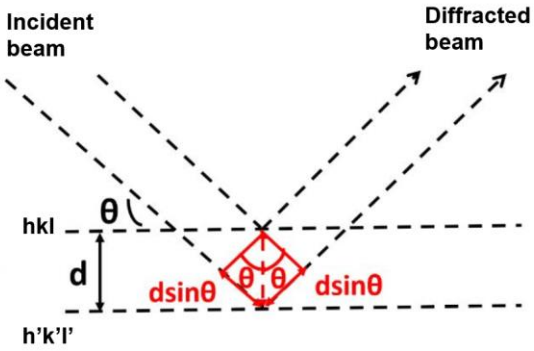

Figure 2- 8. The diffraction of X-ray beam through a crystal.

The crystalline sizes can be calculated by using the Scherrer equation (Equation 2-7) where D is the average crystallite size; λ is the wavelength of the incident X-ray beam; B is the full width at half of the maximum intensity of the reflection peak; θ is the angle of diffraction.

$$D = \frac{0.9\,\lambda}{B\cos\theta} \qquad \textbf{(Equation 2-7)}$$

2.6 Photoluminescence

Photoluminescence (PL), as an example of a non-heat-related electrical process that produces luminescence, refers to using light energy or photons to excite the emission of a photon from any matter. Photons are absorbed by electrons, promoting the electronic transition to an excited state. When the electrons return to the ground state, PL is produced. In terms of inorganic semiconductors, there are two kinds of PL, which are intrinsic PL and extrinsic PL. The intrinsic PL happens mostly owing to band-to-band radiative transitions in a pure semiconductor. The extrinsic PL can occur between free carriers and impurities or defect states.[29]

With this photoluminescence property, the optical properties of materials can be studied by photoluminescence spectroscopy. When the sample is exposed to the light with a particular wavelength and generates PL, an emission scan of photoluminescence spectroscopy can be obtained. In an inverse way, the detector can monitor a particular wavelength emitted from the sample. By exposing the sample to a range of wavelengths, an excitation scan of photoluminescence spectroscopy can tell us which wavelengths can excite the sample. The PL in this thesis was collected with Fluorolog spectrometer (QM-7/2005, Photon Technology Internation (PTI)).

2.7 Fourier-transform Infrared Spectroscopy (FTIR)

Fourier-transform infrared spectroscopy (FTIR) measures the infrared-light-absorption capability of a sample. The fundamental principle of this technology is that each functional group contains certain bonds, and the stretches and compresses of a certain bond can only be achieved by a certain vibrational frequency. This allows us to know the types of functional groups by knowing the vibrational frequency they show up in the IR spectrum.

The working principle of the instrument can be explained as following. A beam splitter divides the fixed and movable mirrors, allowing a collimated beam of light from an external source to be partially reflected (at point F) and partially transmitted to the moveable mirror (at point M) shown in Figure 2-9. When the beams return to the beamsplitter, they collide

and are partially reflected and partially transmitted once more. The intensity of each beam travelling to the detector and returning to the source is determined by the difference in the path of the beams due to interference. The FTIR spectrum information is obtained by varying the intensity of the beams going to the detector and returning to the source as a function of the route difference.[30] The FTIR can provide information such as the structural elucidation of organic compounds. Attenuated Total Reflection (ATR) sampling revolutionized Fourier transform infrared spectroscopy (FTIR) in this thesis was collected by ALPHA II Compact FT-IR Spectrometer and OPUS software.

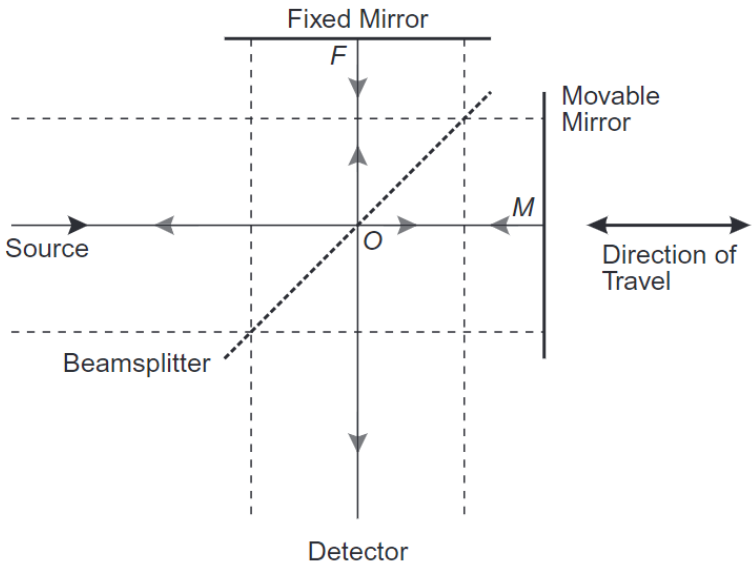

Figure 2- 9. The working principle of the Fourier-transform infrared spectrometry.[30]

2.8 References

[1] The Advance Photon Source List of Parameters, compiled by H. M. Bizek, July1996.http://www.aps.anl.gov/Science/Publications/techbulletins/content/files/APS_1421579.pdf (accessed by June 7th. 2022)

[2] Beamlines Map. https://www.aps.anl.gov/Beamlines/Beamlines-Map (accessed byJune 7th. 2022)

[3] Spectroscopy: Beamline 20-BM. https://www.aps.anl.gov/Spectroscopy/Beamlines/20-BM (accessed by June 7th. 2022)

[4] Heald, SM., Brewe, DL., Stern, EA., Kim, KH., Brown, FC., Jiang, DT., Crozier, ED., Gordon, RA. *J Synchrotron Radiat*. **1999**, 6, 347–349.

[5] Beamline Map. http://tpsbl.nsrrc.org.tw/index.aspx?lang=en (accessed by June 7th. 2022)

[6] 44A Quick-scanning X-ray Absorption Spectroscopy. http://tpsbl.nsrrc.org.tw/bd_page.aspx?lang=en&pid=1065&port=44A(accessed by June 25th. 2022)

[7] 44A Quick-scanning X-ray Absorption Spectroscopy. http://tpsbl.nsrrc.org.tw/bd_page.aspx?lang=en&pid=1078&port=44A (accessed by June 25th. 2022)

[8] Shi, W., Song, S., Zhang, H. *Chem. Soc. Rev*. **2013**, 42, 5714–5743.

[9] Feng, S., Xu, R. *Acc. Chem. Res*. **2001**, 34, 239–247.

[10] Cundy, CS, Cox, PA. *Chem. Rev*. **2003**, 103, 663–702.

[11] Yang Y, Zhao Q, Feng W, Li F. *Chem. Rev*. 2013;113(1):192–270. doi:10.1021/cr2004103

[12] Hirano, M. *J. Mater. Chem*. **2000**, 10, 469–472.

[13] Luan, T., Liu, J., Yuan, X., Li, J-G. *Nanoscale Res. Lett*. **2017**, 12, 1–219.

[14] Liu, J-L., Zhao, X., Chen, L-J., Pan, L-M., Yan X-P. *Anal. Chem*. **2021**, 93, 7348–7354.

[15] Srivastava, BB., Gupta, SK., Mohan, S., Mao, Y. *Chem. Eur. J*. **2021**, 27, 11398–11405.

[16] Hussen, MK., Dejene, FB. *J. Sol-Gel Sci. Technol*. **2018**, 88, 454–464. doi:10.1007/s10971-018-4830-8

[17] Aneesh, P. M., Krishna, K. M., Jayaraj, M. K., *J. Electrochem. Soc*. **2009**, K33–K36.

[18] Ewart, P. X-rays: transitions involving inner-shell electrons. *Atomic Physics*; Morgan & Claypool Publisher: San Rafael, 2019, p.58-59.

[19] Bunker, G. *Introduction to XAFS: a practical guide to X-ray absorption fine structure spectroscopy*. Cambridge University Press, 2010, p.8-35.

[20] Shikano, M., Kobayashi, H., Koike, S., Sakaebe, H., Saito, Y., Hori, H., Kageyama, H., Tatsumi, K. J. *Power Sources*. **2011**, 196, 6881–6883.

[21] Piao, Y., Qin, Y., Ren, Y., Heald, SM., Sun, C., Zhou, D., Polzin, BJ., Trask, SE., Amine, K., Wei, Y., et al. *Phys. Chem. Chem. Phys*. **2014**, 16, 3254–3260.

[22] Li, J., Liu, C-H., Li, X., Wang, Z-Q., Shao, Y-C., Wang, S-D., Sun, X-L., Pong, W-F., Guo, J-H., Sham, T-K. *Chem. Mater*. **2016**, 28, 4467–4475.

[23] Roy1, M., Gurman, SJ., van Dorssen, G. *J. Phys. IV France*. **1997**, 7, C2-151-C2-152.

[24] Suwanpinij, P., Worabut, A., Supruangnet, R., Henning Dickert, H. *AIMS Mater. Sci*. **2017**, 4, 856–866.

[25] Ramalingam, M., Ramakrishna, S. *Nanofiber composites for biomedical applications*. Ramalingam, M., Ramakrishna, S., editors. Duxford, United Kingdom: Woodhead Publishing, an imprint of Elsevier, 2017, p.97-115.

[26] Wang GC. *The utilization of slag in civil infrastructure construction*. Duxford, UK: Woodhead Publishing is an imprint of Elsevier, 2016, p.87-113.

[27] Kaliva, M., Vamvakaki, M. *Nanomaterials characterization*. Polymer Science and Nanotechnology. R. Narain, Ed.; Elsevier: Amsterdam, 2020, p.401-433

[28] Suryanarayana, C., Norton, MG. *X-Ray diffraction: a practical approach*. New York: Plenum Press,1998.

[29] Aoki, T. Photoluminescence. *Optical Properties of Materials and Their Applications*. Chichester, UK: John Wiley & Sons Ltd, 2019. p. 157–202.

[30] Griffiths PR, De Haseth JA. Introduction to Vibrational Spectroscopy. *Fourier transform infrared spectrometry*. 2nd ed. Hoboken, N.J: Wiley-Interscience, 2007, p. 1-18.

Chapter 3

3 Investigating the Influence of Synthesis Temperature on the Electronic Structure and Luminescence of Cr-doped $ZnGa_2O_4$

In this chapter, a study on the influence of synthesis temperature on the structure and luminescence property of Cr-ZGO is presented. The EDX, XRD, PL, XANES and EXAFS of Cr-ZGO synthesized under different temperatures will be discussed.

3.1 Introduction

Temperature is a crucial factor during materials synthesis. A temperature change could alter the reaction kinetics and chemical equilibrium and influences the size, shape and sometimes the crystal structure of the material, which will further impact the physical properties of materials.[1] Materials with the same chemical composition could have a different atomic arrangement, so a modification on the synthesis temperature could lead to the formation of a different crystal structure.[1] Particles can transform into a new structure when the synthesis temperature changes. There has been some research about how synthesis temperature will affect the structure. For example, a mixture of γ-MnO_2 and R–MnO_2 can be formed when the hydrothermal temperature is less 145 ℃; however, when the hydrothermal temperature increases to higher than 165 ℃ with using the same precursors (1:1 mole ratio of ammonium persulfate ($(NH_4)_2S_2O_8$) and manganese sulfate monohydrate ($MnSO_4 \cdot H_2O$)), a single pyrolusite phase β-MnO_2 is observed.[2] Undoped $ZnGa_2O_4$ can be synthesized under different hydrothermal temperatures from 150 ℃ to 240℃, and it was found that a high synthesis temperature leads to the formation of larger crystals.[3] In another study on Mn^{2+} doped Zn_2SiO_4 synthesized at different temperatures shows both the temperature influences both the luminescence intensity and emission wavelength of the material, the luminescence intensities of samples under 450 ℃ and 500 ℃ are five times weaker than the one from sample synthesized under 400 ℃.[4] In terms of Cr-doped $ZnGa_2O_4$ (Cr-ZGO), there have been many successful syntheses using the

hydrothermal method. However, the reported reaction temperatures at which the experiment was conducted vary significantly, from as low as 120 ℃ to 220 ℃ being the highest temperature reported.[5-10] To the best of my knowledge, there has been no study on how the temperature influences the structure and optical properties of the Cr-ZGO.

Therefore, in this chapter, Cr-ZGO particles were synthesized at three different temperatures, which are (1) the lowest temperature reported (120 ℃), (2) the highest temperature reported (220 ℃), and (3) an intermediate temperature (170 ℃). The observed luminescence intensity change can be correlated with the electronic structure of the materials, so as to reveal how the synthesis temperature influences the luminescence properties of Cr-ZGO.

3.2 Experimental

3.2.1 Chemicals and instrumentation

Gallium(III) nitrate hydrate ($Ga(NO_3)_3 \cdot xH_2O$, crystalline, 99.9% trace metals basis), zinc nitrate hexahydrate ($Zn(NO_3)_2 \cdot 6H_2O$, reagent grade, 98%), and ammonium hydroxide solution (NH_4OH, 28 wt%) were commercially obtained from Sigma Aldrich. Chromium (III) nitrate nonahydrate ($Cr(NO_3)_3 \cdot 9H_2O$, 98.5%) and hydrochloric acid solution (HCl, 36.5-38.0%) were commercially obtained from Alfa Aesar. All the chemicals were used without any purification.

Elemental compositions of the materials were analyzed using the energy dispersive X-ray spectroscopy (EDX). The energy of the electron beam for EDX analysis is 20 kV. The X-ray diffraction (XRD) was obtained using an Inel XRG3000 generator, and an Inel CPS 120 detector, with a Cu Kα sealed tube source. The photoluminescence (PL) spectra were collected by Fluorolog spectrometer (QM-7/2005, Photon Technology Internation (PTI)). The X-ray absorption fine structure (XAFS) spectra were collected at Taiwan Photon Source (TPS), beamline 44A, and Advanced Photon Source (APS), beamline 20BM. The spectra were processed and analyzed by Athena and Artemis from Demeter software package.[11]

3.2.2 Synthesis of Cr-ZGO

All the samples were synthesized using a hydrothermal method according to the description in Chapter 2. During the hydrothermal process, three synthesis temperatures were selected, which were 120 ℃, 170 ℃ and 220 ℃, respectively. The hydrothermal pH was set to 9 in all cases.

3.3 Results and Discussion

3.3.1 Elemental Composition Analysis

The elemental compositions of the Cr-ZGO synthesized at different temperatures were examined by EDX, and Table 3-1 summarizes the concentration of Zn and Ga in each sample. Interestingly, the 120 ℃ has a particularly low Zn concentration, so the product formed at this temperature is Zn-deficient. The Ga/Zn ratio deviates significantly from the theoretical value of 2. At higher synthesis temperatures, more Zn is able to be incorporated into the ZGO lattice, and the 220 ℃ sample has the lowest Ga/Zn ratio. It should be noted that the presence of Cr cannot be confirmed by EDX for all samples, due to its low concentration (i.e. 0.5 mol%).

Table 3- 1. The elemental concentrations of Zn and Ga in Cr-ZGO synthesized at three different temperatures, with the calculated Ga to Zn ratio.

Hydrothermal temperature	Zn %	Ga %	Ga to Zn ratio
120 ℃	6.69	19.00	2.8 ± 0.2
170 ℃	10.91	24.02	2.20 ± 0.04
220 ℃	11.02	23.29	2.1 ± 0.1

3.3.2 Crystal Structure Analysis

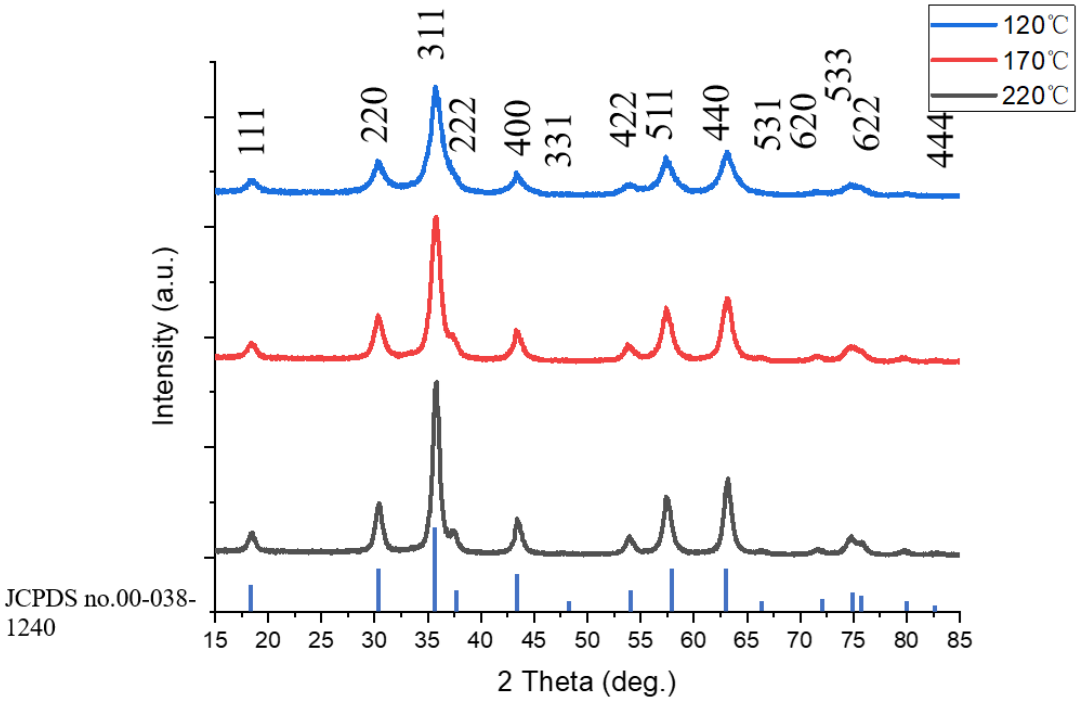

Figure 3- 1. XRD patterns of Cr-ZGO synthesized at different temperatures.

The crystal structures of the three Cr-ZGO synthesized at different temperatures are examined by XRD. In Figure 3-1, all three samples show the existence of the $ZnGa_2O_4$ structure. By comparing with JCPDS no.00-038-1240,[12,13] all peaks are indexed. Although EDX has shown the Ga to Zn ratio is higher than the stoichiometric value, in XRD, there is no unidentified peak which suggests there are no other crystalline species formed in these samples. It is noticed that with the increase of temperature, the peak becomes narrower. This means a high degree of crystallinity. The crystalline sizes of the three samples are calculated using the Scherrer equation (Equation 3-1) based on the (3 1 1) diffraction peak.

$$D = \frac{0.9\,\lambda}{B\cos\theta} \qquad \textbf{(Equation 3-1)}$$

where D is the crystalline size in Angstroms; λ is the wavelength of incident X-ray in Angstroms; B is angular full width at half maximum of the diffraction peak; θ is Bragg

angle. The result is summarized in Table 3-2. The crystalline size of Cr-ZGO increases with increasing of the synthesis temperature.

Table 3- 2. The crystalline sizes of Cr-ZGO synthesized at different temperatures.

Hydrothermal temperature	120 ℃	170 ℃	220 ℃
Crystalline size (nm)	8.059	9.574	13.331

3.3.3 Optical Property Characterization

All Cr-ZGO samples emit red light when exposed to the UV light of 365 nm, shown in Figure 3-2. By visually examining the luminescence intensity, the ones synthesized at 170 ℃ and 220 ℃ show relatively stronger luminescence. PL measurements were conducted to obtain the luminescence spectra. It should be noted that in this chapter, when comparing the luminescence intensity variation of one sample under different excitation wavelengths, such intensity is referred to as relative intensity. When comparing luminescence from different samples under the same excitation wavelength, the intensity is referred to as overall intensity.

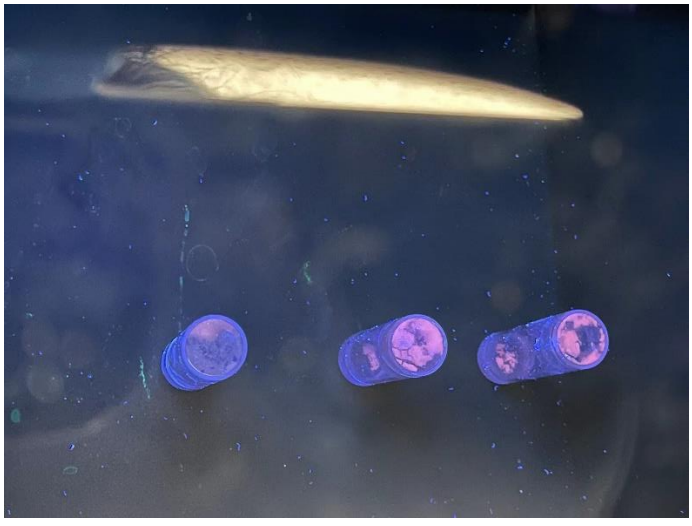

Figure 3- 2. A photograph of Cr-ZGO excited under the 365 nm UV light. From left to right: Samples synthesized at 120 ℃, 170 ℃ and 220 ℃.

The PL excitation spectra were obtained by monitoring the 695 nm emission. As shown in Figure 3-3, there are three excitation wavelengths where the emission intensities are enhanced, especially in samples 170 ℃ and 220 ℃. These three excitation peaks are at around 280 nm, 415 nm, and 555 nm, respectively. The UV excitation band at 280 nm can be ascribed to the host absorption, indicating an energy transfer (ET) from the host to Cr^{3+}. This process can be bridged by the host defect. Excitation peaks around 280 nm, 415 nm and 555 nm excitations are due to $^4A_2$ (^4F) → $^4T_1$ (^4P), $^4A_2$ (^4F) → $^4T_1$ (^4F) and $^4A_2$ (^4F) →$^4T_2$ (^4F) transitions of Cr^{3+} respectively.[14-16]

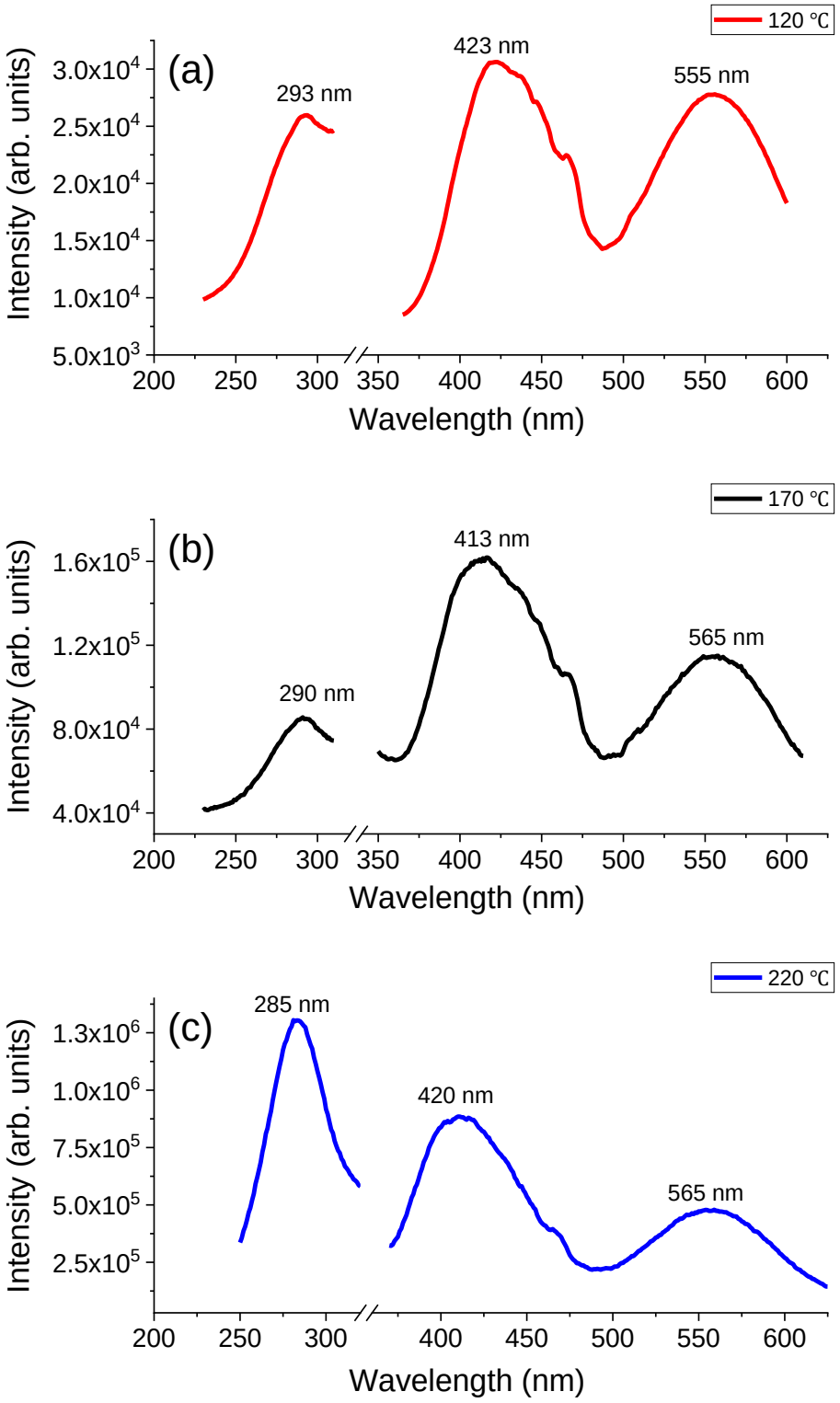

Figure 3- 3. PL excitation spectra of Cr-ZGO samples synthesized temperature at (a) 120 ℃, (b) 170 ℃ and (c) 220 ℃.

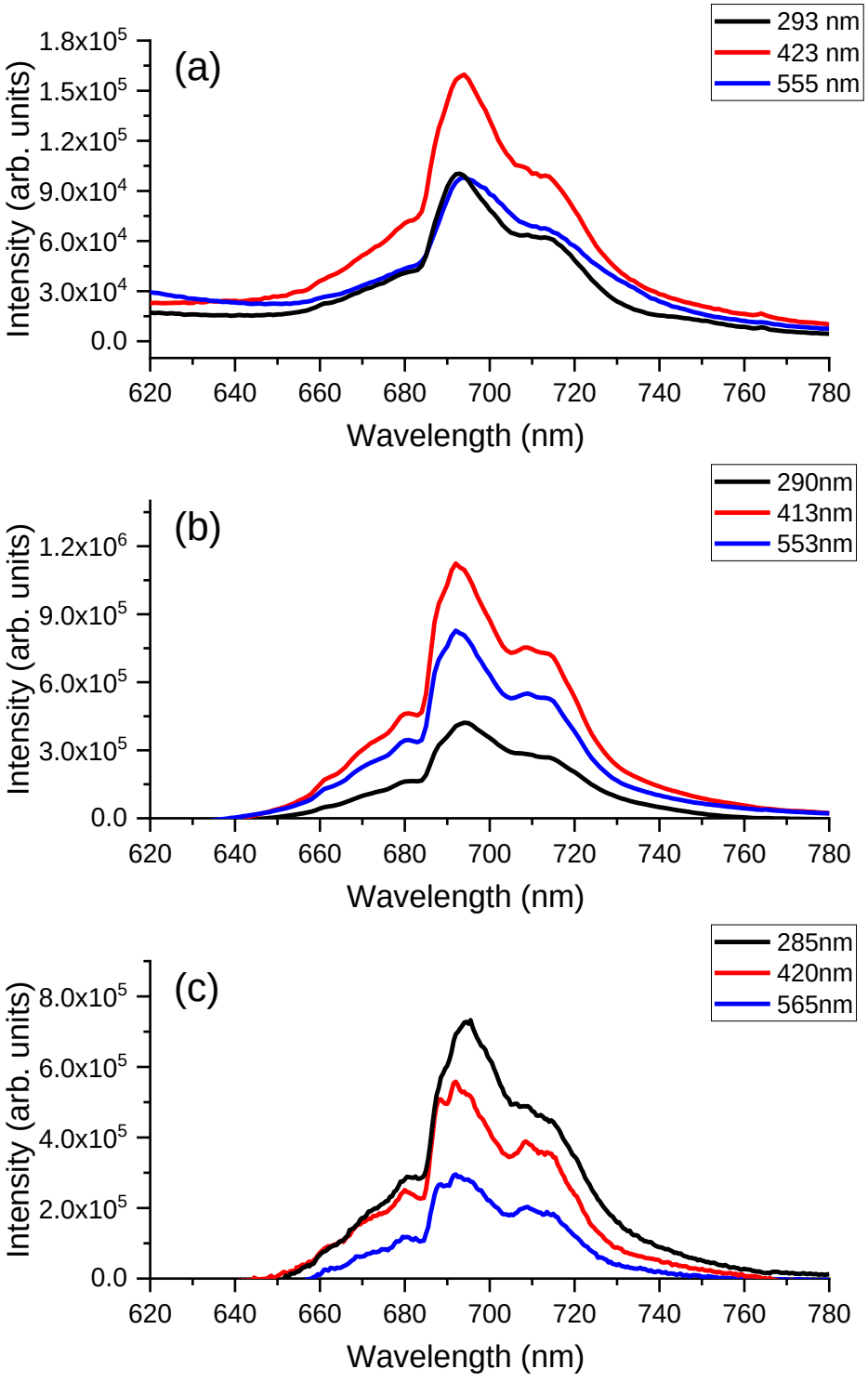

Figure 3- 4. PL emission spectra of Cr-ZGO samples synthesized at (a) 120 ℃, (b) 170 ℃, and (c) 220 ℃.

According to wavelengths obtained from excitation scans, the emission scans were taken using the wavelength at the three excitation maxima for each sample, and the spectra are shown in Figure 3-4. All the samples show red/NIR emission peaks at around 700 nm. The main emission band is the d-d transition of Cr^{3+} ions (^2E (^2G) state to $^4A_2$ (^4F) state) inside the spinel host lattice.[17] The peak at around 695 nm is the characteristic of the N2 band, which is related to the anti-site defects adjacent to Cr^{3+} ions .[18, 19] The shoulder next to the N2 band at ~688 nm is the zero phonon R line, which is caused by weak trigonal distortion around Cr^{3+} in the unperturbed octahedral sites.[14, 18, 20] The R line is accompanied by Stokes phonon side band (PSB) at longer wavelengths (708-715 nm), and the anti-Stokes PSB at shorter wavelengths (660 nm-680 nm), respectively.[17, 20, 21]

From Figure 3-4, we can see that the PL intensity within each sample depends on the excitation wavelength, but such dependency is not the same. For example, the 220 ℃ sample exhibits the strongest emission at 285 nm excitation, but for the 170 ℃ and 120 ℃ samples, the strongest emission occurs when using the 415 nm excitation. Since the excitation around 285 nm is related to an energy transfer from the host to Cr^{3+}, and this process can be bridged by the host defect, the relative intensity change may be related to the host defect caused by the temperature change.[5] This may suggest that 170 ℃ and 120 ℃ samples have more host defects than 220 ℃ sample. The relative intensities caused by 415 nm and 555 nm are not affected by temperature as significantly as emission at 285 nm since they are caused by the d-d transition of Cr and are less related to host defect.

Figure 3-5 shows the overall PL intensity comparison of these three samples under the same excitation wavelength, and the results show that the PL from the 120 ℃ sample is the weakest regardless of the excitation wavelength. The 220 ℃ sample is the strongest emitter under UV excitation, while the 170 ℃ is much brighter under visible light (415 nm and 555 nm) excitation. Since the high temperature may cause large crystal size and further lead to more atoms of Cr-ZGO on surface, this may be one of the potential reasons why 220 ℃ and 170 ℃ samples have stronger emissions.

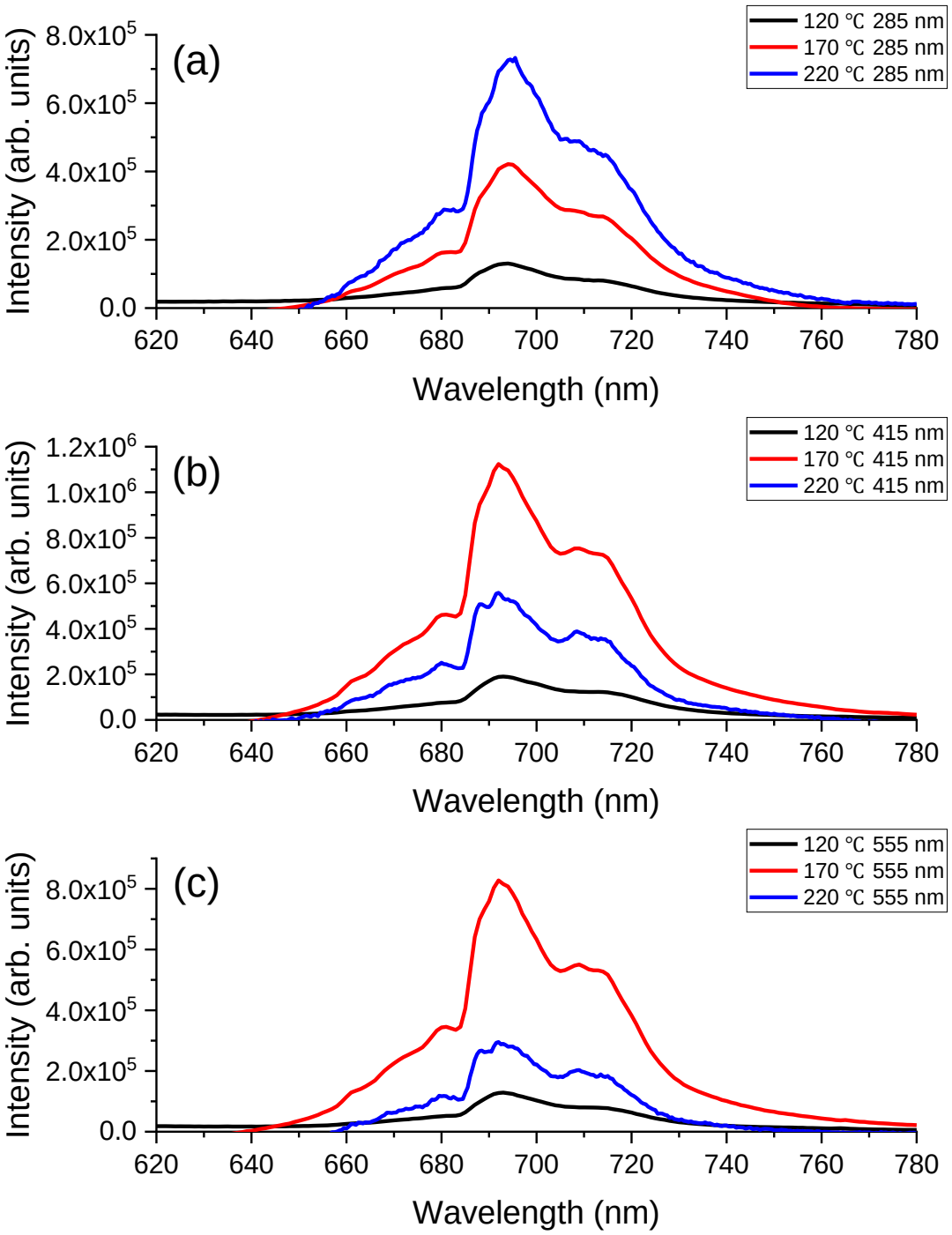

Figure 3- 5. The PL intensity comparison of three samples excited under (a) 285 nm, (b) 415 nm and (c) 555 nm

3.3.4 Electronic Structure

3.3.4.1 The Zn K-edge XAFS

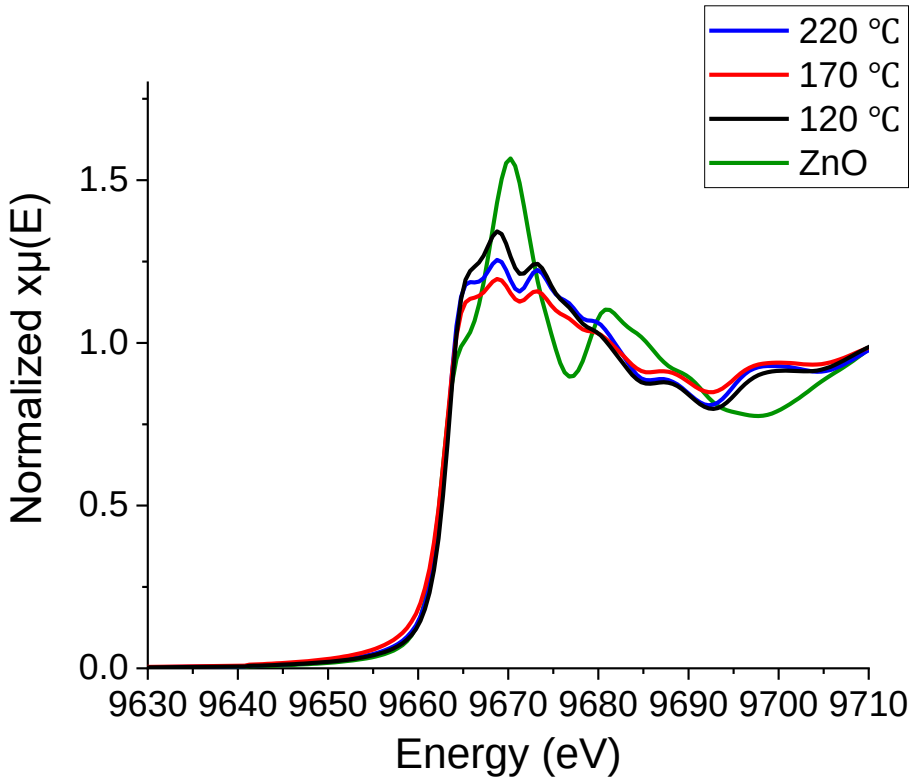

Figure 3- 6. The Zn K-edge XANES of Cr-ZGO samples synthesized at different temperatures. The spectrum of ZnO is included as a reference.

As shown in Figure 3-6, the Zn K-edge X-ray absorption near edge structure (XANES) spectra have several resonances between 9660 eV and 9668 eV, which corresponds to the Zn 1s to 4p electronic transition. In ZGO, Zn is four-coordinated with O, so the spectra of Cr-ZGO are compared with the XANES of ZnO, a hexagonal crystal in which Zn is four-coordinated with O. It can be seen that the spectral profile of Cr-ZGO is drastically different from the one of ZnO, confirming that all Zn are incorporated into the Ga-O lattice, and no ZnO phase is detected.[23, 24]

Although the Zn K-edge spectra for all Cr-ZGO are similar, there are still noticeable differences, mainly the intensity of the main resonances. The 120 ℃ sample shows the

highest intensity, followed by 220 ℃ samples, and the 170 ℃ sample has the lowest intensity. Since the absorption comes from the Zn 1s to 4p transition, the peak intensity can be related to the occupancy of Zn 4p orbital: the 170 ℃ sample has the most occupied 4p orbitals, followed by the 220 ℃ sample, and the 120 ℃ sample. The 4p occupancy can be related to the number of coordinated O atoms around Zn. Due to the hybridization between O and Zn, a higher amount of O atoms could facilitate a more efficient charge transfer, hence lowering the 4p electron density (increased absorption peak intensity).[22] This suggests Zn in the 120 ℃ sample is surrounded with most oxygens, while the 170 ℃ sample contains most oxygen vacancies. This will be further confirmed by analyzing the EXAFS region of the Zn K-edge spectra.

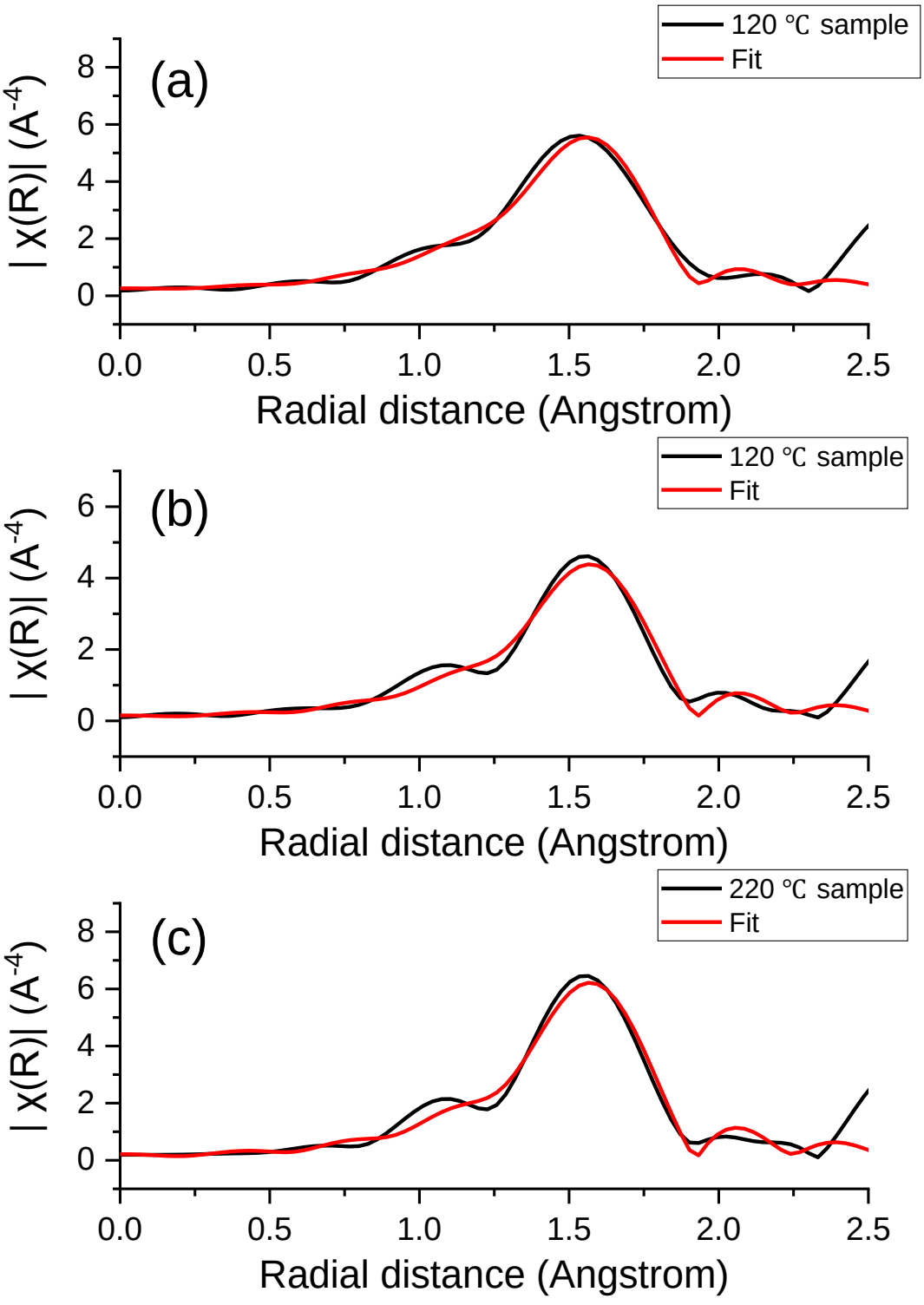

Figure 3- 7. The Zn K-edge EXAFS first-shell fit for Cr-ZGO samples plotted in R-space (a) 120 ℃ sample, (b) 170 ℃ sample, (c) 220 ℃ sample.

Table 3- 3. Detailed EXAFS fitting parameters for Cr-ZGO synthesized at different temperatures.

Hydrothermal temperature	CN	R(Å)	σ^2 (Å^2)	ΔE_0(eV)
120 ℃	3.1 ± 0.3	1.980 ± 0.009	0.007 ± 0.001	1.5 ± 1.3
170 ℃	2.0 ± 0.2	1.977 ± 0.009	0.005 ± 0.001	2.6 ± 1.2
220 ℃	2.5 ± 0.2	1.973 ± 0.009	0.004 ± 0.001	2.6 ± 1.2

Notes: CN, coordination number; R(Å), interatomic distance. σ^2 (Å^2), the Debye-Waller factor (mean square relative displacement); ΔE_0 (eV), the difference between experimentally determined threshold energy and the FEFF calculated threshold energy.

The EXAFS region of the Zn K-edge was analyzed by performing a first-shell fit to the spectra, using a Zn-O single scattering path from a model ZGO compound.[25] Figure 3-7 shows the fitted spectra plotted in R-space. The detailed fitting parameters are summarized in Table 3-3. It can be noticed that with the temperature increase, σ^2 (mean square relative displacement) decreases, suggesting the structure formed is less disordered, which agrees with the results obtained from XRD. The Zn-O bond length also decreases when the synthesis temperature increases, suggesting a more compact crystal is formed. We then look at the coordination number (CN) of the Zn-O bond. In an ideal ZGO crystal, Zn is surrounded by four O, so CN equals 4. However, the EXAFS fit reveals Zn in all samples are undercoordinated. For the 170 ℃ sample, there are the most oxygen vacancies around Zn (the lowest CN of Zn-O). Recall the PL of 170 ℃ sample (Figure 3-4b), it has the lowest relative emission intensity when excited at 290 nm, therefore excess oxygen vacancies lead to a decreased intensity under UV excitation. Luminescence generated under UV excitation is mostly facilitated by energy transfer (ET) from the host to Cr^{3+}. A large amount of oxygen vacancies could act as electron traps, hindering an efficient transfer to Cr^{3+}. The

luminescence under visible light excitation, however, is not affected by this process, therefore the 170 ℃ sample produces higher PL under 413 nm and 553 nm excitation.

3.3.4.2 The Ga K-edge XAFS

Figure 3-8 shows the Ga K-edge XANES spectra of the three samples, in comparison with the spectrum of Ga_2O_3. All spectra contain one main resonance located between 10364 eV and 10380 eV, but unlike the Zn K-edge XANES, the differences in the Ga K-edge XANES are more apparent. It can be seen that the 220 ℃ sample shows the highest intensity that is comparable to Ga_2O_3, while the 120 ℃ sample is the lowest. The position of peak maxima of 170 ℃ and 120 ℃ samples are similar, but the 220 ℃ sample appears at an energy 1.91 eV higher. The Ga XANES suggest that 120 ℃ sample shows the most occupied 4p orbital. This means Ga in 120 ℃ samples has the least O surrounded. Meanwhile, the 220 ℃ shows the least occupied 4p orbital. This means Ga in 120 ℃ samples has most O surrounded.

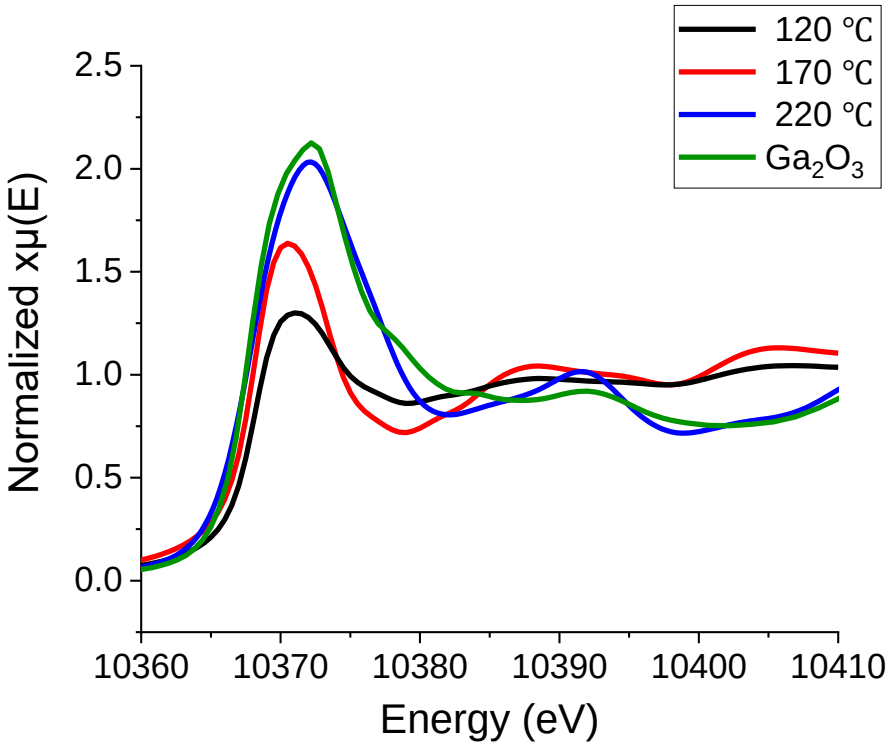

Figure 3- 8. The Ga K-edge XANES of Cr-ZGO synthesized at different temperatures.

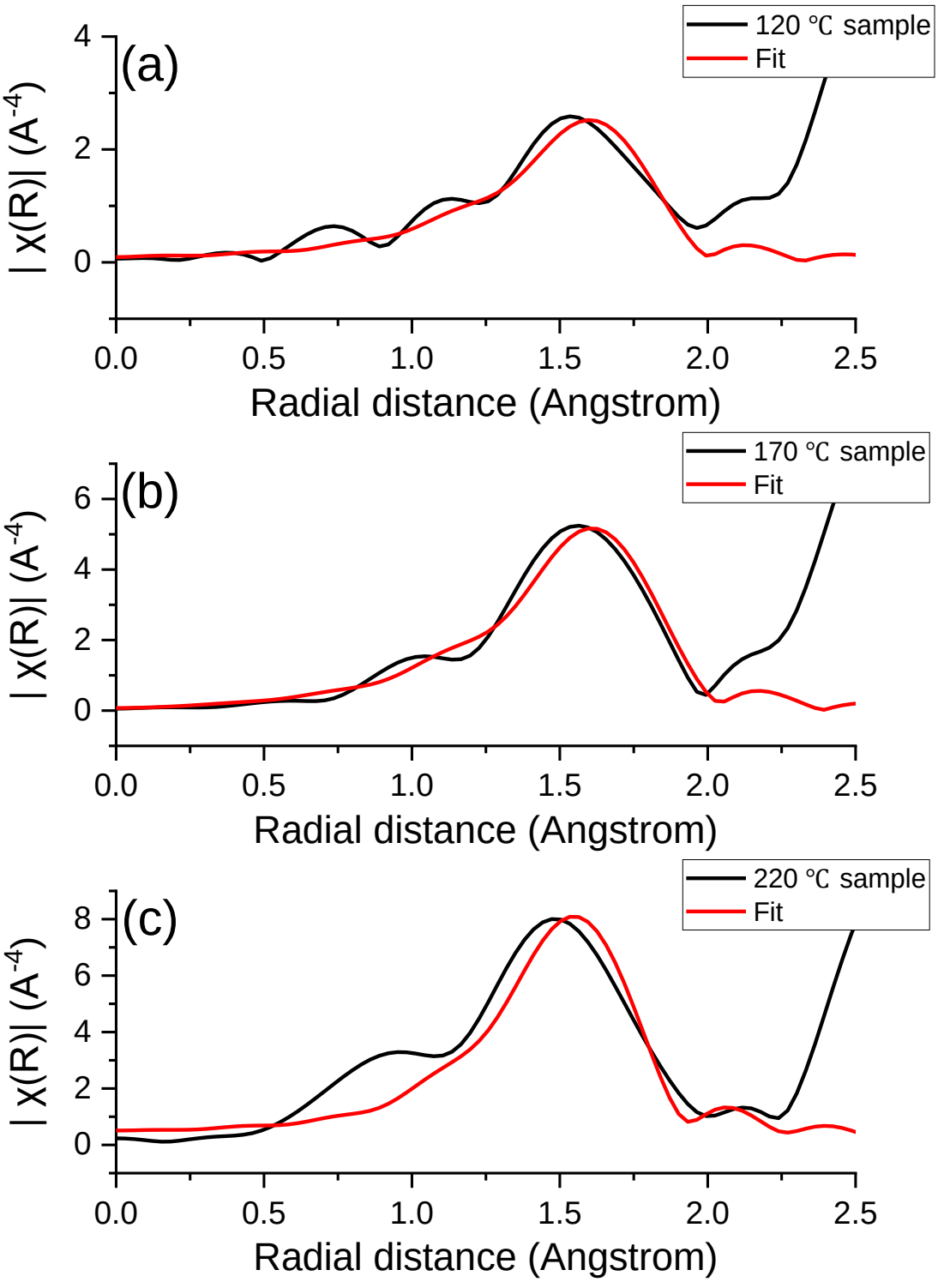

Figure 3- 9. The Ga K-edge EXAFS first-shell fitting of Cr-ZGO plotted in R-space. (a) the 120 ℃ sample, (b) the 170 ℃ sample, (c) the 220 ℃ sample.

Table 3- 4. The fitting results with structure information for Cr-ZGO synthesized at different temperatures.

Hydrothermal temperature	CN	R(Å)	σ^2 (Å^2)	ΔE_0(eV)
120 ℃	1.9 ± 0.4	2.09 ± 0.02	0.007 ± 0.003	-8.7 ± 2.4
170 ℃	4.1 ± 0.7	2.11 ± 0.02	0.007 ± 0.003	-8.1 ± 2.1
220 ℃	4.1 ± 0.7	1.98 ± 0.02	0.008 ± 0.003	7.0 ± 1.5

Notes: CN, coordination number; R(Å), interatomic distance. σ^2 (Å^2), the Debye-Waller factor (mean square relative displacement); ΔE_0 (eV), the difference between experimentally determined threshold energy and the FEFF calculated threshold energy.

The first-shell EXAFS fitting was also performed at the Ga K-edge. The fitted spectra plotted in R-space are shown in Figure 3-9, and the fitting parameters are summarized in Table 3-4. The temperature increase from 120 ℃ to 170 ℃ does not significantly affect the disorder of oxygen nearby Ga since all samples have similar σ^2 values. Similar to Zn, the Ga-O bond length also shortens when the synthesis is conducted at a high temperature.

The most noticeable difference among the three samples is still the CN. The Ga in the 120 ℃ sample has an extremely low CN comparing with the other two samples, while the CN of Ga-O for the other two samples are comparable. Recall the PL results, the 120 ℃ has the lowest PL intensity regardless of excitation energy, so it could be linked to the presence of excess oxygen vacancies around Ga. Therefore, it can be concluded the oxygen vacancy defects around Ga and Zn have different roles in modulating the luminescence properties of Cr-ZGO: more oxygen vacancies around Ga will decrease the overall PL intensity, while the oxygen vacancies around Zn have less impact on the overall PL intensity, but it determines which excitation wavelength produces the highest PL. This is probably because

that the oxygen vacancies around Ga will capture the charge carriers stronger than the oxygen vacancies around Zn.

3.3.4.3 The Cr K-edge XANES

The local structure of the Cr was examined by the Cr K-edge XANES spectra. As shown in Figure 3-10, all three Cr-ZGO exhibit similar profiles, with some minor differences. The overall spectral profile resembles Cr in an octahedral environment, [16] indicating Cr is substituting Ga in the ZGO lattice. Figure 3-10(b) focuses on the pre-edge region of the spectra, which is between 5988 eV and 5995 eV. There are two characteristic peaks labeled in Figure 3-10 (b) as P-A and P-B. These two peaks are caused by electronic transitions of Cr 1s electron to t_{2g} and $e_{g,}$ respectively.[21] The 120 ℃ sample shows a 0.5 eV energy shift to lower energy for peak P-A and 0.5 eV energy shift to higher energy for peak P-B comparing with 170 ℃ and 220 ℃ samples. These two shifts show the charge redistributions happened between t_2g and e_g. This suggests that 120 ℃ sample t_{2g} is more occupied but e_g is less occupied comparing with 170 ℃ and 220 ℃ samples. This difference is caused by the different amounts of oxygen vacancies among the three samples. The geometries (Td, C3v and Oh) of Cr will show a variation of the pre-edge. By comparing with Farges's study, the pre-edge in Figure 3-10 shows regular Cr^{3+} octahedral geometry.[26] This is evidence that Cr^{3+} ions replace the position of Ga in ZGO, there is no significant oxidation state change.

The 170 ℃ sample shows the most intense peak at pre-edge (relative empty 3d orbitals), and 120 ℃ sample is slightly higher than and 220 ℃ sample, which means 3d orbitals of 120 ℃ sample is less occupied than 220 ℃ sample. As previously mentioned, Cr^{3+} ions replace the position of Ga in ZGO. The Cr-O coordination environment therefore resembles of the one of Ga-O. In both Cr K-edge XANES and Ga K-edge XANES, 220 ℃ sample shows the strongest intensity, and 120 ℃ sample shows the weakest intensity. The intensity variation at different synthesis temperatures observed in the Cr K-edge XANES is in good agreement with the one observed for the Ga K-edge XANES.

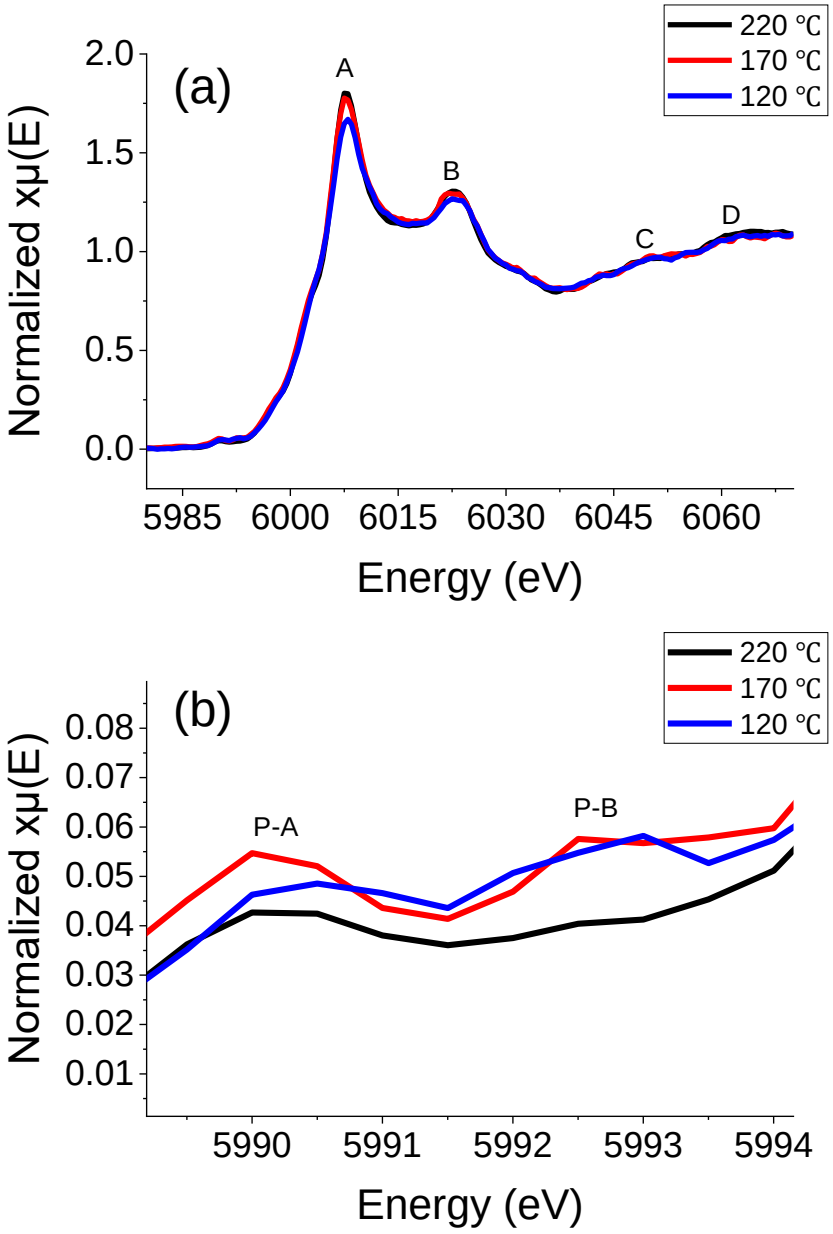

Figure 3- 10. Cr K-edge XANES of Cr-ZGO synthesized at different temperatures (a) The overview of Cr K-edge XANES of Cr-ZGO synthesized at different temperatures. (b) a magnified view at the pre-edge of the Cr K-edge XANES.

3.4 Conclusion

The influence of hydrothermal synthesis temperature on the structure and luminescence of Cr-ZGO particles was investigated. All temperatures lead to the formation of pure-phase ZGO, but the crystalline size increases in the samples synthesized at a higher temperature. All samples exhibit characteristic Cr^{3+} emission at 700 nm; however, the intensity varies significantly. Among the three excitation bands (290 nm, 415 nm and 555 nm), the 120°C sample exhibits the lowest emission intensity. The 170°C sample emits strongly when excited at 415 nm and 555 nm, while the 220°C sample has the most intense luminescence only when it is excited at 290 nm. This difference is due to the energy transfer from the host to Cr^{3+}. The electronic structure-luminescence correlation was further investigated by XAFS at the Zn, Ga, and Cr K-edge, respectively. The Cr^{3+} replaces the Ga octahedral site in all samples. The main influence of the temperature is the number of oxygen vacancies. The 170°C sample with the strongest emissions caused by the visible lights shows the most oxygen vacancies around Zn, and 120 °C sample with the weakest emissions shows the most oxygen vacancies around Ga. Oxygen vacancies around Zn and Ga affect the intensity of luminescence. This is because that the oxygen vacancies around Ga will capture the charge carriers stronger than the oxygen vacancies around Zn. Oxygen vacancies tend to form around Ga at lower synthesis temperatures, which leads to an overall low PL intensity. A high temperature could lead to a better coordinated Ga-O environment but brings in more oxygen vacancies around Zn. A higher amount of oxygen vacancies around Zn, increases the overall luminescence.

3.5 References

[1] Sau TK, Rogach AL. Complex-shaped metal nanoparticles: bottom-up syntheses and applications. Weinheim: Wiley-VCH; 2012.

[2] Zeng, L., Zhang, G., Huang, X., Wang, H., Zhou, T., Xie, H. *Vacuum*. **2021**, 192, 110398.

[3] Hirano, M. *J. Mater. Chem*. **2000**, 10, 469–472.

[4] Shibuki, K., Takesue, M., Aida, TM., Watanabe, M., Hayashi, H., Smith, RL. *J. Supercrit. Fluids*. **2010**, 54, 266–271.

[5] Li, Z., Zhang, Y., Wu, X., Huang, L., Li, D., Fan, W., Han, G. *J. Am. Chem. Soc*. **2015**,137, 5304–5307.

[6] Maldiney, T., Bessière, A., Seguin, J., Teston, E., Sharma, SK., Viana, B., Bos, AJJ., Dorenbos, P., Bessodes, M., Gourier, D., et al. *Nat. Mater*. **2014**, 13, 418–426.

[7] Wang, Y., Yang, C-X., Yan, X-P. *Nanoscale*. **2017**, 9, 9049–9055.

[8] Wang, H-F., Chen, X., Feng, F., Ji, X., Zhang, Y. *Chem. Sci*. **2018**, 9, 8923–8929.

[9] Mondal, A., Manam., J. *Mater. Res. Express*. **2019**, 6, 95081.

[10] Tuerdi, A., Abdukayum., A. *RSC Adv*. **2019**, 9, 17653–17657.

[11] Ravel, B., Newville, M. *J Synchrotron Radiat*. **2005,** 12, 537–541.

[12] Sun, M., Li, D., Zhang, W., Chen, Z., Huang, H., Li, W., He, Y., Fu, X. *J. Solid State Chem.* **2012**, 190, 135–142.

[13] Basavaraju, N., Priolkar, KR., Gourier, D., Bessière, A., Viana, B. *Phys. Chem. Chem. Phys.* **2015**, 17, 1993–1999.

[14] Zhou, Z., Zheng, W., Kong, J., Liu, Y., Huang, P., Zhou, S., Chen, Z., Shi, J., Chen, X. *Nanoscale*. **2017**, 9, 6846–6853.

[15] Lakshmi Reddy, S., *Electronic (Absorption) Spectra of 3d Transition Metal Complexes*. IntechOpen; 2012.

[16] Mian, F., Bottaro, G., Wang, Z., You, Y-M., Rancan, M., Sham, T-K., Armelao, L. *Appl. Surf. Sci.* **2022**, 577, 151896.

[17] Bessière, A., Jacquart, S., Priolkar, K., Lecointre, A., Viana, B., Gourier, D. *Opt. Express*. **2011**, 19, 10131-10137.

[18] Mikenda, W., Preisinger, A. *J. Lumin*. **1981**, 26, 53–66.

[19] Mikenda, W., Preisinger, A. *J. Lumin.* **1981**, 26, 67–83.

[20] Bessière, A., Sharma, SK., Basavaraju, N., Priolkar, KR., Binet, L., Viana, B., Bos, AJJ., Maldiney, T., Richard, C., Scherman, D., et al. *Chem. Mater.* **2014**, 26, 1365–1373.

[21] Srivastava, BB., Kuang, A., Mao, Y. *ChemComm (Cambridge, England)*. **2015**, 51,7372–7375.

[22] Zhang, S., Zhang, L., Li, H., Li, J., Jiang, Z., Chu, W., Huang, Y., Wang, J., Wu, Z. *J Synchrotron Radiat*. **2010**,17, 600–605.

[23] Rodrigues, A., do Carmo Martins Alves, M., Morais, J. *Mater. Des*. **2018**, 142, 240–246.

[24] Chen, M-IM-I., Singh, AKAK., Chiang, J-LJ-L., Horng, R-HR-H., Wuu, D-SD-S. *Nanomaterials (Basel)*. **2020**, 10, 2208.

[25] Allix, M., Chenu, S., Véron, E., Poumeyrol, T., Kouadri-Boudjelthia, EA., Alahraché, S., Porcher, F., Massiot, D., Fayon, F. *Chem. Mater*. **2013**, 25, 1600–1606.

[26] Farges, F. *Phys Chem Miner*. **2009**, 36, 463–481.

Chapter 4

4 Investigating the Influence of Synthesis pH Condition on the Electronic Structure and Luminescence of Cr-doped $ZnGa_2O_4$

In this chapter, a study on the influence of the synthesis pH environment on the structure and luminescence property of Cr-ZGO is presented. The EDX, XRD, PL, XANES and EXAFS of Cr-ZGO synthesized under different pH environments will be discussed. In addition, the effects of different base addition rates on the luminescence property of Cr-ZGO will be discussed.

4.1 Introduction

Hydrothermal synthesis has been a commonly used method to make various spinel nanoparticles, such as $ZnAl_2O_4$, $ZnGa_2O_4$, and $NiCo_2O_4$, and many others.[1-6] A typical synthesis procedure starts with dissolving metal precursor salts to produce hydroxy complexes. The hydroxy complexes react in the solution to form spinel nanoparticles at the microscopic level under the hydrothermal condition where the temperature is over 100 ℃ at elevated pressures. Equations 4-1 to 4-5 show the reaction mechanism of $ZnGa_2O_4$ (ZGO) formation as an example.[5] It can be seen that in order to produce the $Zn(OH)_3^-$ and $Ga(OH)_4^-$ species, a basic environment is essential. Therefore, the concentration of OH^- plays a significant role in the reaction kinetics. NH_4OH is the commonly used base to adjust the pH environment for ZGO synthesis.[6-11] It was found that with the increase of pH, the particle size increases with higher crystallinity.[12] When it comes to Cr-doped ZGO, however, although similar outcomes might be expected due to the similarity between ZGO and Cr-ZGO, there has been no study performed on how the pH environment impacts the crystal structure, and in particular, the luminescence property of Cr-ZGO.

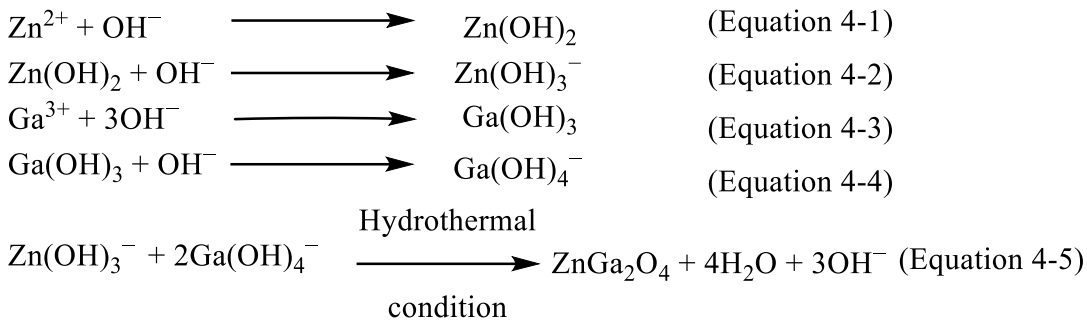

In this chapter, Cr-ZGO nanoparticles were synthesized under different pH environments, from neutral (pH=7) to strongly basic (pH=11). The structure and the luminescence of the as-formed nanoparticles are comparatively studied. In addition, we have noticed some literature emphasizes in the experimental procedure that the NH_4OH shall be added quickly.[6] Therefore we also investigate whether how fast the NH_4OH is added impacts the luminescence of Cr-ZGO. X-ray diffraction, photoluminescence (PL) spectroscopy, and X-ray absorption fine structure (XAFS) were utilized to characterize various Cr-ZGO products.

4.2 Experimental

4.2.1 Synthesis of Cr-ZGO under Different pH Environments

All the chemicals and instrumentation have been introduced in chapter 3. There is no difference for the chemicals and instrumentation in this chapter. All the samples were synthesized using a hydrothermal method according to the description in Chapter 2. During the hydrothermal process, three synthesis pH conditions were selected, which were pH=7, pH=9 and pH=11, respectively. The hydrothermal temperature was set to 220 ℃ in all cases.

4.2.2 Synthesis of Cr-ZGO with different base addition rates

Three samples were prepared following the same hydrothermal protocol as described in the previous section, with pH set to be 9, but the pH adjustment was performed by adding

NH_4OH at different rates. For sample 1, NH_4OH was added at 1-2 drops per second until the pH is 9, and the volume used is recorded. The whole process took about 15 minutes. For sample 2, the same volume of NH_4OH was added at 3-4 drops per second until the pH is 9. The whole process took about 8 minutes. For sample 3, an equal volume of NH_4OH was added at once (i.e. rapid addition).

4.3 Results and Discussion

4.3.1 Elemental Composition Analysis

The elemental compositions of Cr-ZGO prepared under different pH environments were analyzed by EDX (Table 4-1). This is noticed that with the increase of pH, the Ga/Zn ratio increases. The difference between pH=7 and pH=9 samples is not as significant as the one between pH=9 and pH=11 samples. This suggests when pH is below or equal to 9, the pH change does not affect elemental composition a lot. However, a more basic environment produces a Ga-rich Cr-ZGO. As Chapter 3 has mentioned, Ga to Zn ratio is larger than the theoretical 2:1 value because some structure defects lead to that some of Zn are missing with vacancies, or the Ga takes over the Zn positions. The EDX result suggests Cr-ZGO formed in a strongly basic environment deviates from the theoretical structure. The Zn ions are not effectively incorporated into the ZGO system under a strongly basic environment.

Table 4- 1. Elemental concentration of Cr-ZGO synthesized under different pH conditions.

pH value	Zn %	Ga %	Ga to Zn ratio
pH=7	8.85	18.66	2.11 ± 0.01
pH=9	11.02	23.29	2.11 ± 0.04
pH=11	10.34	26.39	2.55 ± 0.04

4.3.2 Crystal Structure Analysis

Figure 4-1 shows the XRD for the Cr-ZGO samples prepared under pH=7, 9, and 11, respectively. The results are compared with the literature to confirm the identity of Cr-ZGO.[13,14] The results confirm the existence of $ZnGa_2O_4$ particles in all cases. No unidentified impurities peaks are present. It is noticed that a low pH value will lead to a broad peak which indicates a poor degree of crystallinity. Table 4-2 shows the calculated crystalline size, using the Scherrer equation based on the (3 1 1) diffraction peak. The high pH condition facilitates the formation of larger crystals.

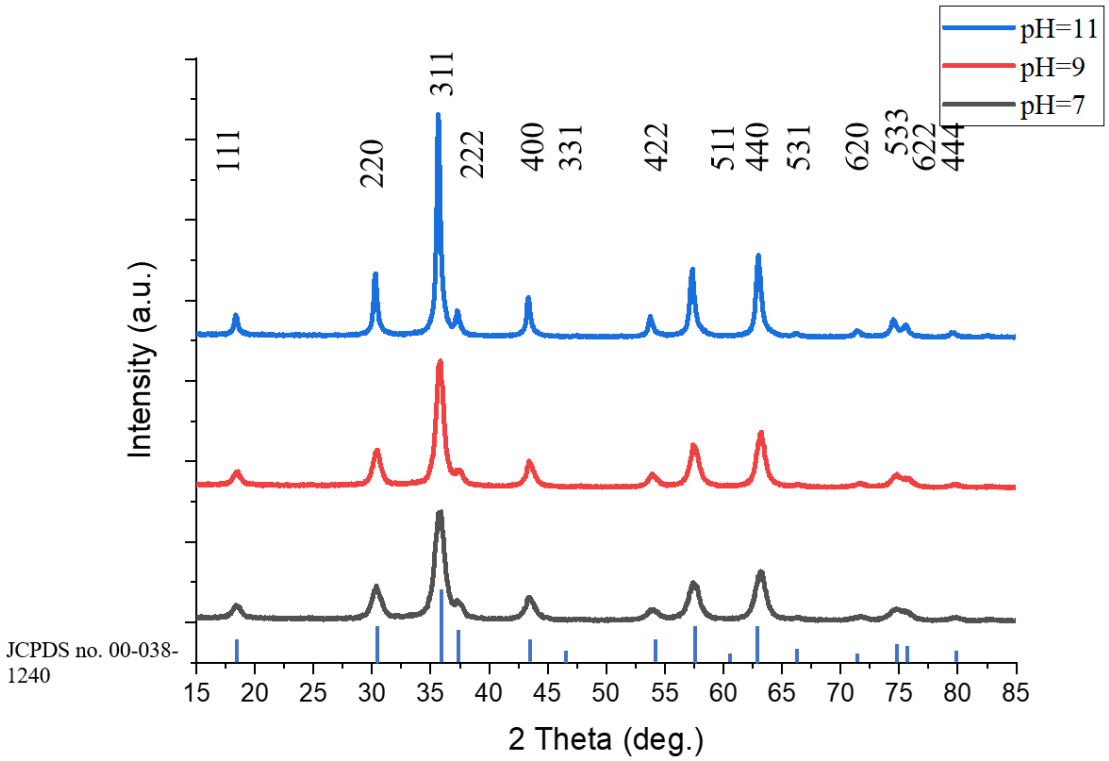

Figure 4- 1. XRD patterns of Cr-ZGO prepared under different pH environments.

The effect of NH_4OH addition rate on the crystallinity of the Cr-ZGO was also investigated. The target pH was set to be 9. Interestingly, when NH_4OH is added more abruptly, the Cr-ZGO has better crystallinity, demonstrated by narrower diffraction peaks in Figure 4-2, as well as the calculated crystalline size in Table 4-2. The possible reason is that the speed of base addition will affect the intermediate steps (Equations 4-1 to 4-4). The fast addition rate may lead that the intermediate step reactions are inadequate. This may lead to hydroxy

complexes precipitates accumulating in a short time; therefore, this accumulation will cause a larger crystal size.

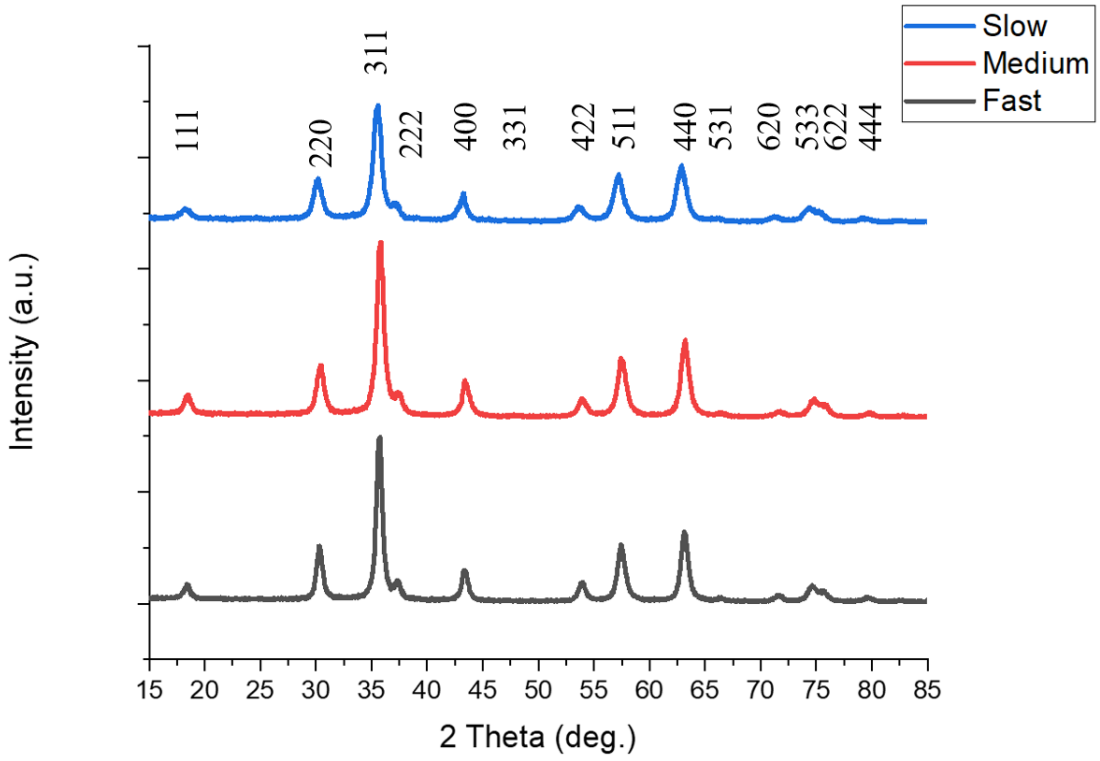

Figure 4- 2. X-ray diffraction patterns of Cr-ZGO prepared under different base addition rates.

Table 4- 2. The crystal sizes of Cr-ZGO prepared under different pH environments and different base addition rates.

pH value	7	9	11	9	9	9
Base addition rates	Medium	Medium	Medium	Slow	Medium	Fast
Crystal size (nm)	9.899	13.331	25.490	11.331	13.331	14.589

4.3.3 Optical Property Characterization

4.3.3.1 Cr-ZGO Synthesized under Different pH Environments

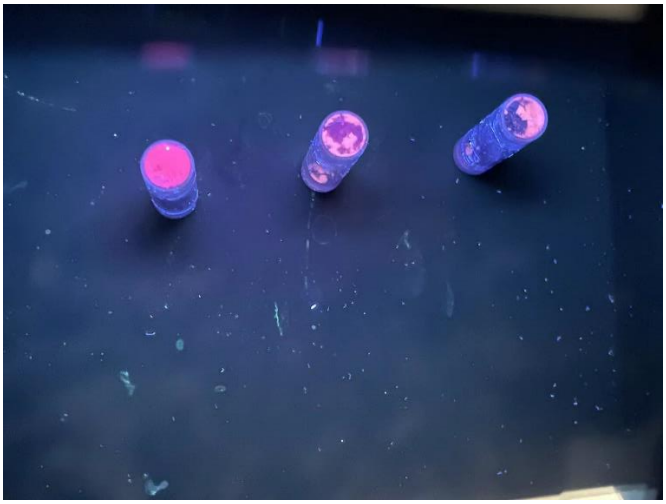

Figure 4- 3. Cr-ZGO samples synthesized under different pH environments exposed to 365 nm UV light. From left to right: pH=7, pH=9 and pH=11.

Figure 4-3 shows the photograph of the Cr-ZGO synthesized under different pH environments exposed to 365 nm UV light. Visually, pH=7 sample shows the brightest luminescence. pH=9 sample is brighter than pH=11 sample. For the quantitative study, the excitation scans of samples under pH=7, 9 and 11 monitored at 695 nm are shown in Figure 4-4. All samples exhibit three characteristic peaks that are related to the d-d transition of Cr^{3+} ions: the $^4A_2(^4F)$ - $^4T_1(^4P)$ (293 nm), $^4A_2(^4F)$ - $^4T_1(^4F)$ (420 nm), and $^4A_2(^4F)$ - $^4T_2(^4F)$ (553 nm).[15-17]

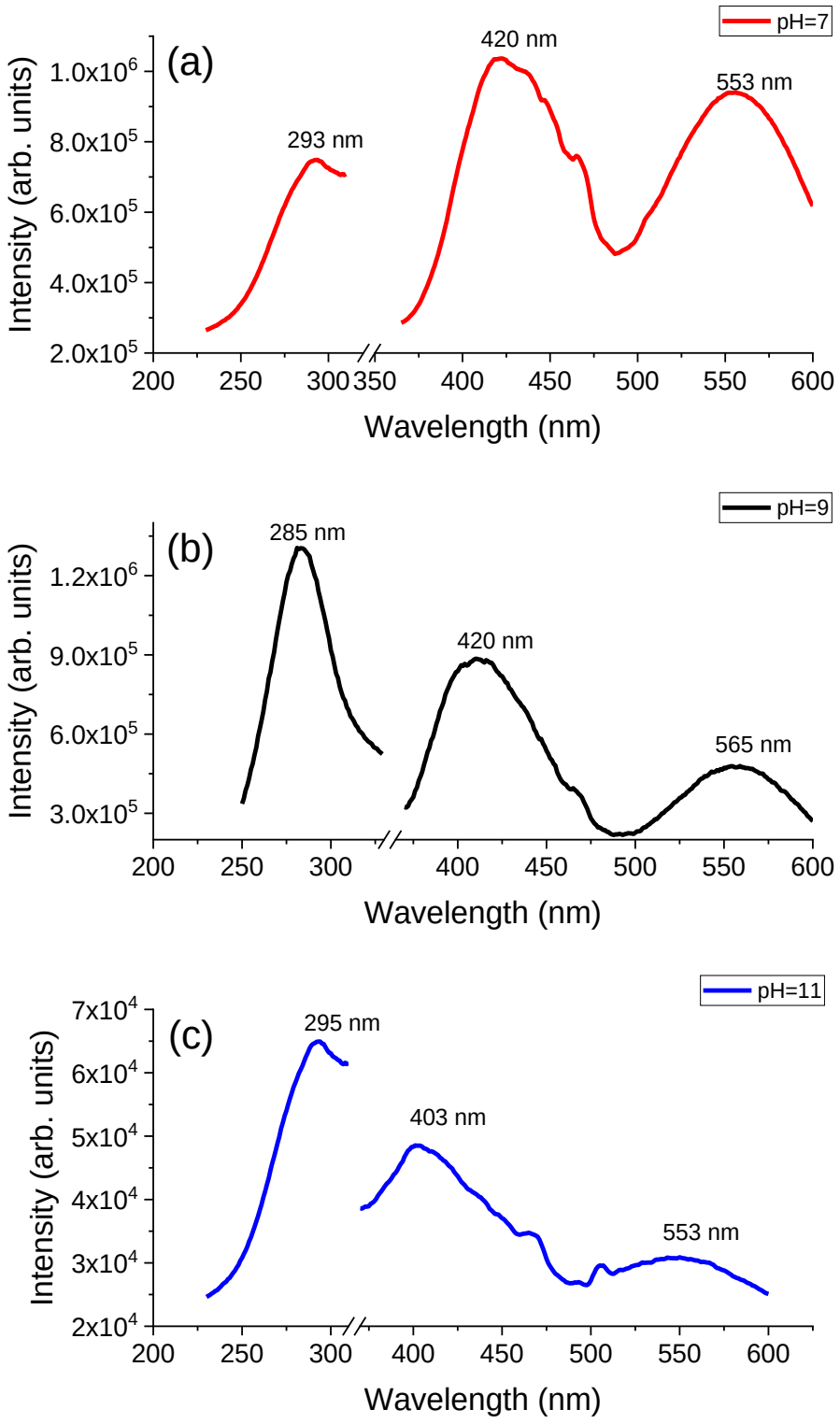

Figure 4- 4. The excitation scan of samples synthesized under different pH values. (a) pH= 7. (b) pH=9. (c) pH=11.

Using these excitation wavelengths, the emission spectra of all three samples are obtained, shown in Figure 4-5. All Cr-ZGO samples synthesized under different pH values have similar Cr-related emission profiles: a characteristic N2 band (696 nm), zero phonon (680-687 nm) and by Stokes (S-PSB) (708-715 nm) and anti-Stokes phonon side bands (AS-PSB) (660-680 nm).[7,18-21] However, the emission intensities relative to the excitation wavelength vary: for the pH=7 sample, the strongest emission was obtained using visible light (420 nm and 553 nm), while the pH=9 and pH=11 samples exhibit the strongest emission under UV excitation. The emission caused by UV excitation involves the energy transfer from the host to Cr^{3+}, a relatively low intensity could be due to structural defects such as the oxygen vacancies. Based on the results obtained from Chapter 3, such vacancies are likely around Zn. We will return to this point later.

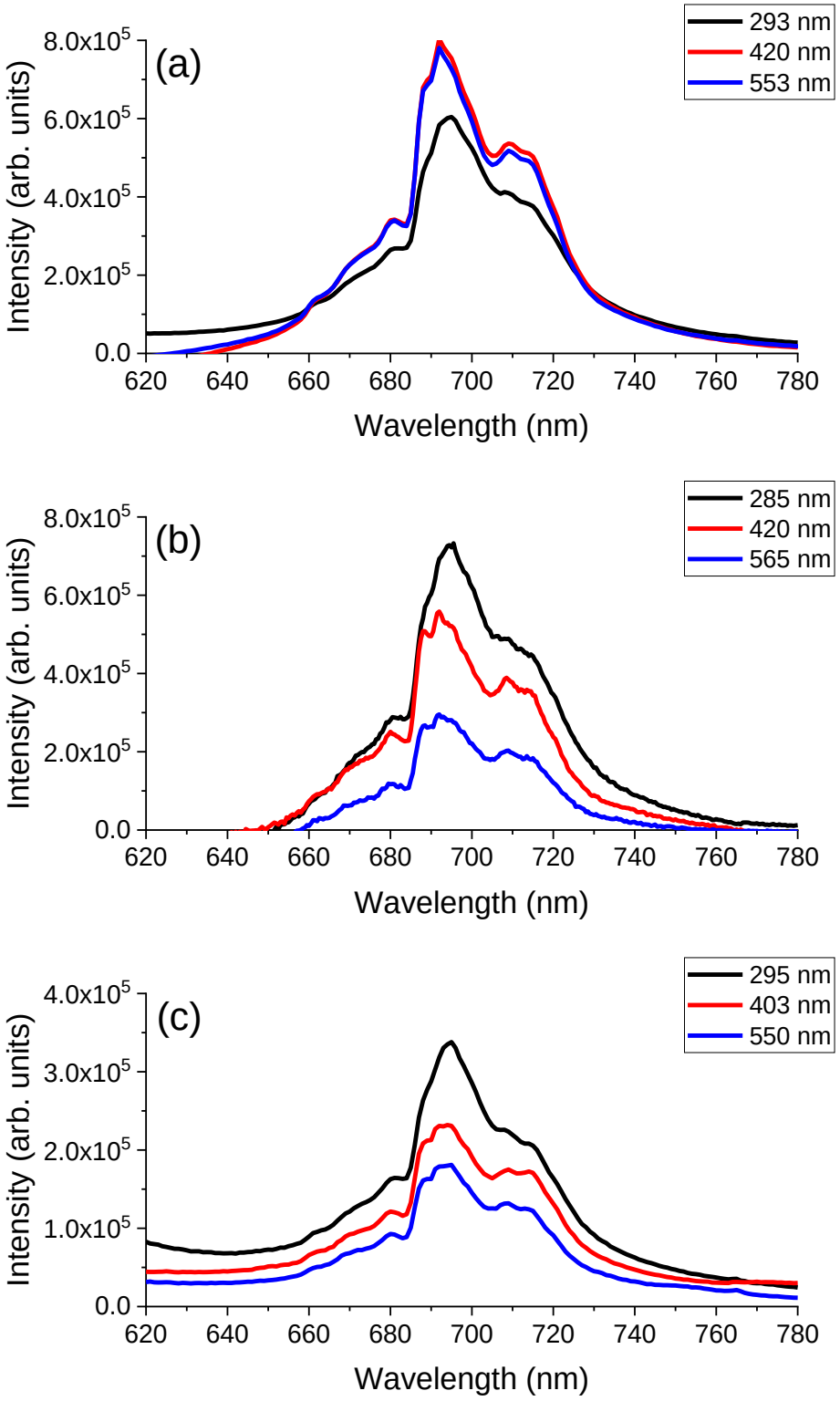

Figure 4- 5. Emission spectrums of synthesized pH different Cr-ZGO samples (a) pH=7. (b) pH=9. (c) pH=11.

Next the relative emission intensities of the three samples are compared. The results are shown in Figure 4-6. The pH=11 sample has the lowest emission intensity regardless of excitation wavelengths. shows an apparent weak overall emission. The results correspond to the picture under UV light. For the emission caused by 285 nm, pH=9 sample shows an obviously strong overall emission, and pH=7 sample shows the strongest emissions caused by 415 nm and 555 nm. It should also be noticed that pH=7 sample shows the emission constantly around 600000 to 750000 arb. units. With the change of excitation wavelength, the emissions caused by different wavelengths are not significantly changed; however, the pH=9 sample's emissions decrease significantly when the excitation wavelength changes from 285 to 555 nm. pH=11 sample shows a similar trend to pH=9 sample but the decrease is not significant. Overall, pH=7 exhibits strong luminescence ability, and pH=11 exhibits the weakest luminescence capability. In addition, the emission details are also not entirely the same. All lines are broad in Figure 4-6 (a) but Figure 4-6 (b) and (c) contain sharper features. This could be explained that host absorption, which is an energy transfer (ET) from the host to Cr^{3+} that happens in the excitation band at 285 nm, weakens the representation of these sharper features.

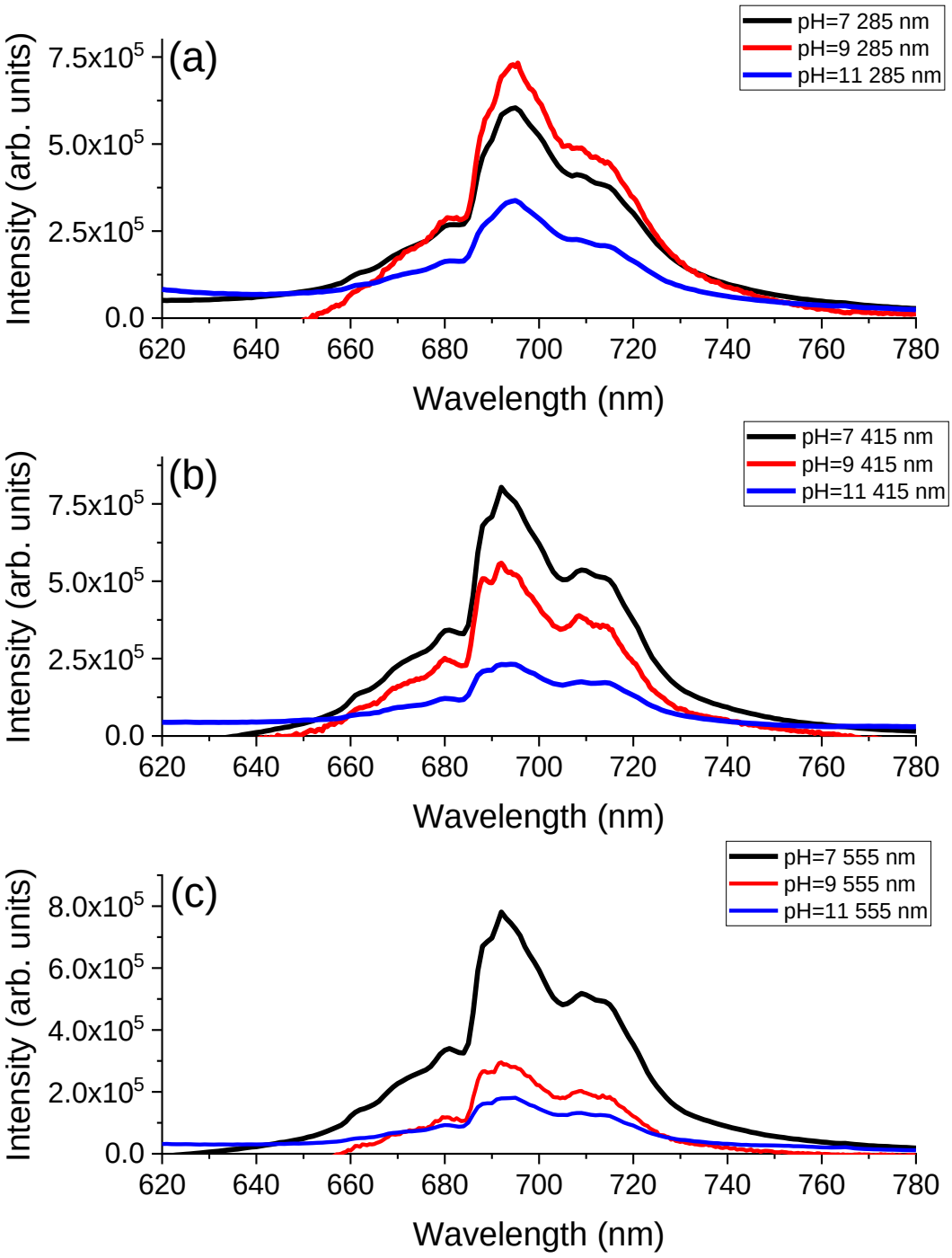

Figure 4- 6. The PL intensity comparison of pH different samples under (a) 285 nm, (b) 415 nm and (c) 555 nm.

4.3.3.2 Cr-ZGO Synthesized with different base addition rates

Figure 4-7 shows the excitation spectra of Cr-ZGO synthesized with different base addition rates. It turns out Cr-ZGO samples prepared with both slow rate and fast rate have relatively low luminescence intensities under visible light excitation (409 nm and 553 nm). There are some potential reasons for this. First, too fast addition may lead to hydroxy complexes precipitates accumulating. This will result in an inadequate reaction for the formation of hydroxy complexes and Cr-ZGO. On the other hand, due to different metal cations and hydroxide binding ability, too slow addition may affect the formation sequence and concentration of metal hydroxide.[22] However, the real reason needs further investigation.

Figure 4-8 compares the luminescence intensities of the three Cr-ZGO when excited at the same wavelength. Under all three wavelengths, the medium rate Cr-ZGO shows the strongest overall emission, and the fast base addition Cr-ZGO shows the weakest overall emission. The effect of inadequate reaction on luminescence intensity is enormous.

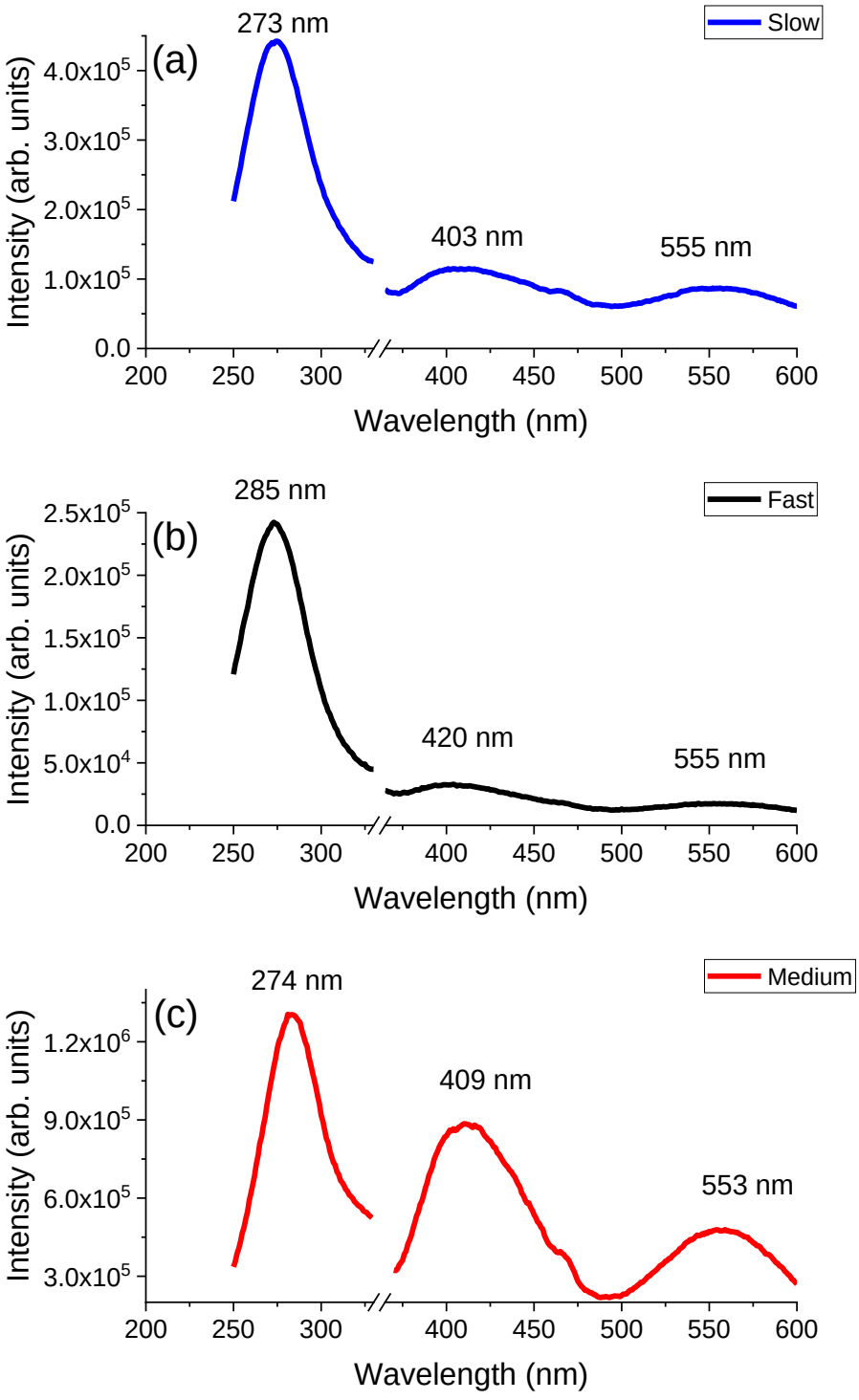

Figure 4- 7. The photoluminescence spectroscopy of different base addition rates Cr-ZGO. (a) the excitation scan of fast base addition Cr-ZGO (b) the excitation scan of medium - rate base addition Cr-ZGO (c) the excitation scan of slow base addition Cr-ZGO.

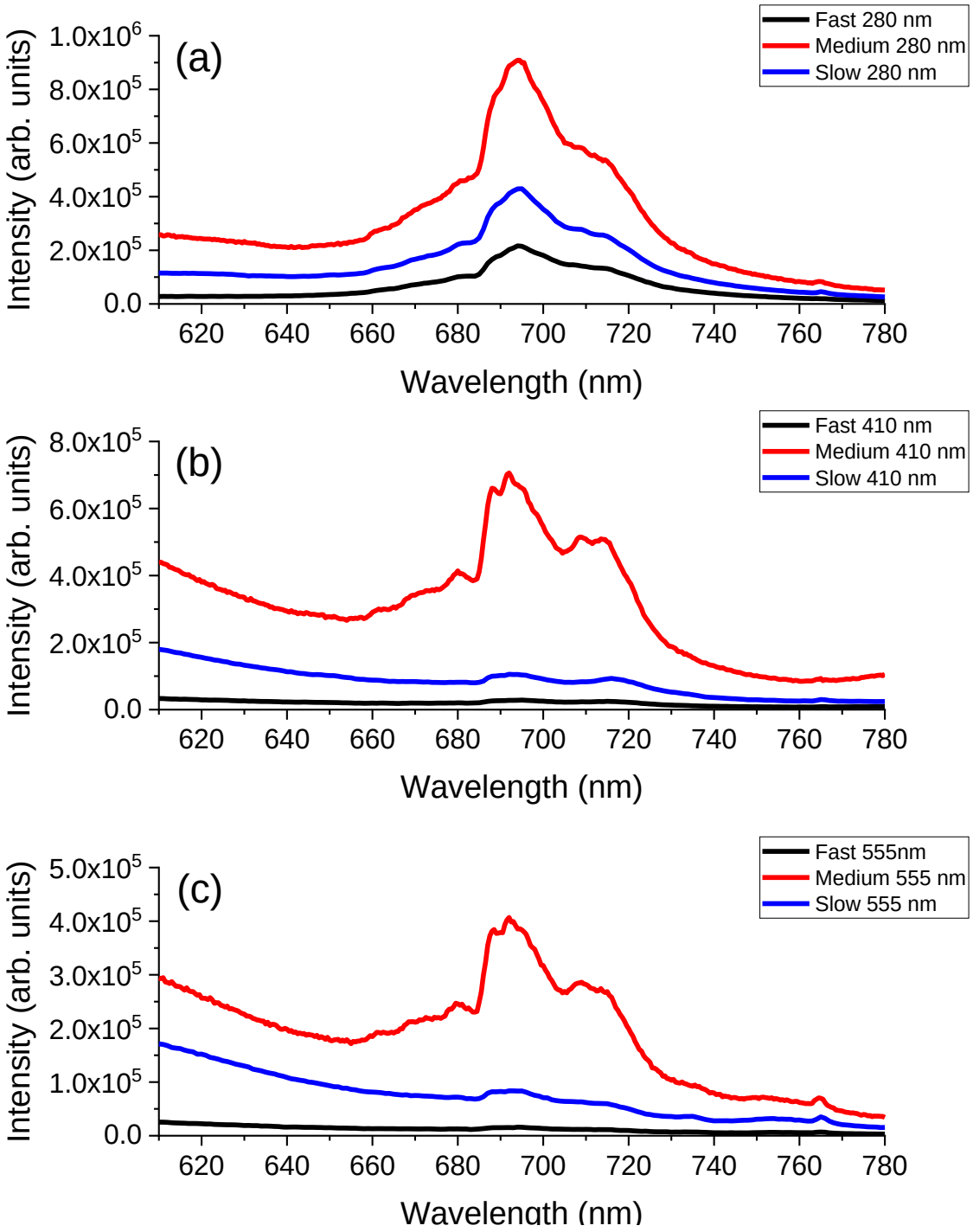

Figure 4- 8. The luminescence intensity comparison among the slow base addition ZGO, medium base addition ZGO and fast base addition ZGO. (a) 280 nm (b) 410 nm (c) 555 nm.

4.3.4 Electronic Structure

Since medium base addition rate Cr-ZGO shows the strongest overall emission, samples with medium base addition rate but under different pH environments (pH=7, 9, 11) will be used for the study of electronic structure.

4.3.4.1 The Zn K-edge XAFS

The Zn K-edge XANES of the three Cr-ZGO samples synthesized under different pH environments is shown in Figure 4-9. Comparing with the reference ZnO sample, the Cr-ZGO samples show two typical peaks at 9668 eV and 9673 eV and an obvious peak shape change. This peak shape change is the same as the energy shift of different temperature ZGO samples, indicating that the pH variation has no effect on the peak shape change. It has been discovered that a high pH value causes high intensity, which suggests that the 4p orbitals of Zn are emptier for the sample under a high pH value. Since the 4p occupancy can be related to the number of coordinated O atoms around Zn, it proves the previous predictions. The 4p orbitals of Zn are more occupied meaning there will be fewer oxygens surrounding Zn, and the low pH environment will cause more oxygen vacancies around Zn. For the pH values modified ZGO samples, there are some charge redistributions within the 4p orbital. The highest occupied 4p orbital is seen in the pH=7 sample, indicating that there are more oxygens near Zn. The pH=11 sample has the least occupied 4p orbital, implying that there are fewer oxygens near Zn.

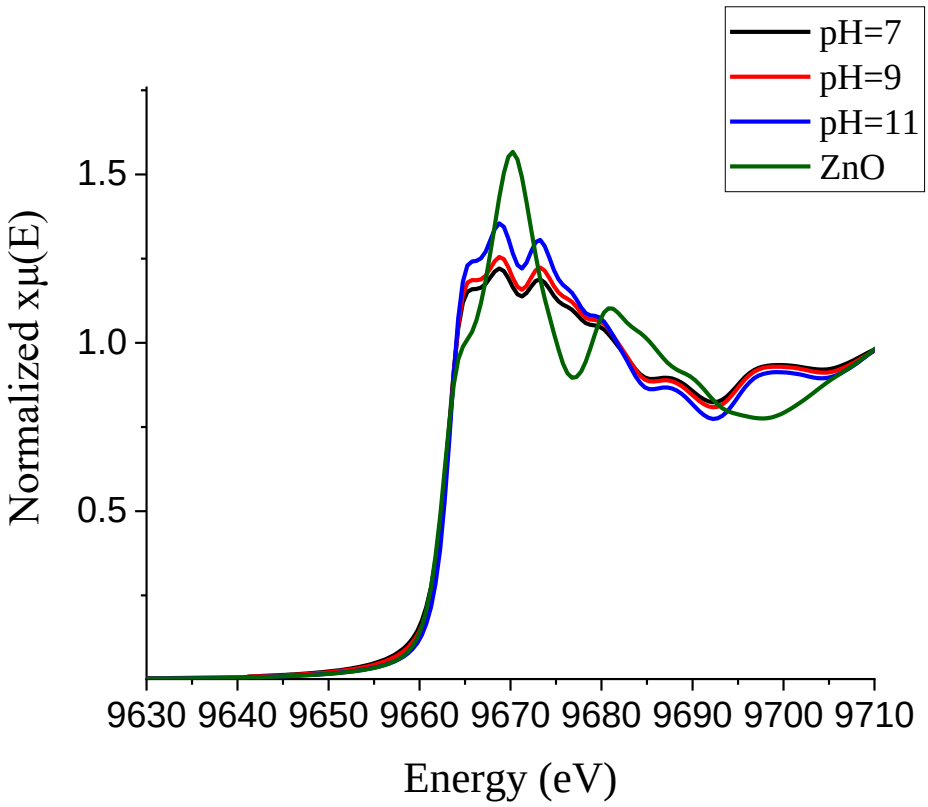

Figure 4- 9. Zn K-edge XANES of Cr-ZGO samples synthesized under different pH environment. ZnO is as a reference.

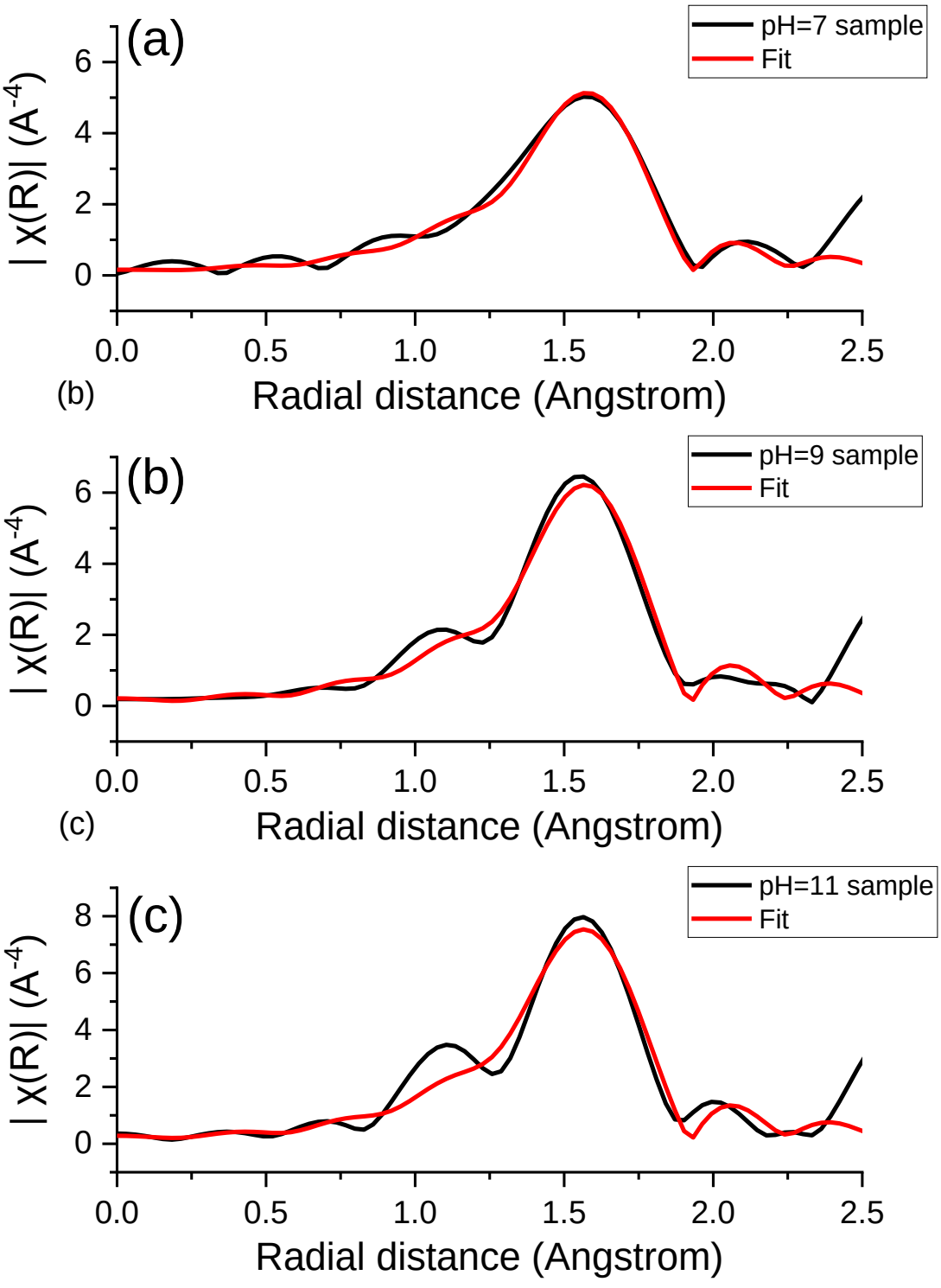

Figure 4- 10. The Zn K-edge EXAFS first-shell fitting for Cr-ZGO samples plotted in R-space (a) pH=7 sample. (b) pH=9 sample. (c) pH=11 sample.

Figure 4-10 shows the Zn K-edge EXAFS of the Cr-ZGO samples using a Zn-O single scattering path from a model ZGO compound, plotted at the R-space, with the first-shell fit.[23] Detailed fitting parameters are summarized in Table 4-3. The pH=7 sample shows a relatively high σ^2. This means the oxygen shell is more disordered; however, when pH reaches 9 and 11. The pH change effect is inconspicuous. Comparing with the theoretical 4 oxygen atoms around one Zn atom, the pH increase will lead to less oxygen vacancy around Zn. This is consistent with the predictions in the optical section.

In Chapter 3, we have proposed that oxygen vacancy around Zn will affect the relative luminescence intensity caused by 290 nm for the same sample by comparing with emission caused by 420 nm and 555 nm but it will help with increasing the overall luminescence intensity. The results shown in Table 4-3 confirm this conclusion. In Figure 4-5, pH=7 sample shows a relatively weak emission caused by 293 nm but its overall luminescence intensity shows a strong emission comparing with pH=9 and pH=11 samples, and the EXAFS fitting results show pH=7 sample has the most oxygen vacancy defects. This confirms the conclusion from chapter 3.

Table 4- 3. The fitting results with structure information for Cr-ZGO synthesized under different environment.

pH environment	CN	R (Å)	σ^2 (Å^2)	ΔE_0(eV)
pH=7	2.3 ± 0.2	1.981 ± 0.008	0.005 ± 0.001	3.0 ± 1.0
pH=9	2.5 ± 0.2	1.973 ± 0.009	0.004 ± 0.001	2.6 ± 1.2
pH=11	3.3 ± 0.4	1.973 ± 0.009	0.005 ± 0.002	2.3 ± 1.6

Notes: CN, coordination number; R(Å), interatomic distance. σ^2 (Å^2), the Debye-Waller factor (mean square relative displacement); ΔE_0 (eV), the difference between experimentally determined threshold energy and the FEFF calculated threshold energy.

4.3.4.2 The Ga K-edge XAFS

Figure 4-11 shows Ga K-edge XANES spectra of the three samples in comparison with the spectrum of Ga_2O_3. For the main resonance (from 10364 eV to 10373 eV) of samples, pH=9 and pH=11 samples show a 1.5 eV energy shift comparing with Ga_2O_3. The energy shift and intensity change still show the charge redistributions happened in 4p orbitals. pH=11 sample shows the most occupied 4p orbital, which suggests there are fewer oxygens around Ga in pH=11 sample. pH=7 sample shows the least occupied 4p orbital, which suggests there are more oxygens around Ga in pH=7 sample. This shows a reverse trend comparing with Zn XANES, which indicates that if there are more oxygen vacancies around Zn, there will be fewer oxygen vacancies around Ga.

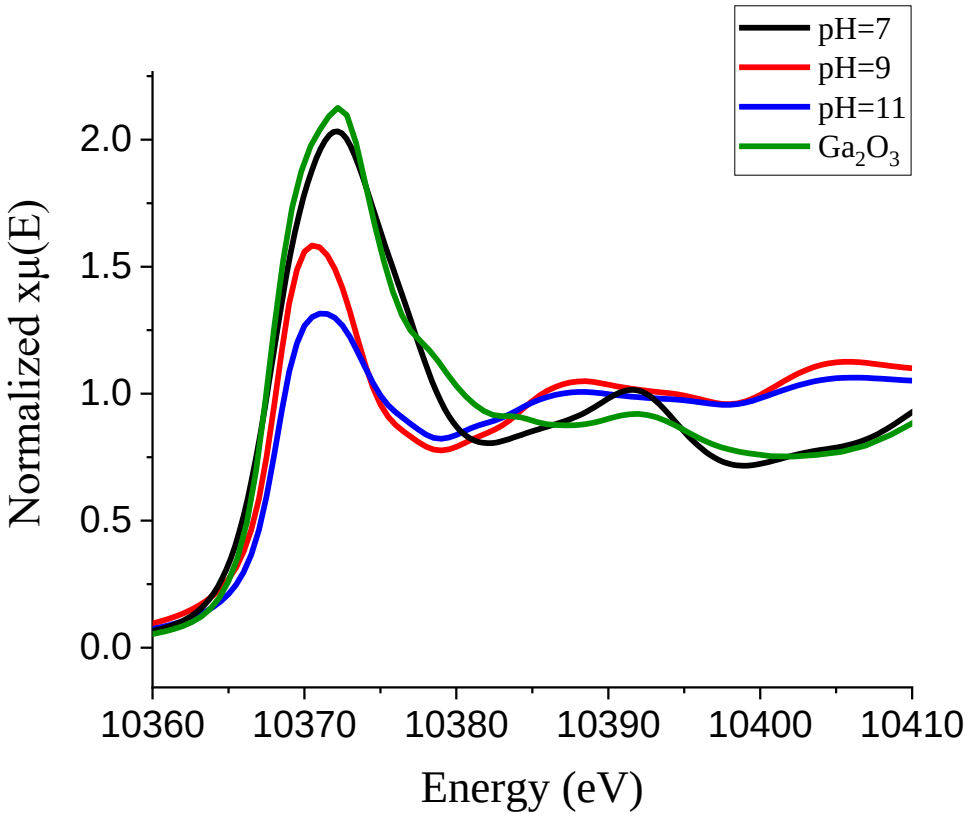

Figure 4- 11. Ga K-edge XANES of ZGO samples synthesized under different pH values. Ga_2O_3 is as reference.

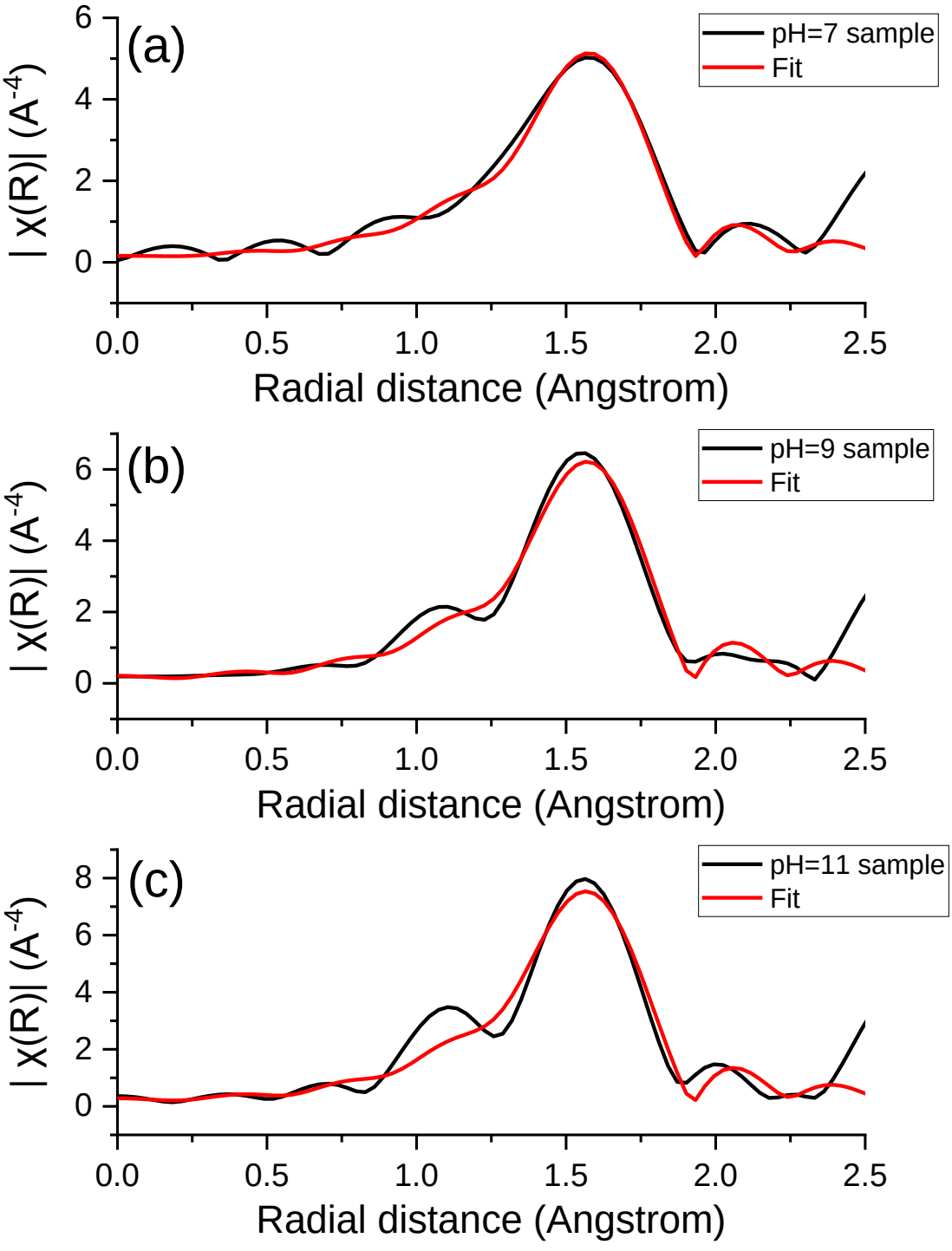

Figure 4- 12. The Ga K-edge EXAFS first-shell fitting of Cr-ZGO plotted in R-space. (a) pH=7 sample. (b) pH=9 sample. (c) pH=11 sample.

The EXAFS R space fitting of the first shell of Ga in Cr-ZGO is shown in Figure 4-12. By choosing the single scattering path of Ga to O, the main peak shape of the first shell is fitted with k weighting equal to 2 produced by forward Fourier transformations.[23] The fitting result fits the first shell and shows that there is an ordered coordinating oxygen shell around Ga. The fitting results shown in Table 4-4 suggest that similar to Zn, the pH change effect on the change of R is irregular but it is noticed that the low pH sample has a more disordered oxygen shell due to the high value of σ^2. pH=11 sample shows a low coordination number, and the low coordination number and weak luminescence confirm the previous conclusion which is oxygen vacancy around Ga will impair the overall luminescence. pH=11 sample, which has the weakest overall emission, shows low coordination numbers according to the EXAFS.

Table 4- 4. EXAFS fitting results of Ga.

	CN	R (Å)	σ^2 (Å^2)	ΔE_0(eV)
pH=7	4.1 ± 0.8	2.11 ± 0.02	0.008 ± 0.003	-8.5 ± 2.7
pH=9	4.1 ± 0.7	1.98 ± 0.02	0.008 ± 0.003	7.0 ± 1.5
pH=11	1.9 ± 0.2	2.11 ± 0.01	0.005 ± 0.002	-7.2 ± 1.2

Notes: CN, coordination number; R(Å), interatomic distance. σ^2 (Å^2), the Debye-Waller factor (mean square relative displacement); ΔE_0 (eV), the difference between experimentally determined threshold energy and the FEFF calculated threshold energy.

4.3.4.3 The Cr K-edge XANES

In Figure 4-13, Cr K-edge XANES spectra depict that the pre-edge regions for ZGO samples synthesized under different pH values are from 5988 eV to 5992 eV, which only shows a slight difference of intensity (pH=11, 7, 9 from highest to lowest intensity), and

the main resonance is from 5992 eV to 6014 eV where pH=7 shows the most intense peak followed by pH=9 then pH=11. Because the emissions by 420nm and 555 nm excitation are caused by the energy transfer in 3d orbitals, due to the low occupied 3d orbitals of pH=11 sample, the relative emissions by 420nm and 555 nm excitation (Figure 4-11(c)) are the relative weakest comparing with pH=7 and 9 samples (Figure 4-11(a) and Figure 4-11(b)). The main resonance shows an obvious difference. The Cr 4p orbitals in the pH=7 sample are less occupied. The pH change does not show very significant variation for peaks C and D. This means pH change does not affect the order of structure as significantly as temperature but the peak shape still indicates Cr replaces Ga forming CrO_6 octahedra since it has a similar line shape and features to Ga XANES.[17] For the pre-edge part, peak P-A and peak P-B show a similar result to the temperature chapter. However, peak P-B becomes relatively weak. This indicates that $1s \rightarrow e_g$ transition is not dominant, and e_g energy state is relatively full.

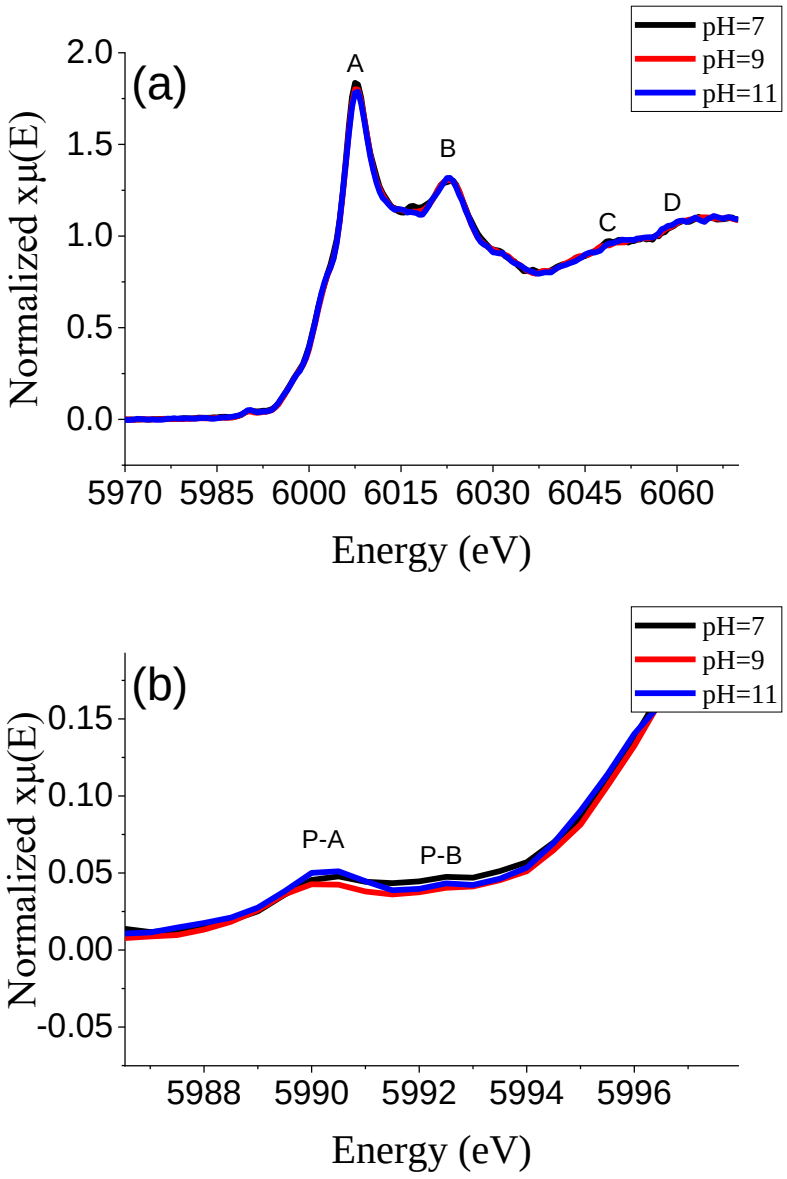

Figure 4- 13. The Cr K-edge XANES of Cr-ZGO samples synthesized under different pH (a) the overview of the Cr K-edge XANES of Cr-ZGO samples synthesized under different pH. (b) A magnified view at the pre-edge region.

4.4 Conclusion

Cr-ZGO samples are successfully synthesized under different pH values and base addition rates but with the same synthesized temperature at 220 ℃. High pH values cause a

significant increase in the crystal size, and when pH changes from 9 to 11, the size increases significantly. In terms of base addition rate, a slow base added manner will lead to a larger crystal size. This is probably because the accumulation of hydroxy complexes precipitates. For the PL spectroscopy, Cr-ZGO samples synthesized under different pH values show characterized peaks around 700 nm, which is similar to chapter 3. The UV light displays pH=7 sample has the strongest luminescence, and this is confirmed by qualitative PL comparison. The qualitative PL comparison also indicates pH=11 sample has the weakest luminescence. In terms of the PL of different base addition rates samples, the medium addition base will improve the luminescence slightly. The XANES of Zn and Ga both suggest the charge redistributions happen in 4p orbitals, and the EXAFS fitting results confirm the conclusion from the temperature changed chapter, which is both oxygen vacancy around Ga and Zn will affect the relative intensity for one same sample but oxygen vacancy around Ga will decrease the overall luminescence intensity, and oxygen vacancy around Zn will increase the overall luminescence intensity. pH=7 sample with the strongest luminescence caused by the visible lights shows the most vacancies around Zn, and those vacancies capture more charge carriers leading to stronger emission. pH=11 sample with the weakest luminescence shows the most vacancies around Ga, and those vacancies capture the charge carries strongly with a low releasing rate leading to weak emission. The XANES of Cr also confirms the Cr replacement of Ga but pH change does not affect the order of the structure of ZGO as significantly as temperature change.

4.5 References

[1] Dai, Q., Zhang, Z., Zhan, T., Hu, Z-T., Chen, J. *ACS Omega*. **2018**, 3, 6506–6512.

[2]Strachowski, T., Grzanka, E., Mizeracki, J., Chlanda, A., Baran, M., Małek, M., Niedziałek, M. *Materials*. **2021**, 15, 245.

[3] Chen, Z., Zhao, X., Wei, S. *Optik*. **2021**, 242, 167151.

[4] Guo, W., Wu, Y., Tian, Y., Lian, X., Li, J., Wang, S. *ChemElectroChem*. **2019**, 6, 4645–4652.

[5] Chen, L., Liu, Y., Lu, Z., et al. *Mater. Chem. Phys*. **2006**, 97, 247-251.

[6] Li, Z., Zhang, Y., Wu, X., Huang, L., Li, D., Fan, W., Han, G. *J. Am. Chem. Soc*. **2015**, 137, 5304–5307.

[7] Srivastava, BB., Kuang, A., Mao, Y. *ChemComm (Cambridge, England)*. **2015**, 51,7372–7375.

[8] Maldiney, T., Bessière, A., Seguin, J., Teston, E., Sharma, SK., Viana, B., Bos, AJJ., Dorenbos, P., Bessodes, M., Gourier, D., et al. *Nat. Mater*. **2014**, 13, 418–426.

[9] Wang, Y., Yang, C-X., Yan, X-P. *Nanoscale*. **2017**, 9, 9049–9055.

[10] Wang, H-F., Chen, X., Feng, F., Ji, X., Zhang, Y. *Chem. Sci*. **2018**, 9, 8923–8929.

[11] Tuerdi, A., Abdukayum., A. *RSC Adv*. **2019**, 9, 17653–17657.

[12] Luan, T., Liu, J., Yuan, X., Li, J-G. *Nanoscale Res. Lett*. **2017**, 12, 1–219.

[13] Sun, M., Li, D., Zhang, W., Chen, Z., Huang, H., Li, W., He, Y., Fu, X. *J. Solid State Chem.* **2012**, 190, 135–142.

[14] Basavaraju, N., Priolkar, KR., Gourier, D., Bessière, A., Viana, B. *Phys. Chem. Chem. Phys.* **2015**, 17, 1993–1999.

[15] Zhou, Z., Zheng, W., Kong, J., Liu, Y., Huang, P., Zhou, S., Chen, Z., Shi, J., Chen, X. *Nanoscale*. **2017**, 9, 6846–6853.

[16] Lakshmi Reddy, S., *Electronic (Absorption) Spectra of 3d Transition Metal Complexes*. IntechOpen; 2012.

[17] Mian, F., Bottaro, G., Wang, Z., You, Y-M., Rancan, M., Sham, T-K., Armelao, L. *Appl. Surf. Sci.* **2022**, 577, 151896 .

[18] Bessière, A., Jacquart, S., Priolkar, K., Lecointre, A., Viana, B., Gourier, D. *Opt. Express*. **2011**, 19, 10131-10137.

[19] Mikenda, W., Preisinger, A. *J. Lumin*. **1981**, 26, 53–66.

[20] Mikenda, W., Preisinger, A. *J. Lumin.* **1981**, 26, 67–83.

[21] Bessière, A., Sharma, SK., Basavaraju, N., Priolkar, KR., Binet, L., Viana, B., Bos, AJJ., Maldiney, T., Richard, C., Scherman, D., et al. *Chem. Mater.* **2014**, 26, 1365–1373.

[22] Li, K., Li, M., Xue, D. *J. Phys. Chem. A.* **2012**,116, 4192–4198.

[23] Allix, M., Chenu, S., Véron, E., Poumeyrol, T., Kouadri-Boudjelthia, EA., Alahraché, S., Porcher, F., Massiot, D., Fayon, F. *Chem. Mater*. **2013**, 25, 1600–1606.

Chapter 5

5 Investigating the Influence of Functionalization on the Luminescence of Cr-doped $ZnGa_2O_4$

In this chapter, a study on the influence of functionalization on the luminescence property of Cr-ZGO under hydrothermal conditions is presented. The PL and IR of functionalized Cr-ZGO synthesized under hydrothermal conditions will be discussed.

5.1 Introduction

When a material is applied in the biological field, stability, selectivity and biocompatibility are key factors needed to be considered. In biological application, the in vivo system is extremely complex. The pH, ion strength and the chemical environment such as the presence of biomolecules can affect the stability and biocompatibility of material significantly, and the selectivity can affect the performance of target trace and identification ability.[1, 2] Therefore, the surface of a material needs to be modified so that it remains stable in the biophysical environment. For example, $SrAl_2O_4:Eu^{2+}$, Dy^{3+} (SAO), which can be used as a biological marker due to ten hours of luminescent in blue-green region, becomes partially hydrolyzed because water molecules can easily enter the channels formed by the AlO_6^- and AlO_4^- .[3, 4] However, after modifying the SAO with pyrophosphoric acid (PPA) and Poly(ethylene glycol) methyl ether (PEG-5000-OCH_3), the functionalized SAO is stable in an aqueous solution for more than 3 days with excellent water-dispersibility.[5] When the nude Cr doped $ZnGa_2O_4$ (Cr-ZGO) is utilized in the biological system, it shows a poor monodispersity. This will lead to the agglomeration of particles and affect suspension stability.[6] In addition, in complicated biological systems, nude Cr-ZGO has poor targeting capacity and lacks particular identification ability, which will lower the bioimaging selectivity dramatically.[1,7] To improve the stability of Cr-ZGO, the hydroxyl group is used to functionalize Cr-ZGO. Electrostatic repulsions of O^- caused by hydroxyl group can avoid aggregation of Cr doped $ZnGa_2O_4$ (Cr-ZGO). Due to this

property, hydroxyl functionalized Cr-ZGO shows an excellent colloidal stability in 30 mM phosphate buffers pH 7.0–8.0 and in 30 mM citrate buffers pH 4.5–5.5.[8] In terms of selectivity, KGPNQC is a peptide that can be cleaved by fibroblast activation protein-alpha (FAPα). KGPNQC can be used to functionalize Cr-ZGO to improve the selectivity. In the test of selectivity among fibroblast activation among protein-alpha (FAPα), human dipeptidyl peptidase-IV (DPPIV), which is extremely similar to FAPα, and human serum albumin (HSA), which is the most abundant protein in human serum, it turns out only with the existence of FAPα, the afterglow is detected. Biocompatibility presents the feasibility of using the material in vivo.[1, 9] Moreover, toxicity is another concern for the biological use of Cr-ZGO. By modifying Cr-ZGO with α, ω-dicarboxyl-terminated PEG (MW = 2000) and polyacrylic acid (PAA), the in vitro relative cell viabilities are markedly improved after Cr-ZGO conjugation with the peptide.[10]

However, functionalization also brings up some drawbacks. It has been noticed that the surface functionalization will quench the luminescence dramatically due to the energy transfer process from materials to modifiers.[1] For instance, the persistent luminescence of MnO_2 coated $Zn_3Ga_2GeO_8$ reduces dramatically comparing with nude $Zn_3Ga_2GeO_8$, and the quenching becomes more obvious with more MnO_2 shells formed.[11] However, the reported studies on functionalized Cr-ZGO to date didn't include discussion on whether the functionalization impacts the original luminescence intensity of Cr-ZGO, and whether such influence applies to all Cr-ZGO systems regardless of their preparation condition. In the previous chapters, it has been found that different synthesis temperatures and pH values will affect the luminescence intensity and the electronic structure of the Cr-ZGO. In this chapter, a comparative study is performed on the luminescence of Cr-ZGO nanoparticles after hydroxyl- and aminosilane-functionalization, respectively. Hydroxyl group functionalization, is normally the first step of functionalizing Cr-ZGO.[8, 12, 13] It is a standard modification procedure for various materials, and it can provide colloidal stability for particles.[14, 15] In addition, hydroxyl functionalized Cr-ZGO has been successfully applied to in vivo imaging trapping within the liver due to the negative charge on the surface.[12] In terms of aminosilanized Cr-ZGO samples, surface amination will aid in the conjugation of several biofunctional compounds such as folic acid (FA), peptide, polyethylene glycol

(PEG), DNA, bovine serum albumin (BSA), hyaluronic acid (HA) and antibody due to the reaction with carboxylic acid group.[13, 16]

5.2 Experimental

5.2.1 Chemicals and Instrumentation

3-Aminopropyl-triethoxysilane (APTES, $H_2N(CH_2)_3Si(OC_2H_5)_3$, 99%), Gallium(III) nitrate hydrate ($Ga(NO_3)_3 \cdot xH_2O$, crystalline, 99.9% trace metals basis), zinc nitrate hexahydrate ($Zn(NO_3)_2 \cdot 6H_2O$, reagent grade, 98%), and ammonium hydroxide solution (NH_4OH, 28%, wt) were commercially obtained from Sigma Aldrich. Chromium (III) nitrate nonahydrate ($Cr(NO_3)_3 \cdot 9H_2O$, 98.5%) and hydrochloric acid solution (HCl, 36.5-38.0%) were commercially obtained from Alfa Aesar. Sodium Hydroxide (NaOH, 98%) and N,N-Dimethylformamide (DMF, $HCON(CH_3)_2$, ≥99.7%) were obtained from Fisher Scientific. was obtained from. All the chemicals were used without any purification.

5.2.2 Synthesis of Cr-ZGO

All the samples were synthesized using a hydrothermal method according to the description in Chapter 2.[17] For the samples synthesized at different pH environments, pH was changed, and the hydrothermal temperature was set to 220 ℃. For the samples under different synthesis temperatures, the hydrothermal temperature was changed, and the pH was set to 9.

The samples under different hydrothermal temperatures will be called as Cr-ZGO-120, Cr-ZGO-170 and Cr-ZGO-220 corresponding to 120 ℃, 170 ℃ and 220 ℃, respectively in the following statement. The samples under different synthesis pH values will be called as Cr-ZGO-7, Cr-ZGO-9 and Cr-ZGO-11 corresponding to pH=7, 9 and 11, respectively in the following statement.

5.2.3 Hydroxyl Functionalized Cr-ZGO

Hydroxyl functionalization of Cr-ZGO was performed by basic wet grinding 1 drop of 5.0 mM NaOH solution was added to 100 mg Cr-ZGO powder and the powder was ground for

15 min. In the middle of grinding, another drop of 5.0 mM NaOH solution was added to keep the powder wet. The resulted powder was dispersed in 10 ml 5.0 mM NaOH. The solution was vigorously stirred at room temperature overnight. The as-formed precipitate was collected by centrifuge at 4500 rpm for 7 min. Then 5 ml DI water was added into a centrifuge tube to wash the crude product, and the mixture was centrifuged at 4500 rpm for 7 min. The solid powder was collected and dried at 60 ℃ for 24 hours.[8] The samples with conditions are named as Cr-ZGO-120-OH, Cr-ZGO-170-OH, Cr-ZGO-220-OH, Cr-ZGO-7-OH, Cr-ZGO-9-OH and Cr-ZGO-11-OH respectively based on previous names.

5.2.4 Aminosilanized Cr-ZGO

200 μL of APTES was added to a suspension of 50 mg Cr-ZGO samples in 20 ml of DMF under vigorous stirring for 4 hours at room temperature. The precipitate was obtained by centrifuge at 4500 rpm for 7 min. Then 5 ml DMF was added into centrifuge tube, and the centrifuge tube was shaken to wash the precipitate. Next precipitate samples were obtained by centrifuge at 4500 rpm for 7 min. the samples were dried at 60 ℃ for 24 hours.[18] The samples with conditions will be called as Cr-ZGO-120-NH_2, Cr-ZGO-170-NH_2, Cr-ZGO-220-NH_2, Cr-ZGO-7-NH_2, Cr-ZGO-9-NH_2 and Cr-ZGO-11-NH_2 respectively based on previous names.

5.3 Results and Discussion

5.3.1 Hydroxyl functionalization to Cr-ZGO prepared under different hydrothermal temperatures

Hydroxyl (OH) functionalization was done to Cr-ZGO synthesized at three different hydrothermal temperatures. The FT-IR spectra of each Cr-ZGO before and after OH functionalization were compared in Figure 5-1. All three samples show peaks at around 3400 cm^{-1}, 3230 cm^{-1}, 1634 cm^{-1}, 1336 cm^{-1}, 569 cm^{-1} and 419 cm^{-1}. For all samples, peaks around 3400 cm^{-1}, 1634 cm^{-1}, 569 cm^{-1} and 419 cm^{-1} remains unchanged after hydroxyl functionalization. The peak around 3400 cm^{-1} is most likely due to O-H stretching of either

water or hydroxyl groups or both since the samples have not annealed over 100 ℃. Peaks around 569 cm^{-1} and 419 cm^{-1} are caused by Zn-O and Ga-O vibration, respectively.[18] The peak around 1634 cm^{-1} is assigned to N-H bending. This suggests that there may be some ammonium ions on the surface. However, a pure Cr-ZGO sample should only have Zn-O and Ga-O vibrations. The ammonium ions probably come from ammonium hydroxide during the synthesis.

Since the ammonium ions exist, the peak around 3230 cm^{-1} can be assigned as N–H stretch. However, peaks around 3230 cm^{-1} and 1336 cm^{-1} are obviously changed. The disappearance of the peak around 3230 cm^{-1} after hydroxyl functionalization shows the evidence that hydroxyl group replaces the ammonium ions on the surface. In addition, the peak around 1336 cm^{-1} can be assigned as N-O stretching. This shows the evidence of nitrate. The disappearance of the N-H bending peak and N-O stretching peaks confirms the ammonium ions and nitrate are replaced on the surface.

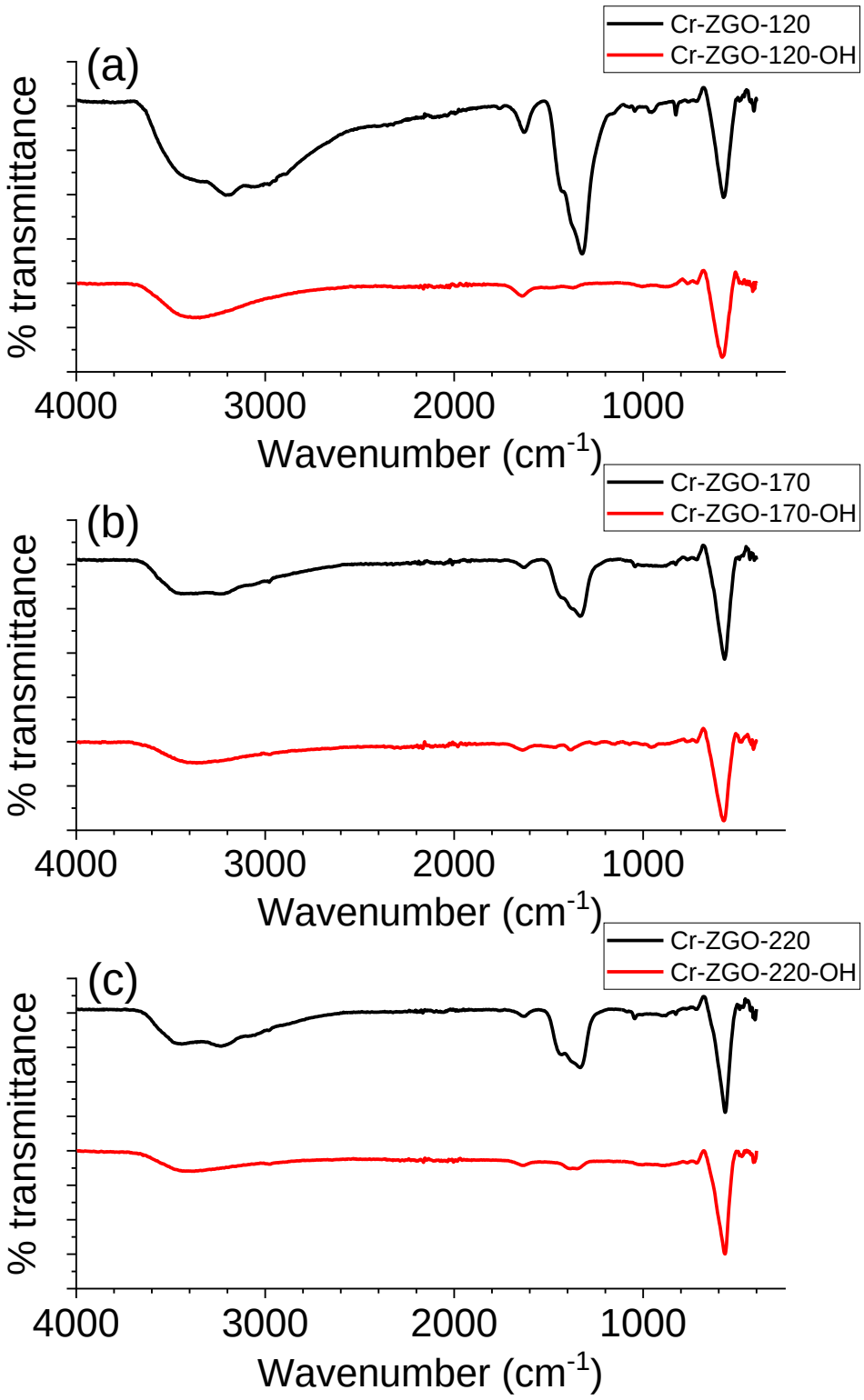

Figure 5- 1. The FTIR spectra of Cr-ZGO and OH functionalized Cr-ZGO under different temperatures. (a) 120 ℃. (b) 170 ℃. (c) 220 ℃.

Figure 5-2 shows the comparison of the luminescence intensities of Cr-ZGO before and after functionalization. The photographs were taken under the UV-light. The luminescence of all samples, regardless of synthesis temperature, decreases drastically after OH functionalization. Such influence is the strongest on Cr-ZGO-120-OH. To quantify luminescence variation, photoluminescence spectra were acquired from these samples.

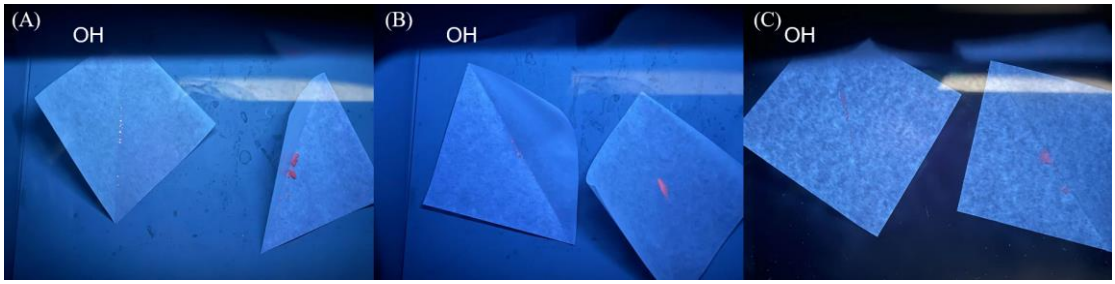

Figure 5- 2. The comparison of Cr-ZGO before and after hydroxyl functionalization under UV-light (254 nm). The left sample is after hydroxyl functionalization. (a) 120 ℃. (b) 170 ℃. (c) 220 ℃.

To avoid repetition, Cr-ZGO-220 is used as an example to demonstrate the extent of PL decrease after functionalization. Cr-ZGO-220 has three excitation bands, as mentioned in previous chapters, at 285 nm, 420 nm, and 565 nm, respectively. Therefore, the PL were taken at all three excitation wavelengths, shown in Figure 5-3. The sample after hydroxyl functionalization shows at least 30 times weaker luminescence than the sample before functionalization. The emission caused by around 420 nm is affected most, which shows at least 60 times weaker luminescence, and the emission caused by 285 nm is the least affected. Although there are some intensity changes, all characteristic peaks such as N2 line (around 700 nm), zero phono (around 660-680 nm) Stokes (around 680-687 nm) and anti-Stokes phonon side bands (around 708-715 nm) remain.[20-24]

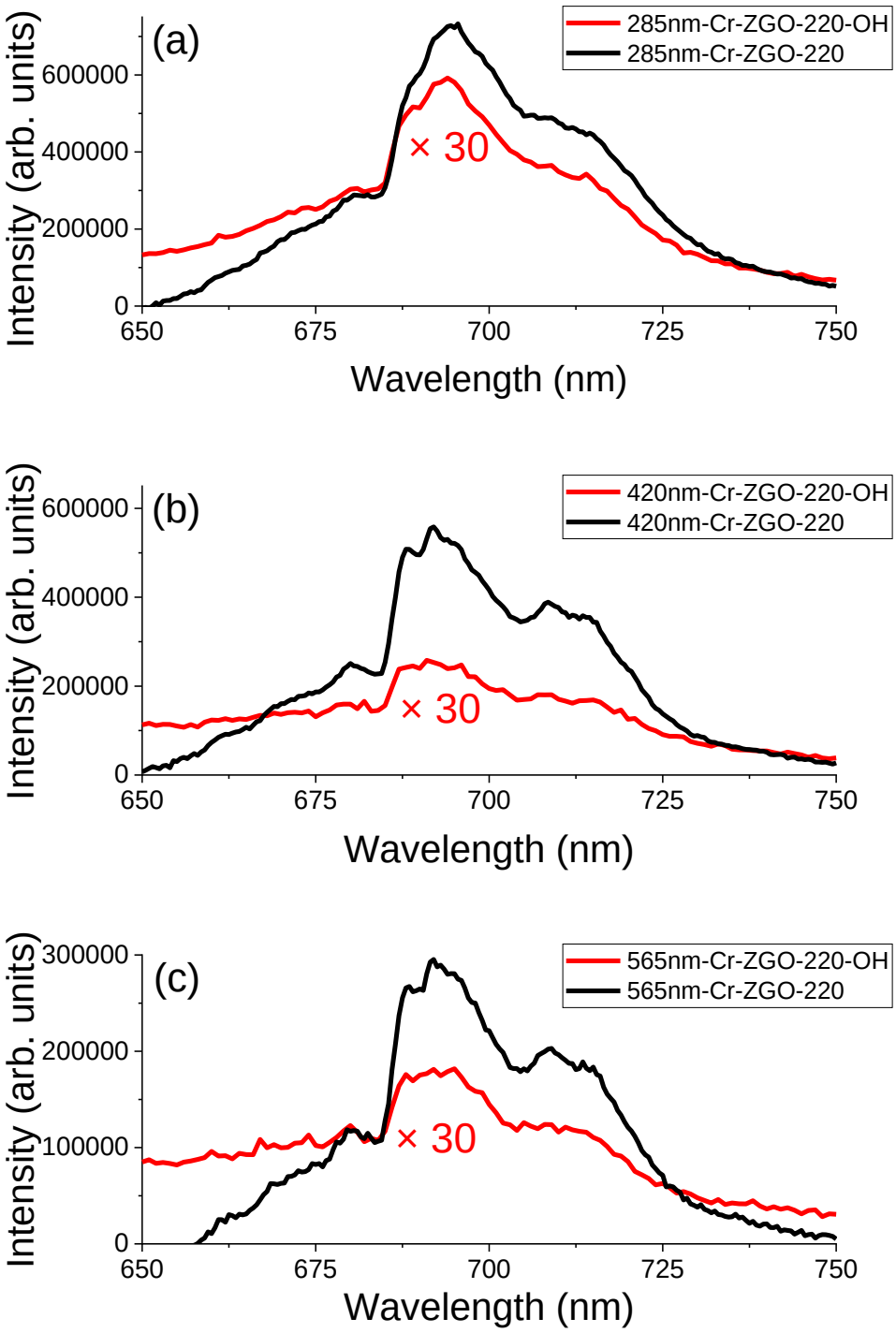

Figure 5- 3. The emission scan for the sample Cr-ZGO-220 before and after hydroxyl functionalization under (a) 285 nm, (b) 420 nm and (c) 565 nm. The intensity after hydroxyl functionalization is multiplied by 30 times.

Figure 5-4 shows the overall intensity of Cr-ZGO-220-OH, Cr-ZGO-170-OH and Cr-ZGO-220-OH. Cr-ZGO-170-OH shows the strongest emission at all three wavelengths, and Cr-ZGO-120-OH has the weakest emission at all three wavelengths. It should be noticed that emissions of Cr-ZGO-220 and Cr-ZGO-220-OH caused by 420 nm and 555 nm are extremely low, which proves hydroxyl functionalization has more effects on emissions caused by 420 nm and 555 nm for these two samples. The overall intensities suggest that the sample with a stronger emission before functionalization will have a stronger emission after functionalization.

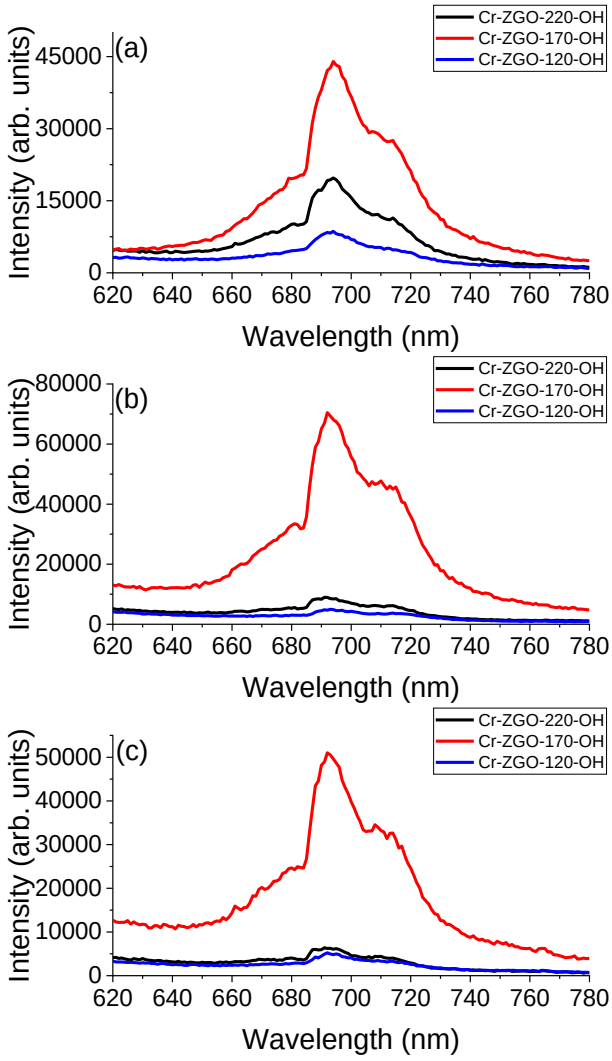

Figure 5- 4. The comparsion of overall intensity of Cr-ZGO-120-OH, Cr-ZGO-170-OH and Cr-ZGO-220-OH caused by (a) 285 nm. (b) 420 nm. (c) 555 nm.

The following discussion mainly focuses on the functionalized Cr-ZGO. We first look at how each sample responds to different excitation wavelengths, shown in Figure 5-5. The excitation wavelengths were selected based on the peak maxima in the excitation scan of each sample. Recalling the results obtained for Cr-ZGO (Chapter 3), the Cr-ZGO-220 sample exhibits the strongest emission at 285 nm excitation, but for the Cr-ZGO-170 and Cr-ZGO-120 samples, the strongest emission occurs when using the 415 nm excitation. According to Figure 5-5 and Figure 3-4 from the temperature chapter, the wavelengths caused the strongest relative intensity and the weakest relative intensity for Cr-ZGO-220-OH and Cr-ZGO-220 are the same. Similarly, the relative intensity order for Cr-ZGO-170-OH and Cr-ZGO-170 are the same. The strongest emission is caused by around 415 nm, and the weakest emission is caused by around 290 nm in both Cr-ZGO-170-OH and Cr-ZGO-170. However, the relative intensity of Cr-ZGO-120-OH is different from Cr-ZGO-120. The emission caused by 415 nm is the strongest in Cr-ZGO-120 samples (Figure 3-4 (a) from temperature chapter) but it is the weakest emission in Cr-ZGO-120-OH samples. There are two possible reasons for this change. First, the hydroxyl functionalization increases the relative intensity of emission at 285 nm excitation. Secondly, the hydroxyl functionalization decreases the relative intensity of emission at 420 nm excitation. However, the temperature chapter points out that the emission caused by around 285 nm excitation is caused by the energy transfer from the host to Cr^{3+} and this process can be bridged by the host defect but hydroxyl functionalization happened on the surface of Cr-ZGO; therefore, hydroxyl functionalization is unlikely to affect the defect of structure so the first reason is the most possible.[19] Therefore, the hydroxyl functionalization decreasing the relative intensity of emission at 420 nm excitation is the reason why the order of the relative intensities in Cr-ZGO-120-OH samples is changed. It has been mentioned the energy transfer process from materials to modifiers. Therefore, this energy transfer process affects spin-allowed $^4A_2 \rightarrow {}^4T_1$ (^4F) transitions (emission caused by around 420 nm) most.[20-22]

However, it should be noticed the emission caused by around 420 nm for Cr-ZGO-170-OH is not affected by the hydroxyl functionalization, and it is still the strongest relative intensity in both Cr-ZGO-170-OH and Cr-ZGO-170. The reason why emission at 420 nm excitation is not affected is possible because Cr-ZGO-170 shows the strongest emission at

around 420 nm and 565 nm (Figure 3-5 (b) and (c) from temperature chapter). In addition, the emission at 290 nm in Cr-ZGO-170-OH (Figure 5-5 (a)) is close to the emission at 553 nm. This suggests that after being affected by hydroxyl functionalization, the emissions of Cr-ZGO-170-OH are still strong enough to overcome the change of relative intensity caused by the hydroxyl functionalization. In terms of Cr-ZGO-220-OH, since the emission caused by around 285 nm is affected least by hydroxyl functionalization, the order of the relative intensities does not change. In a summary, emissions caused by around 565 nm and 420 nm are influenced significantly by OH functionalization, especially 420 nm.

According to the Figure 5-5, Cr-ZGO-120 is the most strongly influenced by OH functionalization. The reason why Cr-ZGO-120 is the most strongly influenced could be firstly due to the relatively low temperature. There are fewer ammonium ions on the surface so the OH group can be functionalized on the surface easily. In other words, Cr-ZGO-120 is functionalized better. Secondly, Cr-ZGO-120 has the weakest overall luminescence; therefore, even minor effects of luminescence can be significant for this sample.

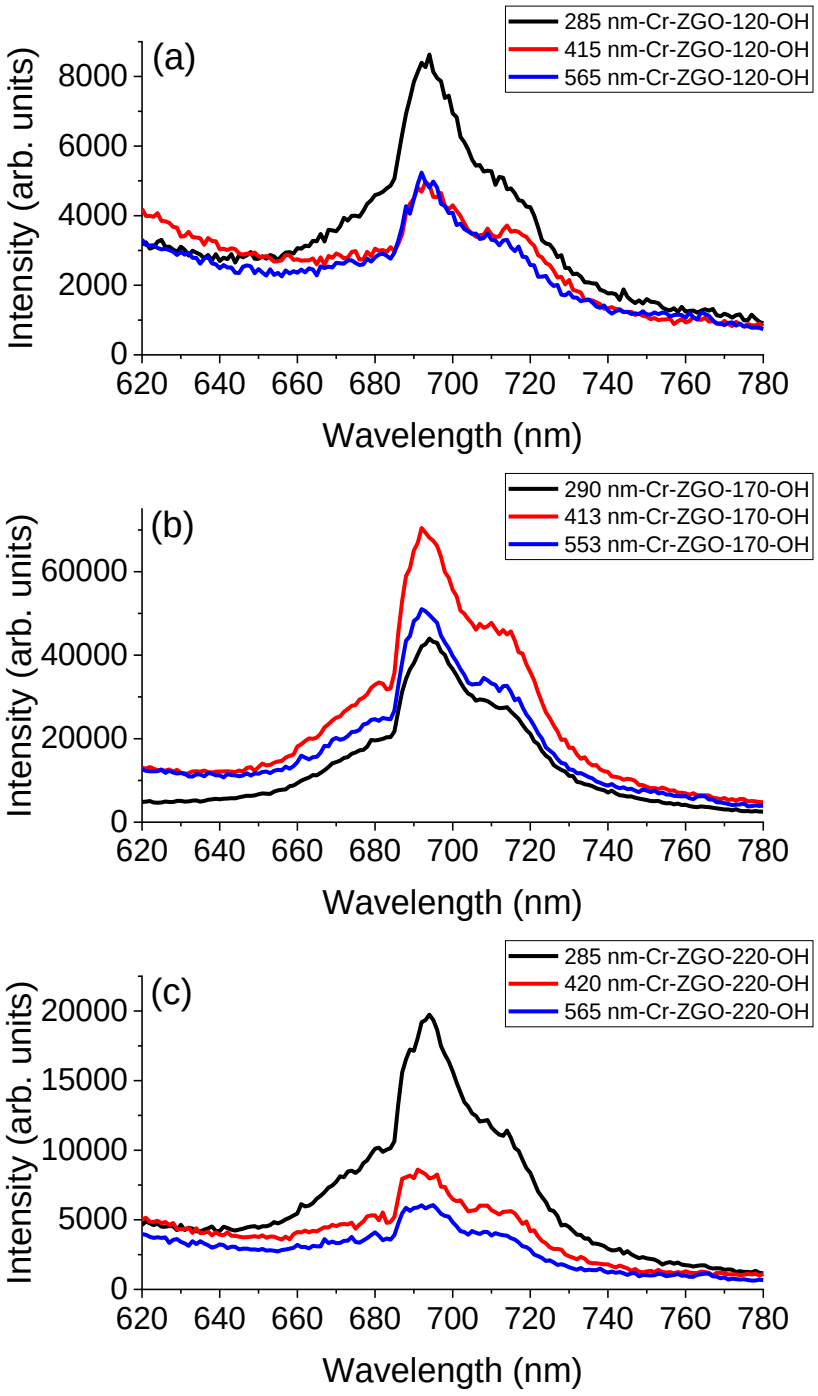

Figure 5- 5. The PL emission spectra of OH-functionalized Cr-ZGO excited at three wavelengths. (a) Cr-ZGO-120-OH, (b) Cr-ZGO-170-OH (c) Cr-ZGO-220-OH.

5.3.2 Hydroxyl Functionalized Cr-ZGO under Different pH Environments

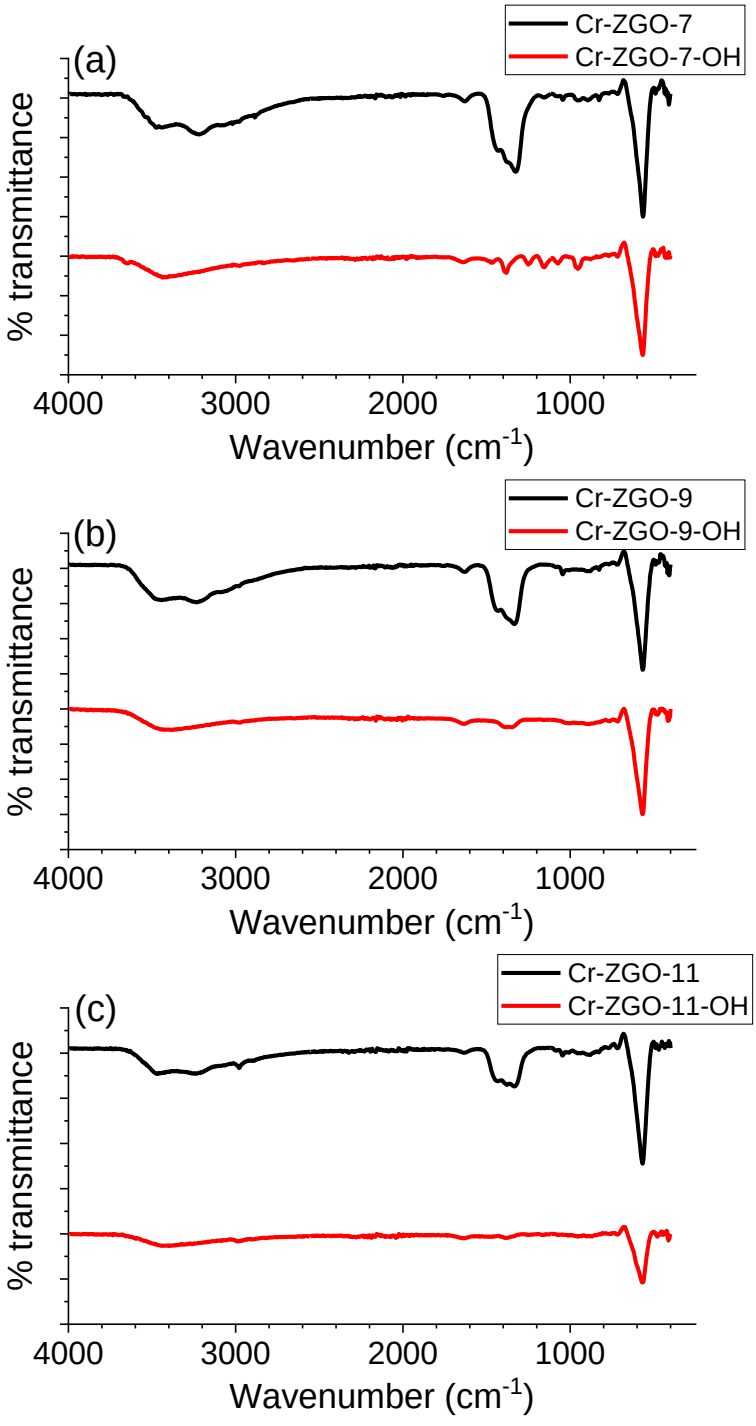

Figure 5- 6. The FTIR spectrum of Cr-ZGO and OH functionalized Cr-ZGO under different pH values. (a) pH =7. (b) pH =9. (c) pH =11

Figure 5-6. shows the FTIR spectrum of Cr-ZGO and OH functionalized Cr-ZGO under different pH values. All the Cr-ZGO before hydroxyl functionalization shows the peaks around 3400 cm^{-1}, 3230 cm^{-1}, 1634 cm^{-1}, 1330 cm^{-1}, 569 cm^{-1} and 419 cm^{-1}, which are all assigned in the previous discussion. pH value change does not affect the ammonium ions are replaced by hydroxyl groups since the peaks around 1330 cm^{-1} and 3230 cm^{-1} show the same change as OH functionalized Cr-ZGO under different temperatures.

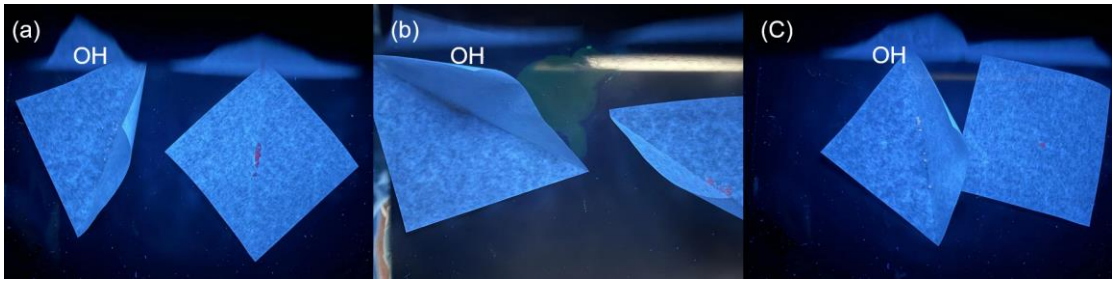

Figure 5- 7. The comparison of Cr-ZGO before and after hydroxyl functionalization under UV-light. The left sample is after hydroxyl functionalization. (a) pH=7 at 365 nm. (b) pH=9 at 365 nm. (c) pH=11 at 365 nm.

The UV light Figure 5-7 shows the Cr-ZGO before and after hydroxyl functionalization. The pH=7 and 11 samples show a more obvious luminescence intensity change under 365 nm. Overall, the hydroxyl functionalization decreases the luminescence intensity, which is the same as the discussion in the hydroxyl functionalization temperature part. Then Figure 5-8 is used to study the details of the emissions after hydroxyl functionalization for samples under different pH environments. Cr-ZGO-7-OH and Cr-ZGO-11-OH show obvious relative intensity changes comparing with Figure 4-5 from pH chapter. Firstly, the strongest relative emission of Cr-ZGO-7-OH is caused by 285 nm, and the weakest relative emission of Cr-ZGO-7-OH is caused by 553 nm; however, Cr-ZGO-7 shows the strongest relative emission is caused around 420 nm, and emission caused around 553 nm is extremely close to emission caused around 420 nm. The weakest relative emission is caused by around 285 nm. Secondly, Cr-ZGO-11 shows the strongest relative emission is caused around 285 nm, and the weakest relative emission is caused by 550 nm. Cr-ZGO-11-OH shows the strongest relative emission is caused by 550 nm and the weakest relative emission caused at 285 nm. pH change has significant effects on the relative intensity change of

luminescence caused by hydroxyl functionalization. As previously discussed, hydroxyl groups would replace the ammonium ions and have effects on emissions caused by around 415 nm and 550 nm. For the Cr-ZGO-7, since the pH is low during the synthesis, due to the low concentration of ammonium ions, hydroxyl groups can replace the ammonium ions easily and cause the quenching of luminescence caused by around 415 nm and 550 nm. However, for the Cr-ZGO-11, because the high concentration of the ammonium ions will protect the surface from the hydroxyl group, hydroxyl groups cannot replace the ammonium ions efficiently and prevent the quenching of luminescence caused by around 415 nm and 550 nm.

To find out which sample has the strongest emission, Figure 5-9 indicates the overall intensity comparison for Cr-ZGO under different pH environments. Cr-ZGO-7-OH shows the strongest overall intensity under all three wavelengths. Cr-ZGO-11-OH shows the weakest intensity under 285 nm and 420 nm, which is the same as Figure 4-6 (a) and (b) from the pH chapter. However, due to the protection of ammonium ions, Cr-ZGO-11-OH intensity under 555 nm becomes the second strongest. In addition, it should be noticed that for the emissions caused by 420 nm and 555 nm for Cr-ZGO-7-OH, there are more minor peaks showing around 700 nm. This is another piece of evidence of energy transfer process from materials to modifiers. These multi-steps of energy transfer cause those minor peaks.

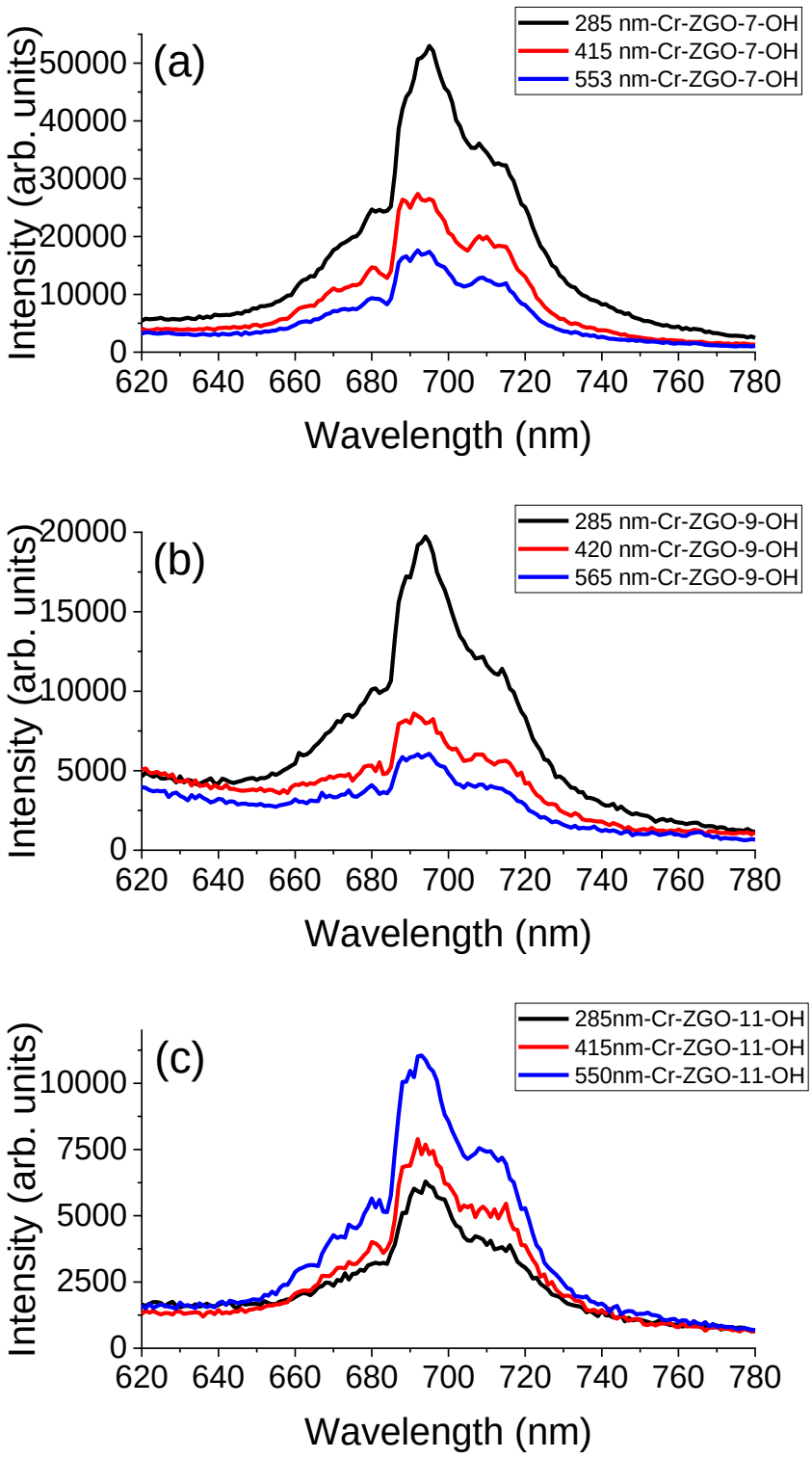

Figure 5- 8. The emission scans under each sample own excitation wavelengths for hydroxyl functionalized Cr-ZGO. (a) Cr-ZGO-7-OH. (b) Cr-ZGO-9-OH. (c) Cr-ZGO-11-OH.

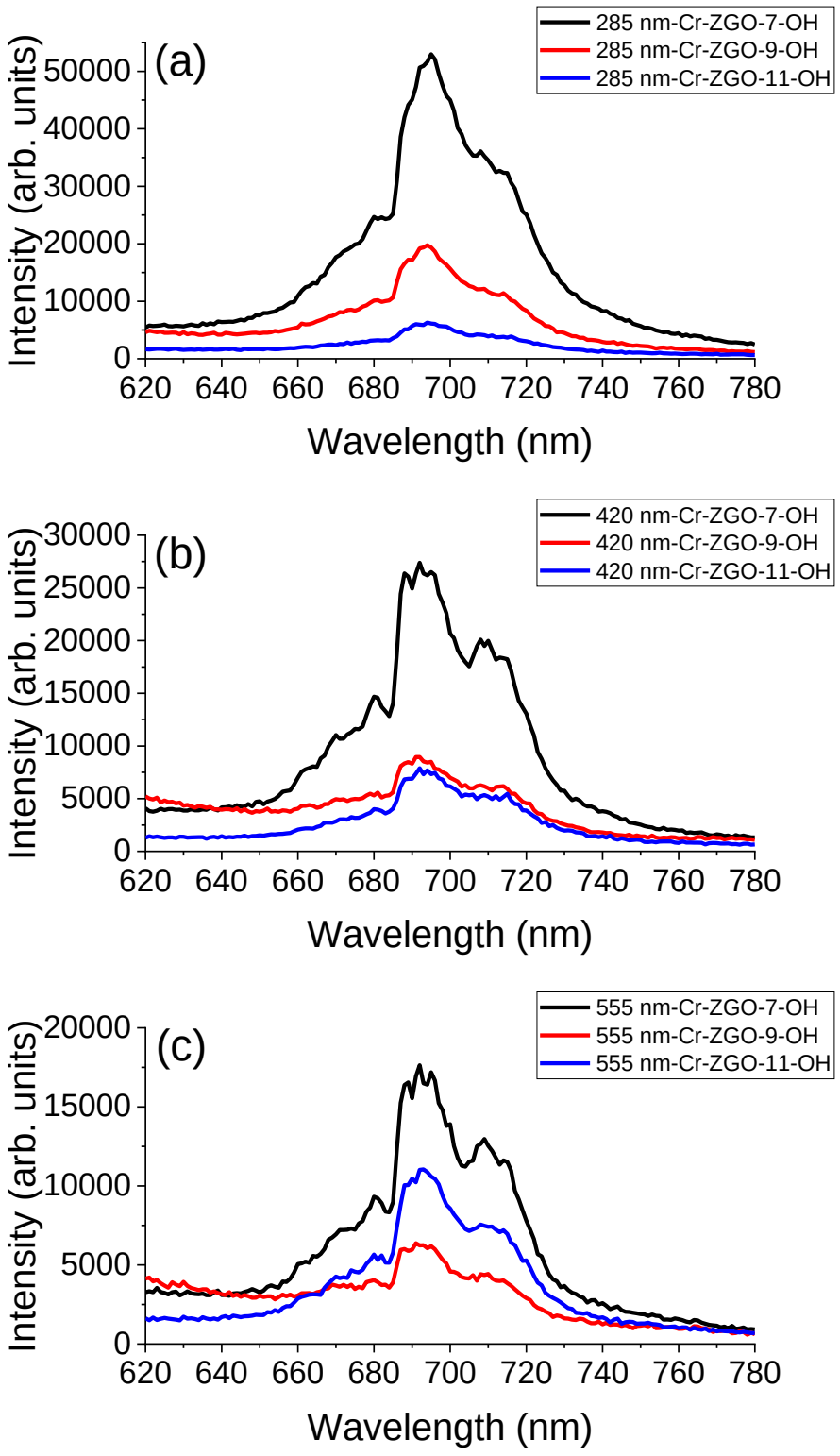

Figure 5- 9. The overall intensity for all three samples under the same wavelengths. (a) 285 nm. (b) 420 nm. (c) 555 nm.

5.3.3 Aminosilanized Cr-ZGO under Different Hydrothermal Temperatures

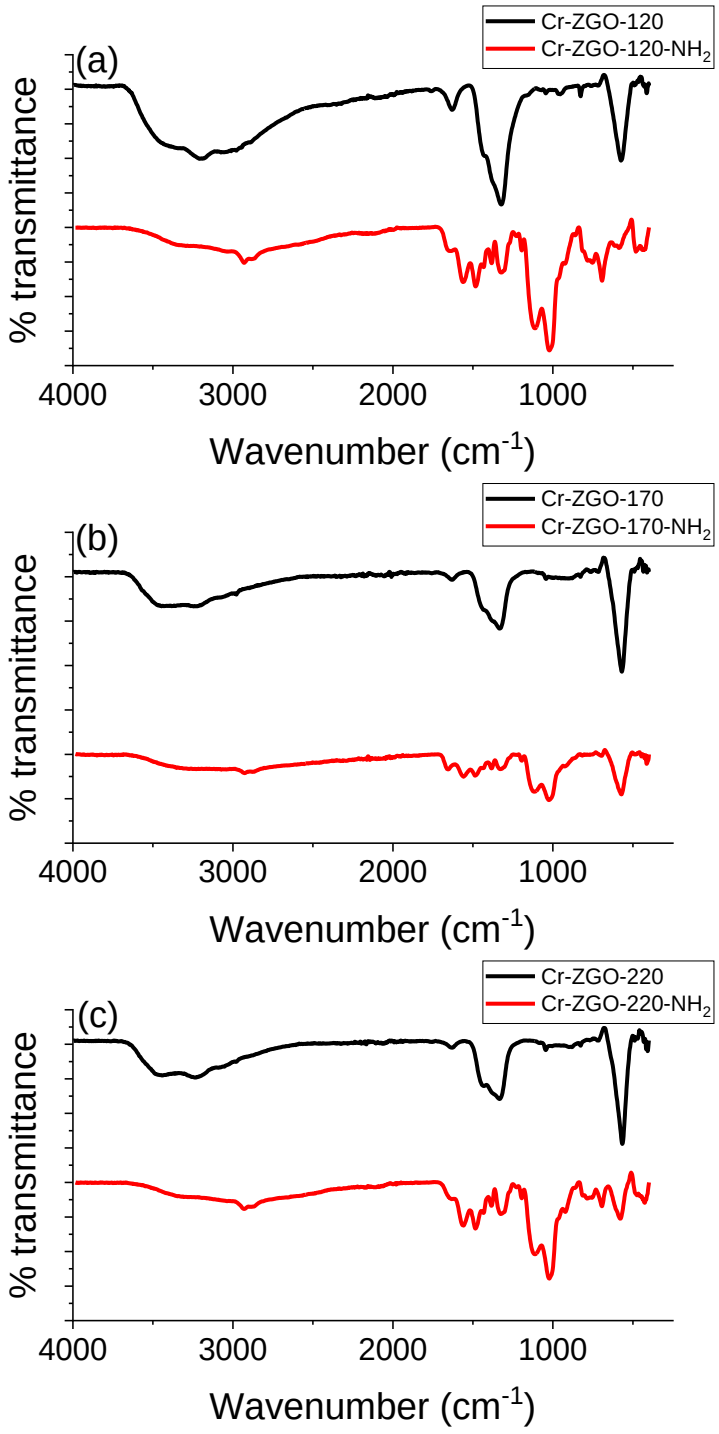

Figure 5- 10. The FTIR spectrum of Cr-ZGO and NH_2 functionalized Cr-ZGO under different pH values. (a) 120 ℃. (b) 170 ℃. (c) 220 ℃.

Figure 5-10 is the FTIR spectrum of Cr-ZGO and aminosilanized Cr-ZGO under different temperatures. The peaks at around 3400 cm^{-1}, 2930 cm^{-1}, 1656 cm^{-1}, 1555 cm^{-1}, 1485 cm^{-1}, 1386 cm^{-1}, 1334 cm^{-1}, 1124 cm^{-1} and 1027 cm^{-1} are obviously changed in all three samples. The broad peak around 3400 cm^{-1} is assigned as O-H stretching. After aminosilanization, the broad huge peak around 3400 cm^{-1} becomes flat. This represents O-H stretching is replaced by N-H stretching at around 3350 cm^{-1}. Peak around 2930 cm^{-1} is caused by C-H stretching. After the aminosilanization, the carbon is from 3-Aminopropyl-triethoxysilane (APTES). Peaks at around 1656 cm^{-1}, 1555 cm^{-1} and 1485 cm^{-1} are due to the N-H bending; peaks around 1386 cm^{-1} and 1334 cm^{-1} are from C-H bending. Peaks around 1124 cm^{-1} and 1027 cm^{-1} are caused by Si-O stretching and C-O-C stretching, respectively. Si-O stretching and C-O-C stretching are from 3-Aminopropyl-triethoxysilane (APTES). The N-H bending peak shape is different after aminosilanization, which means the chemical environment of N-H is changed.[8]

The aminosilanization also significantly decreases the luminescence intensity. To avoid repetition, Figure 5-11 is used as an example. The luminescence shows at least 60 times weaker after aminosilanization for all the samples under different temperatures and pH environments. Figure 5-12 shows the emission after aminosilanization for samples under different temperatures. The emissions of all three samples caused by around 415 nm and 555 nm are lower than the emission caused by around 280 nm. This indicates that aminosilanization effectively affects the emissions caused by 415 nm and 555 nm no matter how strong the emission caused by around 280 nm. In terms of overall intensity, all three samples' emissions caused by 415 nm and 555 nm are around 2000 to 2500 arbitrary unit. The difference is not obvious. However, Cr-ZGO-220-NH_2 shows the strongest intensity for emission caused by around 280 nm among all three samples. This is probably because Cr-ZGO-220 has the strongest overall emission caused by 280 nm (Figure 3-5 (a) from the temperature chapter).

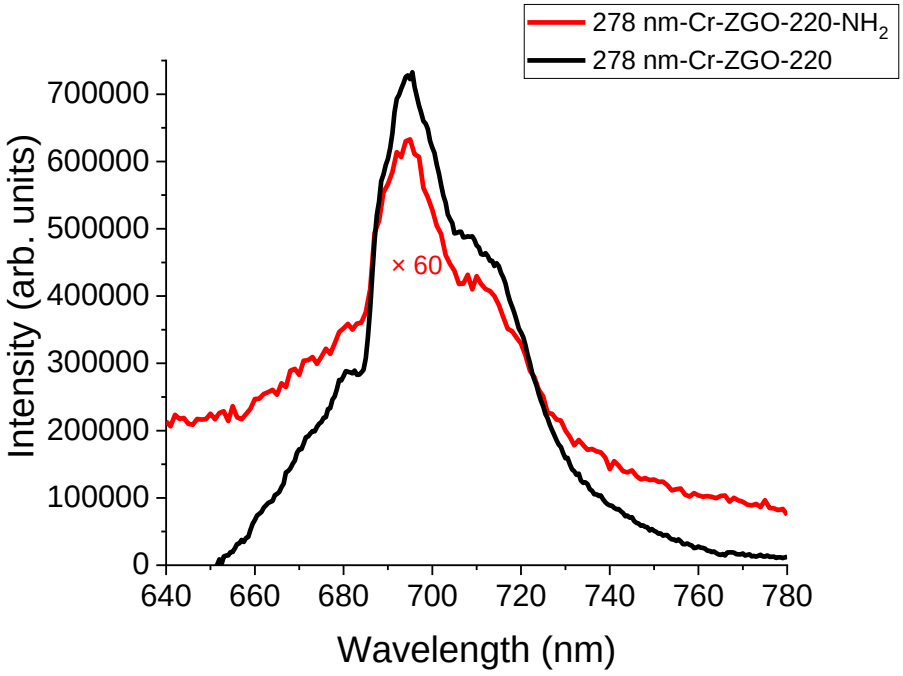

Figure 5- 11. The emission scan for the sample Cr-ZGO-220 before and after aminosilanization under 278 nm. The intensity of Cr-ZGO-220-NH_2 is multiplied by 60.

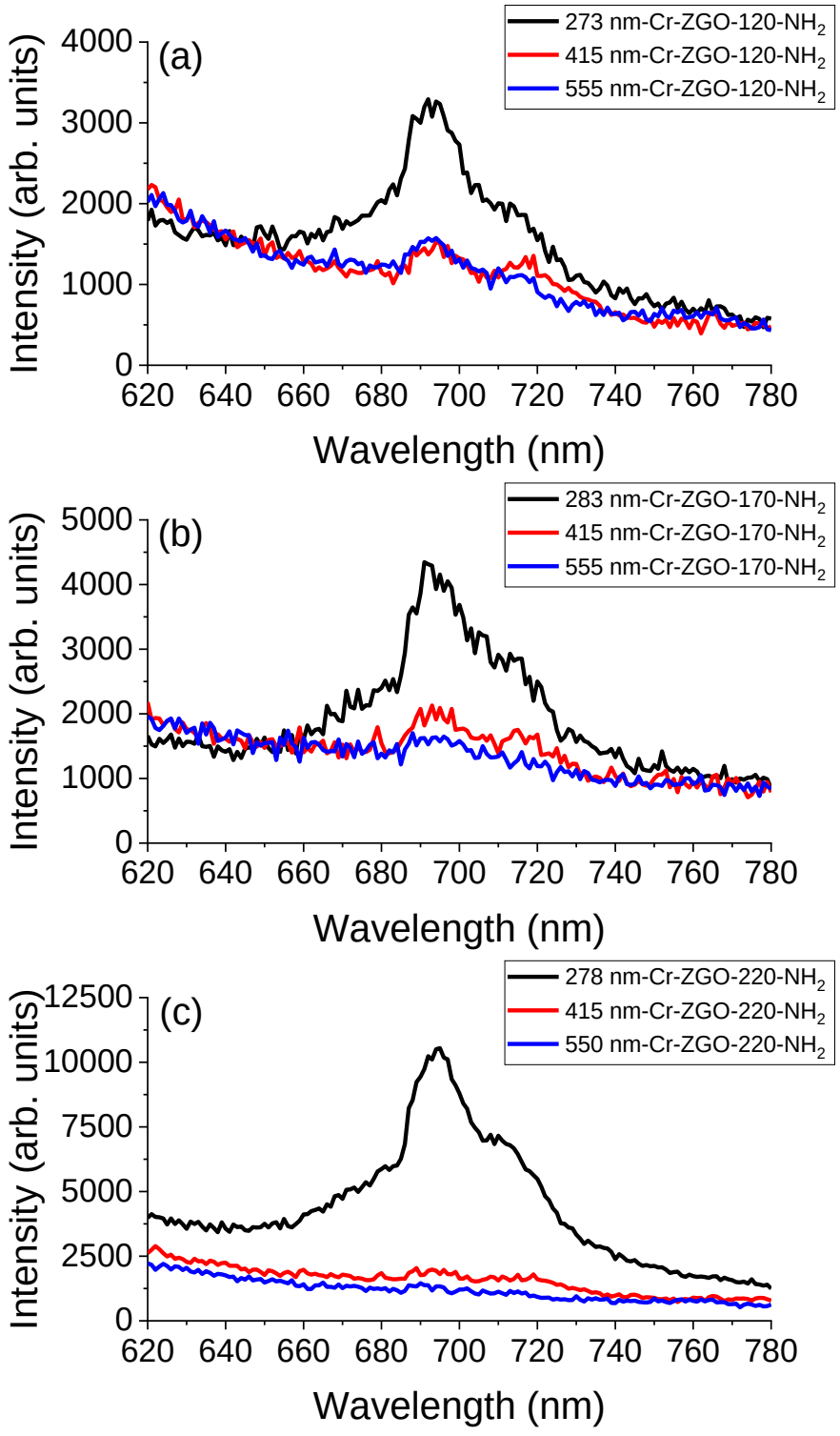

Figure 5- 12. The emission after aminosilanization for samples under different temperature. (a) Cr-ZGO-120-NH_2. (b) Cr-ZGO-170-NH_2. (c) Cr-ZGO-220-NH_2

5.3.4 Aminosilanized Cr-ZGO under Different pH Environments

The IR shows the same change as different temperature samples shown in Figure 5-13. The peaks are changed at around 3400 cm^{-1}, 2930 cm^{-1}, 1656 cm^{-1}, 1555 cm^{-1}, 1485 cm^{-1}, 1386 cm^{-1}, 1334 cm^{-1}, 1124 cm^{-1} 1027 cm^{-1}, 569 cm^{-1} and 419 cm^{-1} after aminosilanization. There is another notable change. The Zn-O vibration around 569 cm^{-1} does not dramatically decrease in Cr-ZGO-7-NH_2 sample; however, that peak decrease significantly in Cr-ZGO-9-NH_2 and Cr-ZGO-11-NH_2 samples. This is possibly because Cr-ZGO-7 sample has relatively more oxygen vacancies around Zn; therefore, the amino group may be trapped by Zn instead of O around Zn on the surface.

The aminosilanization of samples under different pH values shows the same trend as samples under different temperatures in terms of the effects on emissions caused by around 415 nm and 555 nm (Figure 5-14). First, the emissions of all three samples caused by around 415 nm and 555 nm are lower than the emission caused by around 280 nm. It should be noticed that Cr-ZGO-7-NH_2 has the strongest overall intensity among the three samples. The emissions of Cr-ZGO-7-NH_2 caused by around 415 nm and 555 nm are over 20000 arb. unit but the emissions of Cr-ZGO-9-NH_2 and Cr-ZGO-11-NH_2 caused by around 415 nm and 555 nm are around 2000 and 1000 arb. unit, respectively. This is because Cr-ZGO-7 has the strongest overall emissions caused by 415 nm and 555 nm (Figure 4-6 (b) and (c) from pH chapter). Secondly, the high pH environment will lead to a weak emission caused by around 280 nm, which suggests that high pH may have a better functionalization result. There has been a study pointing out the aminosilan reacts with the original function groups on the surface to form a new bond rather than replacing the original group.[8] Therefore, the high pH environment will lead to a high concentration of hydroxyl group and amino group, which will lead to a better aminosilanization, and this better aminosilanization decreases the overall intensity.

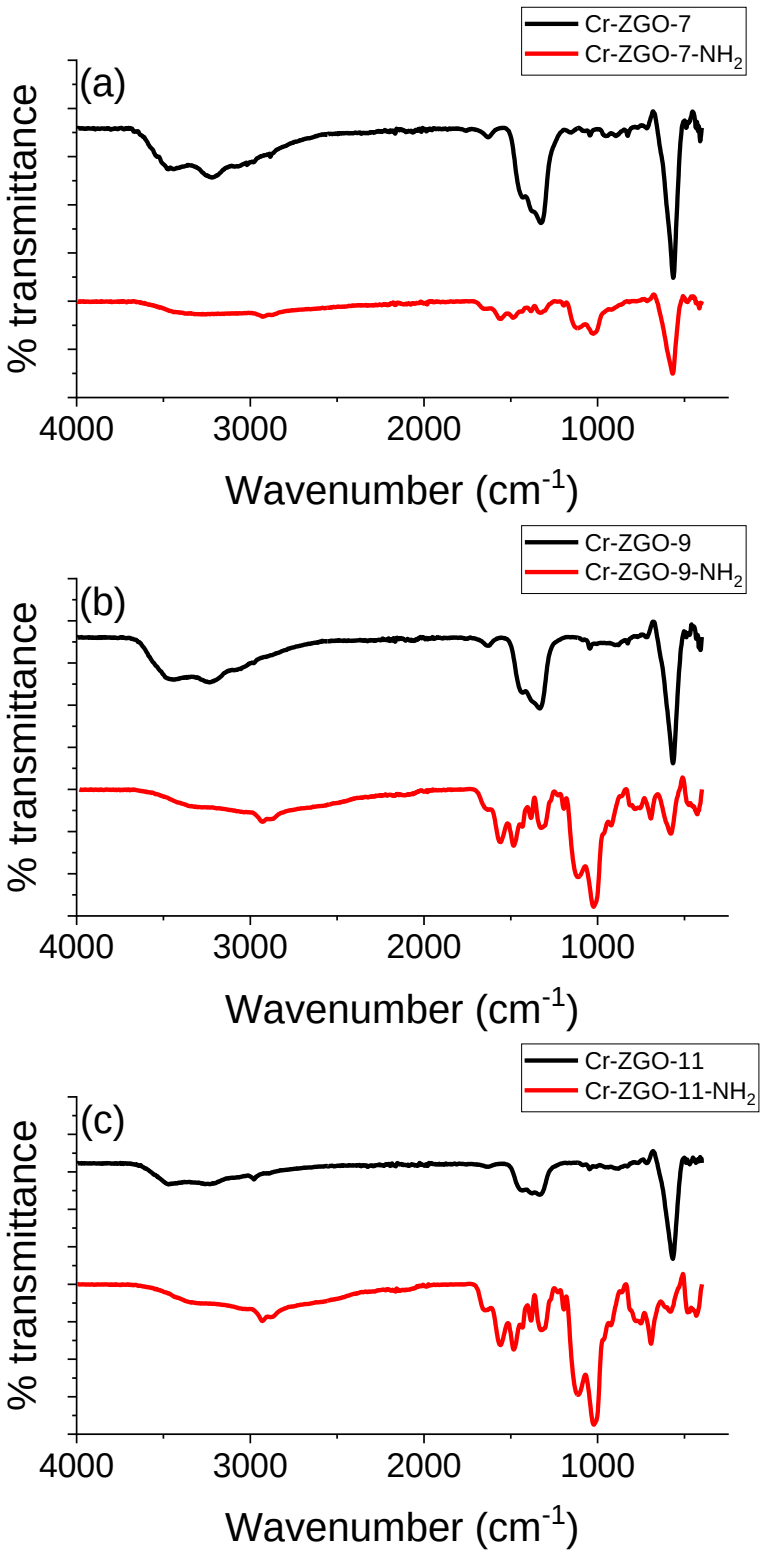

Figure 5- 13. The FTIR spectrum of Cr-ZGO and NH_2 functionalized Cr-ZGO under different pH values. (a) Cr-ZGO-7-NH_2. (b) Cr-ZGO-9-NH_2. (c) Cr-ZGO-11-NH_2.

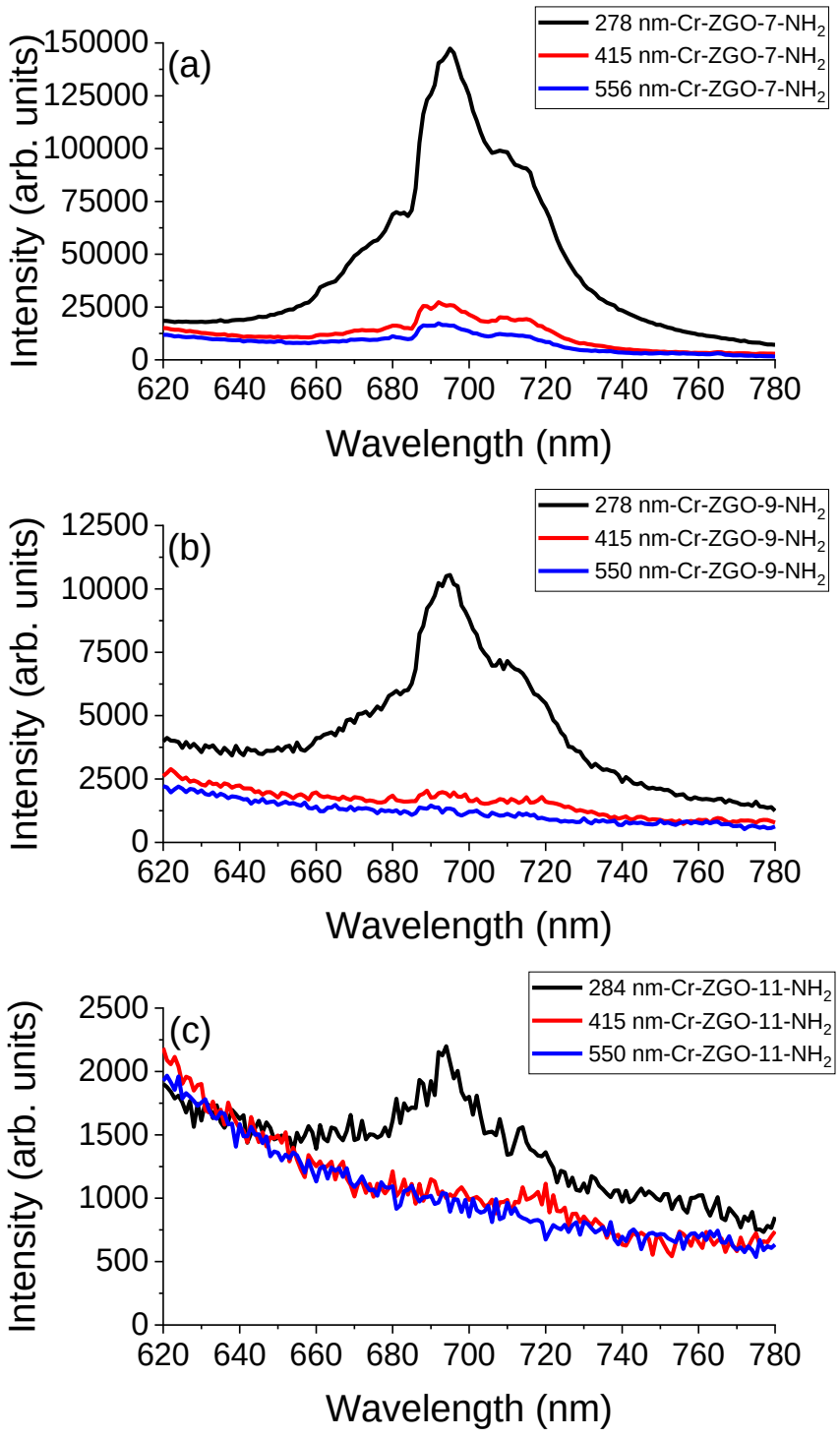

Figure 5- 14. The emission scans under each sample own excitation wavelengths for aminosilanization functionalized Cr-ZGO. (a) Cr-ZGO-7-NH_2. (b) Cr-ZGO-9-NH_2. (c) Cr-ZGO-11-NH_2.

5.4 Conclusion

The Cr-ZGO samples have been successfully functionalized with the hydroxyl group and aminosilan group. The FTIR spectrum suggests there are ammonium ions and nitrate ions before hydroxyl functionalization and aminosilanization. Those ammonium ions and nitrate ions are from ammonium hydroxide and zinc nitrate and gallium nitrate. The process of hydroxyl functionalization will replace the ammonium and nitrate ions while aminosilan will react with the original function groups on the surface to form a new bond rather than replacing the original group. The PL results show that functionalization has a significant effect on the emission caused by around 420 nm and 555 nm for samples under different temperatures and pH environments. This is due to the energy transfer process from materials to modifiers. However, samples under different pH environments are more sensitive to both hydroxyl functionalization and aminosilanization because different pH environments will affect the concertation of ammonium and nitrate ions on the surface and cause further influence on the functionalization. A low pH environment (pH=7) will lead to a stronger overall intensity after functionalization because pH=7 sample has the strongest emission before the functionalization.

5.5 References

[1] Luo, Q., Wang, W., Tan, J., Yuan, Q. *Chin. J. Chem*. **2021**, 39, 1009–1021.

[2] Wang, Y., Li, Z., Lin, Q., Wei, Y., Wang, J., Li, Y., Yang, R., Yuan, Q. *ACS Sens*. **2019**, 4, 2124–2130.

[3] Luitel, HN., Watari, T., Torikai, T., Yada, M., Chand, R., Xu, C-N., Nanoka, K. *Appl. Surf. Sci*. **2010**, 256, 2347–2352.

[4] Liepina, V., Millers, D., Smits, K. *J. Lumin*. **2017**, 185, 151–154.

[5] Sun, M., Li, Z-J., Liu, C-L., Fu, H-X., Shen, J-S., Zhang, H-W. *J. Lumin*. **2014**, 145, 838–842.

[6] Misra, SK., Dybowska, A., Berhanu, D., Luoma, SN., Valsami-Jones, E. *Sci. Total Environ*. **2012**, 438, 225–232.

[7] Carrillo-Carrion, C., Escudero, A., Parak, WJ. *Trends Analyt Chem*. **2016**, 84, 84–96.

[8] Ramírez-García, G., d'Orlyé, F., Gutiérrez-Granados, S., Martínez-Alfaro, M., Mignet, N., Richard, C., Varenne, A. *Colloids Surf. B*. **2015**, 136, 272–281.

[9] Feng, F., Chen, X., Li, G., Liang, S., Hong, Z., Wang, H-F. *ACS Sens*. **2018**, 3, 1846–1854.

[10] Liu, H., Ren, F., Zhang, H., Han, Y., Qin, H., Zeng, J., Wang, Y., Sun, Q., Li, Z., Gao, M. *J Mater Chem B*. **2018**, 6, 1508–1518.

[11] Hu, S., Li, Z., Luo, Q., Ma, Q., Chen, N., Fu, L., Wang, J., Yang, R., Yuan, Q. *Cryst. Growth Des*. **2019**, 19, 2322–2328.

[12] Maldiney, T., Richard, C., Seguin, J., Wattier, N., Bessodes, M., Scherman, D. *ACS Nano*. **2011**, 5, 854–862.

[13] Shi, J., Sun, X., Zhu, J., Li, J., Zhang, H. *Nanoscale*. **2016**, 8, 9798–9804.

[14] Liu, N., Chen, X., Sun, X., Sun, X., Shi, J. *J. Nanobiotechnology.* **2021**, 19, 113–24.

[15] Maldiney, T., Richard, C., Seguin, J., Wattier, N., Bessodes, M., Scherman, D. *ACS Nano*. **2011**, 5, 854–862.

[16] Liu, N., Chen, X., Sun, X., Sun, X., Shi, J. *J. Nanobiotechnology*. **2021**, 19, 113–24.

[17] Sun, M., Li, D., Zhang, W., Chen, Z., Huang, H., Li, W., He, Y., Fu, X. *J. Solid State Chem.* **2012**, 190, 135–142.

[18] Jiang, Y., Li, Y., Richard, C., Scherman, D., Liu, Y. *J Mater Chem B*. **2019**, 7, 3796–3803.

[19] Zhou, Z., Zheng, W., Kong, J., Liu, Y., Huang, P., Zhou, S., Chen, Z., Shi, J., Chen, X. *Nanoscale*. **2017**, 9, 6846–6853.

[20] Mian, F., Bottaro, G., Wang, Z., You, Y-M., Rancan, M., Sham, T-K., Armelao, L. *Appl. Surf. Sci.* **2022**, 577, 151896.

[21] Bessière, A., Jacquart, S., Priolkar, K., Lecointre, A., Viana, B., Gourier, D. *Opt. Express*. **2011**, 19, 10131-10137.

[22] Mikenda, W., Preisinger, A. *J. Lumin*. **1981**, 26, 53–66.

[23] Mikenda, W., Preisinger, A. *J. Lumin.* **1981**, 26, 67–83.

[24] Bessière, A., Sharma, SK., Basavaraju, N., Priolkar, KR., Binet, L., Viana, B., Bos, AJJ., Maldiney, T., Richard, C., Scherman, D., et al. *Chem. Mater.* **2014**, 26, 1365–1373.

Chapter 6

6 Summary and Future Work

6.1 Summary

This thesis studies the relationship among hydrothermal conditions, optical properties and electronic structure for Cr doped $ZnGa_2O_4$ (Cr-ZGO) and the effects of functionalization on optical properties for Cr-ZGO synthesized under different hydrothermal conditions. The X-ray powder diffraction (XRD) and energy dispersive X-ray spectroscopy (EDX) are utilized to analyze the structure of Cr-ZGO crystallinity and elemental speciation and concentration quantification, respectively. The optical properties are studied by photoluminescence spectroscopy. X-ray absorption near-edge structures (XANES) and extended X-ray absorption fine structure (EXAFS) are used to determine the electronic structure of Cr-ZGO synthesized under different hydrothermal conditions. Finally, Fourier-transform infrared spectroscopy (FTIR) confirms the success of functionalization by identifying the target function groups. The results and discussion are presented in the chapter 3, chapter 4 and chapter 5.

In chapter 1, some foundational background information about near infrared-emitting persistent luminescent materials and their applications in the biological field are introduced. Then some basic information about the dopant and host of Cr-ZGO is introduced. Finally, I introduce the mechanism of Cr-ZGO luminescence and the foundation of the synchrotron radiation-based technique.

In chapter 2, all the characterization techniques used in this thesis are introduced. Firstly, I introduce TPS and APS photon sources and beamlines where the data were collected in this thesis. Then a hydrothermal method to synthesize Cr-ZGO is presented. Moreover, I present details of the math and physics principle behind the X-ray absorption spectroscopy. Finally, fundamental and instrument principles of EDX, XRD, PL and FTIR are discussed.

In chapter 3, the study on the influence of synthesis temperature on the structure and luminescence property of Cr-ZGO is presented. Three Cr-ZGO samples were synthesized

at 120℃, 170℃ and 220℃, respectively with a consistent pH environment (pH=9). At high temperatures, the Ga to Zn ratio of Cr-ZGO is closer to the theoretical value of 2 with high degree of crystallinity and a large crystal size. This is due to that the high temperature is conducive to crystal growth. The PL shows sample synthesized at 170 ℃ has the best optical property, and the emission of samples synthesized at 120 ℃ is the weakest. The XANES and EXAFS results show that the sample synthesized at 170 ℃ has the most oxygen vacancies around Zn, which will help increase the intensity of emission. More oxygen vacancies around Zn will capture more charge carriers, which will cause stronger emission. On the other hand, samples synthesized at 120 ℃ with the weakest emission has the most oxygen vacancies around Ga. This shows the evidence that more oxygen vacancies around Ga will decrease the overall PL intensity. This is because oxygen vacancies around Ga will capture the charge carriers strongly.

In chapter 4, I focus on how different pH environments and base addition rates will affect the structure and luminescence property of Cr-ZGO. Three ZGO samples were synthesized under pH=7, pH=9 and pH=11, respectively, and the hydrothermal temperature was set to 220 ℃ in all cases. In addition, three ZGO samples were synthesized under slow, medium and fast base addition rates, respectively, and the hydrothermal temperature was set to 220 ℃ constantly, and pH was adjusted to 9 constantly. It turns out strongly base environments will lead to that the Ga/Zn ratio deviating significantly from the theoretical value of 2 with Zn-deficient. Both fast base addition rate and high pH value will lead to a large crystalline size. This is because of the accumulation of hydroxy complexes precipitates. The PL results show that medium base addition rates and low pH value (pH=7) will improve the emission intensity. The study on XANES and EXAFS of samples synthesized under different pH environments shows a similar conclusion to the conclusion from chapter 3, which is more oxygen vacancies around Zn, will help increase the intensity of emission, and more oxygen vacancies around Ga will decrease the intensity of emission.

In chapter 5, Cr-ZGO under different hydrothermal conditions was functionalized with hydroxyl group and aminosilane group. According to IR, there are ammonium and nitrate ions before the functionalization on the surface. The ammonium and nitrate ions are from Gallium nitrate, zinc nitrate and ammonium hydroxide. The hydroxyl group will replace

the ammonium ions, and aminosilane group will react with groups on the surface. It turns out emissions caused by 415 nm and 555 nm are negatively affected most by functionalization. In terms of different synthesis temperature, samples synthesized at 170℃ and 220℃ shows the strongest emission after hydroxyl functionalization and aminosilanization, respectively because it has the strongest emission caused by around 280 nm, and emissions caused by 415 nm and 555 nm are negatively affected. In terms of different pH environment, the sample synthesized under pH=7 shows the strongest emission after hydroxyl functionalization and aminosilanization because pH=7 sample has the strongest emission before the functionalization.

.

6.2 Future Work

There are still some areas that need further study. First, as discussed in chapter 4, there are some potential reasons why emission from medium base addition rate sample is stronger than emissions from slow and fast base addition rates samples; how the real reason needs further investigation. The XANES and EXAFS analysis for slow and fast base addition rates samples to determine the structure defects will be helpful to find the reason. In addition, this thesis doesn't study the luminescence lifetime. A luminescence decay curve can be used for this study. Cr-ZGO under different hydrothermal conditions can be excited by one of the exciting wavelengths for a certain time. Once the excitation is ceased, we can monitor the luminescence decay to determine the lifetime of each sample. Moreover, the intensity of Cr-ZGO samples after functionalization still needs to be improved. There have been some studies about improving the intensity.[1-3] For example, it has been reported that by using 5-carboxy-tetramethylrhodamine, which is an organic rhodamine dye, dye-sensitized Cr-ZGO can enhance persistent luminescence.[1] This kind of dye can be used to improve the intensity of Cr-ZGO samples after functionalization. Finally, since Cr-ZGO can be used in the biological field, biocompatibility and toxicity need to be concerned. Functionalizing with certain function groups such as α, ω-dicarboxyl-terminated PEG

(MW = 2000) and polyacrylic acid (PAA) can be used to improve in vitro relative cell viabilities.[4]

6.3 References

[1] Li, Z., Zhao, Y., Huang, K., Huang, L., Zhang, Y., Yang, H., Han, G. *Angew. Chem., Int. Ed*. **2021**, 60, 15886–15890.

[2] Chen, G., Damasco, J., Qiu, H., Shao, W., Ohulchanskyy, TY., Valiev, RR., Wu, X., Han, G., Wang, Y., Yang, C., et al. *Nano Lett*. **2015**, 15, 7400.

[3] Wu, X., Zhang, Y., Takle, K., Bilsel, O., Li, Z., Lee, H., Zhang, Z., Li, D., Fan, W., Duan, C., et al. *ACS Nano*, **2016**, 10, 1060.

Curriculum Vitae

Name: Xincheng Li

Post-secondary Education and Degrees:

The University of Western Ontario
September 2016 – April 2020
Bachelor of Science, *Spec. Chemistry*

The University of Western Ontario
September 2020 – now
Master of Science, *Chemistry*

Related Work Experience

Teaching Assistant
The University of Western Ontario
2020-2022

SKILLS & ATTRIBUTES

Superb technical and computer skills

- Proficient in Microsoft Office Suite, ChemDraw, Athena, and Origin
- Familiarity with computer programming and administrating Windows and MacOS operating systems

Relevant Skills Lab instrument operation Skills

Perform Advanced Operation: GC, HPLC, IC, Uv-Vis, MS, IR, PL, NMR Spectrum